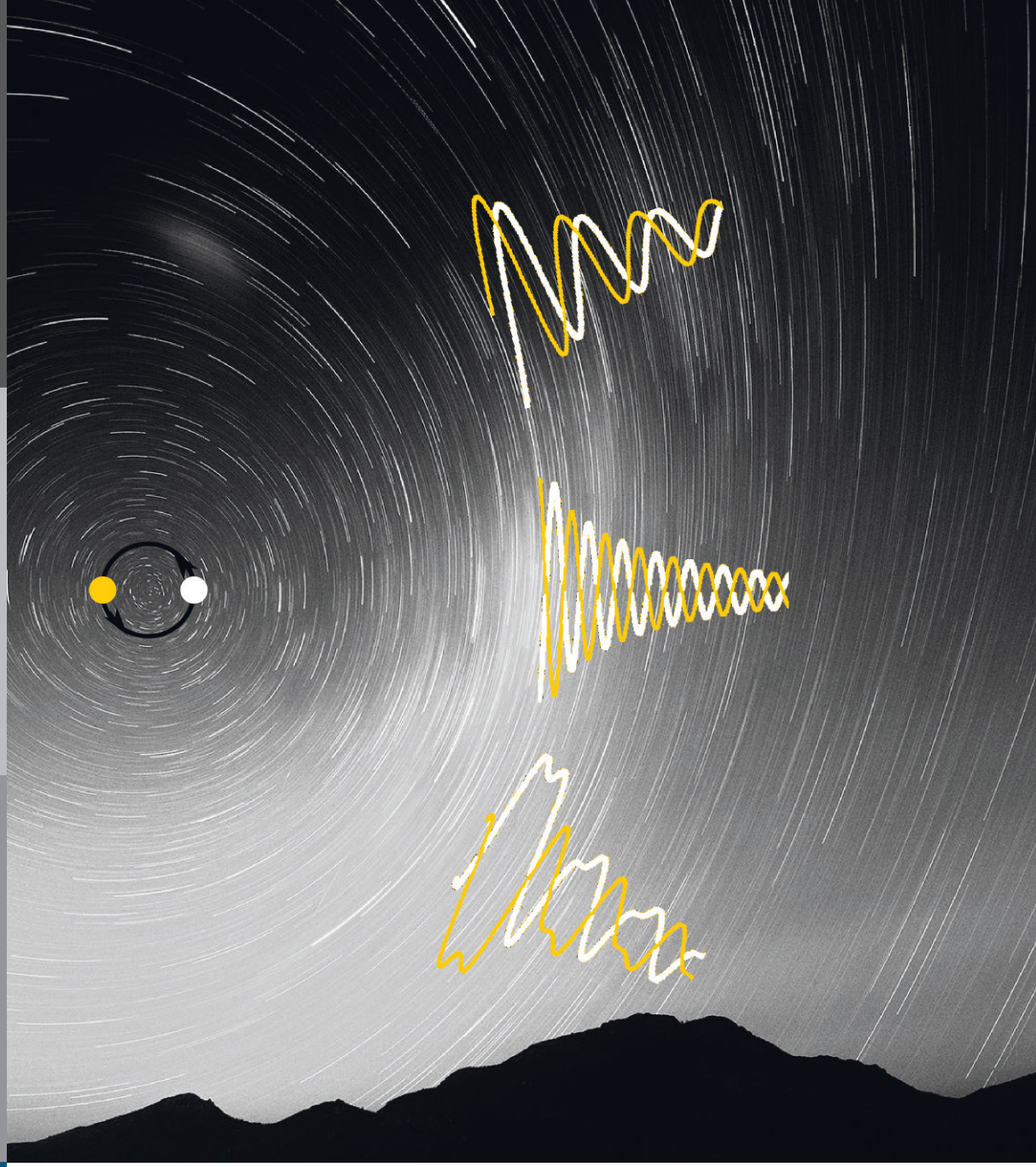

Numerical simulation of gas-induced orbital decay of binary systems in young clusters

Christina Korntreff

JÜLICH
FORSCHUNGSZENTRUM

Member of the Helmholtz Association

Schriften des Forschungszentrums Jülich

IAS Series Volume 25

Forschungszentrum Jülich GmbH
Institute for Advanced Simulation (IAS)
Jülich Supercomputing Centre (JSC)

Numerical simulation of gas-induced orbital decay of binary systems in young clusters

Christina Korntreff

Schriften des Forschungszentrums Jülich

IAS Series Volume 25

ISSN 1868-8489 ISBN 978-3-89336-979-9

Bibliographic information published by the Deutsche Nationalbibliothek.
The Deutsche Nationalbibliothek lists this publication in the Deutsche
Nationalbibliografie; detailed bibliographic data are available in the
Internet at http://dnb.d-nb.de.

Publisher and Distributor:	Forschungszentrum Jülich GmbH Zentralbibliothek 52425 Jülich Phone +49 (0) 24 61 61-53 68 · Fax +49 (0) 24 61 61-61 03 e-mail: zb-publikation@fz-juelich.de Internet: http://www.fz-juelich.de/zb
Cover Design:	Jülich Supercomputing Centre, Forschungszentrum Jülich GmbH
Cover Picture:	© markus weber photography
Printer:	Grafische Medien, Forschungszentrum Jülich GmbH
Copyright:	Forschungszentrum Jülich 2014

Schriften des Forschungszentrums Jülich
IAS Series Volume 25

D 38 (Diss., Köln, Univ., 2014)

ISSN 1868-8489
ISBN 978-3-89336-979-9

Persistent Identifier: urn:nbn:de:0001-2014072202
Resolving URL: http://www.persistent-identifier.de/?link=610

Zusammenfassung

Die meisten Sterne entstehen als Doppel- oder Mehrfachsternsysteme in Sternhaufen von hunderten bis zu hunderttausenden von Sternen. Diese jungen Sternhaufen sind immer noch in das Gas der Molekülwolke eingebettet, aus der sie entstanden sind und aus der auch weiterhin Sterne entstehen können. Das Gas bleibt ungefähr 1-2 Myr im Sternhaufen, bevor es durch den Strahlungsdruck der Sterne und andere Prozesse den Sternhaufen verlässt. Es stellt sich die Frage, ob sich die Eigenschaften und der relative Anteil an Doppelsternen in dieser Gas-Phase ändert.

Die Wechselwirkung zwischen den Sternen in einem Sternhaufen zerstört Doppelsterne mit langen Perioden (>10^5 Tage). Neben der Wechselwirkung zwischen einem Doppelstern und anderen Sternen ergeben sich auch Wechselwirkungen mit dem Gas in welches er eingebettet ist. Der Doppelstern erzeugt eine spiralförmige akustische Dichtewelle in dem umliegenden Gas, die sich vom Doppelstern weg ausbreitet. Dies führt zu einem Drehimpulstransport vom Doppelstern zum Gas aus dem eine Verringerung des Doppelsternorbits resultiert, welche in der vorgelegten Dissertation untersucht wird.

Stahler (2010) entwickelte eine analytische Näherung zur gasinduzierten Orbitverringerung von Doppelsternsystemen, welche hier auf eine Doppelsternpopulation angewandt wurde. Als Resultat zeigt sich, dass die gasinduzierte Orbitverringerung die Periodenverteilung nur für kurze Perioden (<10^5 Tage) signifikant ändert. Vergleicht man die resultierende Periodenverteilung mit Beobachtungen ergibt sich nur für Sterne mit $\approx$ 1 $M_\odot$ eine gut Übereinstimmung. Für diesen ersten Ansatz wurden einige Vereinfachungen angenommen. So wurde in der analytische Näherung die Entstehung der Dichtewellen nur indirekt berechnet und der Orbit eines Doppelsternsystems als zirkular angenommen. Beobachtungen hingegen zeigen, dass die meisten Doppelsterne einen exzentrischen Orbit mit $e > 0.2$ haben. Um auch exzentrische Doppelsternorbits zu untersuchen, wurde eine 3D hydrodynamische Simulation entwickelt. Diese berechnet die gravitative Wechselwirkung zwischen einem Doppelstern und dem Gas, die entstehende Dichtewelle und die resultierende Orbitverringerung. Es wurde eine Parameterstudie durchgeführt, die ein breites Spektrum an Gas- und Doppelsterneigenschaften abdeckt.

Der Vergleich der Ergebnisse aus der Simulation mit den Ergebnissen der analytische Näherung sind ähnlich für die Abhängigkeiten der Orbitverringerung von der Gasdichte, der Zeit, die der Doppelstern eingebettet ist und dem Massenverhältnis des Doppelsterns. Im Gegensatz dazu unterscheiden sich die Abhängigkeiten stark für Parameter, die mit der Generierung der Dichtewelle

im Gas zusammenhängen. Bei der Simulation von Doppelsterne mit exzentrischen Orbits erfahren diese eine viel schnellere Orbitverringerung als ihre zirkularen Gegenstücke. Schlussendlich wurden die numerischen Ergebnisse in einer Fitformel zusammengefasst, die es erlaubt, die Auswirkungen der gasinduzierten Orbitverringerung in einer Doppelsternpopulation kompakt darzustellen.

In der analytischen Näherung verschmelzen Doppelsterne mit kurze Perioden ($<10^5$ Tage) umso schneller je schwerer der Doppelstern ist. Doch gerade für massive Doppelsterne werden viele Doppelsterne mit kurze Perioden beobachtet. Die Simulation zeigt hier eine bessere Massenabhängigkeit, aber auch die durch die Fitformel berechnete Periodenverteilung kann die beobachteten Periodenverteilungen nicht reproduzieren. Dabei ist zu berücksichtigen, dass für diesen Vergleich nur ein Sternhaufentyp betrachtet wurde und zur Reproduktion aber alle möglichen Sternhaufentypen berücksichtigt werden müssten. Da die Entstehung und Entwicklung eines Sternhaufens noch immer Bestand aktueller Forschung ist, können Fortschritte auf diesem Gebiet zu einer umfassenderen Darstellung der Doppelsternpopulation beitragen. Mit diesem Wissen kann die hier entwickelte Methode genutzt werden, um die gasinduzierte Orbitverringerung einer gesamten Doppelsternpopulation zu berechnen.

Abstract

A large fraction of stars ($\approx 50\%$ of the field population) are not single but part of a binary or multiple system. These binary systems form from the gas and dust in molecular clouds largely building clusters that are initially still embedded in the star-forming gas. Here the question arises whether the properties and frequency of binaries change during this gas-embedded phase.

It is known that the gravitational interactions between stars in a cluster environment can destroy long-period binaries ($> 10^5$ days). However, not only can the interaction between the stars themselves change the binary properties but also those between binary systems and the surrounding gas. There, the binary potential torques the nearby gas, producing an outgoing acoustic wave. This wave transports angular momentum from the binary to the gas, resulting in a decay of the binary orbit. This effect is the central focus of the thesis presented here.

First, an analytic approximation for the gas-induces orbital decay by Stahler (2010) was applied to a binary population and the results compared to observations. It was found that the process of orbital decay significantly changes the properties of short period binaries ($< 10^5$ days). The resulting period distribution resembles the one observed for solar-mass stars, but fails to do so for other mass ranges.

The analytic approximation treats only the effect on binary systems with circular orbits and the wave generation is not calculated explicitly. Since, most binary systems have eccentric orbits, a 3D hydrodynamic simulation was developed to avoid these restrictions. It calculates the gravitational binary - gas interaction, the wave generation, and the resulting orbital decay. An extensive parameter study was performed to investigate the dependency of the orbital decay on the binary and gas properties. It was found that the gas density, embedded time span and mass-ratio show a similar scaling as predicted by the analytic approximation. By contrast, all binary and gas properties which influence the wave generation show different dependencies. In particular, it is shown that eccentric orbits lead to a faster orbital decay than their circular counterparts. Eventually, all these effects were combined in a fit formula.

Applying this fit-formula to a binary population, the resulting period distribution shows a better matching mass dependency, but still does not resemble the observed period distributions. The cluster model chosen here is only one example and it is still unknown which cluster types contribute to the field population. Furthermore, future observations of young binary systems and their environment could restrict the parameter space presented here. Having detailed knowledge of the binary's environment, the method developed in this thesis can be used to deduce what impact the gas-induced orbital decay has on a binary population.

Contents

1 Introduction

As observational methods improve, many stars, which were once thought to be single, like Θ^1 Orionis C, are discovered to be in reality binaries (Weigelt et al., 1999) or even triple (Lehmann et al., 2010) systems. Today, various observational methods are used to study binary systems (Sec. 1.1). Not only do the different methods yield different binary properties, but each of these observational techniques is also associated with a different period range for which it can actually be used to detect binaries. Therefore, the comparison of results using different observational methods is error-prone.

The biggest observed sample so far is the field binary population (Sec. 1.2), which represents all stars of the Milky Way which are close enough to Earth so that binaries can be resolved within the limits of the various techniques. As such the field population consists of stars of very different ages up to several billion years (Gyr). In the field, the binary fraction rises with the primary mass m_1 of the binary system, from 20% for brown dwarfs ($m_1 \leq 0.1$ $M_\odot$, Duchêne & Kraus, 2013) to $\geq 80\%$ for O-stars ($m_1 \geq 16$ $M_\odot$, Sana et al., 2012). The period distribution of the field binary population seems also to correlate with the primary mass. For primary masses up to 1.5 $M_\odot$, the period distribution is observed to be log-normal (Duquennoy & Mayor, 1991; Fischer & Marcy, 1992), with different maxima and widths for different mass ranges. However, the observations of binary systems with primaries $1.5\ M_\odot < m_1 < 5\ M_\odot$ and $m_1 \geq 16\ M_\odot$ show in contrast to the log-normal distribution an overabundance of short period binary systems (Carquillat & Prieur, 2007; Sana et al., 2012). Thus, it seems questionable to generalise the log-normal period distribution for these primary masses. The question arises whether these binary properties are already fixed at birth or altered as the cluster develops.

To answer this question one would ideally compare the properties of the star formation outcome to those of the older field binaries. Initially most stars reside in clusters (Lada & Lada, 2003) and only become part of the field population after these clusters dissolve (Goodwin, 2010). Although nowadays, observations at infrared wavelength allow to observe stars at an early stage, their formation process as such is not directly visible. The reason is that the forming stars are deeply embedded in gas (Leisawitz et al., 1989) and the early development is rapid, resulting in only a few stars being observable at the different early stages. Several theoretical concepts for the formation of stars, binaries, and cluster exist (see Sec. 1.3). Nevertheless, the initial conditions of a cluster and its primordial binary properties cannot be derived from these theoretical concepts,

since neither observational nor theoretical initial conditions are well determined.

As a substitute for an initial binary population, young sparse cluster populations are used. Such young clusters have the advantage of all stars being more or less of the same age and therefore being representative for a certain step in the development of the binary population (Sec. 1.4). In such clusters a log-uniform binary period distribution is found (Kouwenhoven et al., 2007; Connelley et al., 2008a,b), which differs from the observations in the field. This leads to the conclusion that some processes must alter the binary properties with age. Various processes have been considered so far as possible culprits for the temporal change of the binary properties (Sec. 1.5).

In the following, the above described current understanding of the first few million years (Myr) of binary evolution in the context of their environment is detailed and the structure of this thesis (see Sec. 1.6) is outlined.

1.1 Binary detection methods

Before looking at observational methods for the detection of binary system, the properties of a binary system are summarised. Theoretically, a binary system is defined by its orbital parameters and the resulting internal energy of two stars. Binary systems consist of two stars which are gravitationally bound and as a result orbit around each other. This means, that their internal/binding energy is negative:

$$E_{\rm int} = \frac{1}{2}\left(m_1\mathbf{v}_1^2 + m_2\mathbf{v}_2^2\right) - \frac{Gm_1m_2}{|\mathbf{r}_{12}|} < 0, \tag{1.1}$$

where m_1, m_2 and $\mathbf{v}_1, \mathbf{v}_2$ are the masses and velocities of the two stars, $\mathbf{r}_{12} = \mathbf{r}_2 - \mathbf{r}_1$ their separation vector, and G is the gravitational constant. The orbits of the two stars follow Kepler ellipses with the eccentricity

$$e = \sqrt{1 - \left(\frac{|\mathbf{r}_{12} \times \mathbf{v}_{12}|^2}{G \cdot M_{sys} \cdot a}\right)} < 1, \tag{1.2}$$

where $\mathbf{v}_{12} = \mathbf{v}_2 - \mathbf{v}_1$ is their relative velocity vector, $\mathbf{r}_{12} \times \mathbf{v}_{12} =: \mathbf{h}$ is the specific angular momentum and $M_{sys} = m_1 + m_2$ the system mass. The semi-major axis of the orbit is given by

$$a = \left(\frac{2}{|\mathbf{r}_{12}|} - \frac{|\mathbf{v}_{12}|^2}{G \cdot M_{sys}}\right)^{-1}. \tag{1.3}$$

Often not the semi-major axis, but the period T of the binary orbit is observed. If the binary systems mass is given, the period can be calculated from the semi-major axis using Kepler's third law

$$T^2 = \frac{4 \cdot \pi^2}{G \cdot M_{sys}} a^3 \tag{1.4}$$

From this follows, that for a given system mass the period and semi-major axis is often used interchangeably. Using the semi-major axis and eccentricity, the specific angular momentum h and the specific orbital energy k can be calculated as

$$h = \sqrt{a \cdot G \cdot M_{sys} |1 - e^2|}, \tag{1.5}$$

$$k = \frac{G \cdot M_{sys}}{2a}. \tag{1.6}$$

After a transformation into the coordinate system of one star, with $r = |\mathbf{r}_{12}|$ and ϕ being polar coordinates, the distance between the two stars is given by

$$r = \frac{a|1 - e^2|}{1 + e\cos\phi}. \tag{1.7}$$

This leads to the periastron r_p and apastron distance r_a (minimum/maximum separation between the two stars) and their corresponding velocities v_p and v_a

$$\text{periastron:} \qquad r_p = a(1-e), \qquad v_p = \sqrt{\frac{G \cdot M_{sys}}{a \cdot |1 - e^2|}}, \tag{1.8}$$

$$\text{apastron:} \qquad r_a = a(1+e), \qquad v_a = \sqrt{\frac{G \cdot M_{sys} \cdot |1 - e^2|}{a}}. \tag{1.9}$$

Thus, the four parameters that characterise a binary system are the masses of its components m_1 and m_2, the semi-major axis, a, and the eccentricity, e, of the orbit. The stellar masses of the binary system define a mass-ratio $q = m_2/m_1 \leq 1$, with m_1 being the primary (more massive) and m_2 the secondary (less massive) star.

Observations often do not reveal all of these binary parameters simultaneously. In this case different observational methods are necessary to determine all parameters. Additionally, these methods also differ in the semi-major axis and therefore period ranges which can be observed.

First, if the angular separation between the two stars is on the one hand large enough to permit them to be observed as a double star in a telescope but on the other hand small relative to the average separation of stars in the neighbourhood, the system is called **visual binary**. As a result, the maximum period which can be detected visually depends on the stellar density in which the binary system is embedded, including possible foreground and background stars. Without velocity measurements, these are only candidates for binary systems since chance alignment is possible. This classification strongly depends on the resolution of the telescope, on the distance of the binary, the separation of the two stars, and their relative brightness. As a result, Jorissen & Frankowski (2008) estimated the minimum observable period of visual binaries to be one year (see first row of Tab. 1.1). This minimum period decreases with the development of new high resolution telescopes. A famous example for the discovery of binary systems in objects which

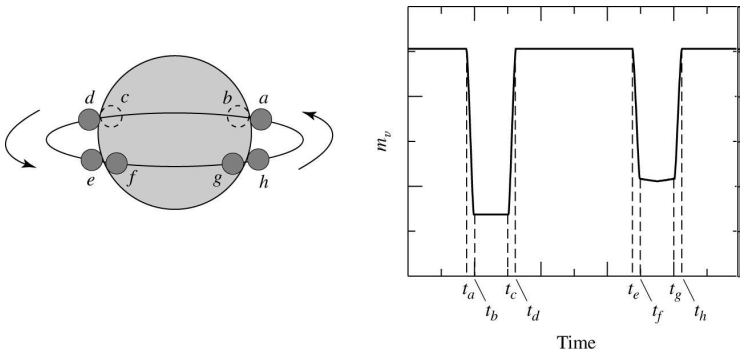

Figure 1.1: Light curve of an eclipsing binary with inclination of 90°. The times indicated on the light curve correspond to the positions of the smaller star relative to its larger companion. In this example the smaller star is hotter than the larger one (Taken from Carroll & Ostlie (2006)).

were thought to be a single star is Θ^1 Orionis C. In 1999, Weigelt et al. discovered Θ^1 Orionis C to be a binary system. By combining different observational methods, in 2010 evidence has been found that Θ^1 Orionis C might be a triple system (Lehmann et al., 2010),

Indirect evidence for binaries is obtained by spectroscopy. As two stars orbit around the common centre of mass, the Doppler effect leads to a variation of the colour of their emitted light. If the plane of the orbit is not perpendicular to the line of sight, of the observer and the observed radial velocity of the system will vary periodically. Such binaries are called **spectroscopic binaries**. They have usually a much smaller separation than visual binaries at the same distance to the sun. Due to the necessary geometry, the inclination cannot be determined with this method (see column 3 in Tab. 1.1).

Binary systems with an orbit oriented approximately along the line of sight of the observer, can also be detected from variations in the luminosity of their light curve during mutual eclipses of their components (see Fig. 1.1). These periodic variations happen, when one star passes in front of the other and the light coming from the rear star is obstructed from view for the observer. This detection method for **eclipsing binary** systems provides the inclination, semi-major axis, and mass of the systems depending on the radius of the eclipsed star (see Tab. 1.1 column 5). For systems with periods greater than one day, it might be possible to observe them also spectroscopically and combine both methods to derive also the absolute masses and semi-major axis independent of other parameters. The observational method for eclipsing binaries is not applicable if the brightness of one member of the binary is significantly brighter than the other, since in this case it might not be possible to observe the fainter member directly. This limits the observations to nearly equal binary components, because the mass is related to the luminosity. For young binary systems this method can be used seldom, since at this stage the luminosity of the stars is highly variable.

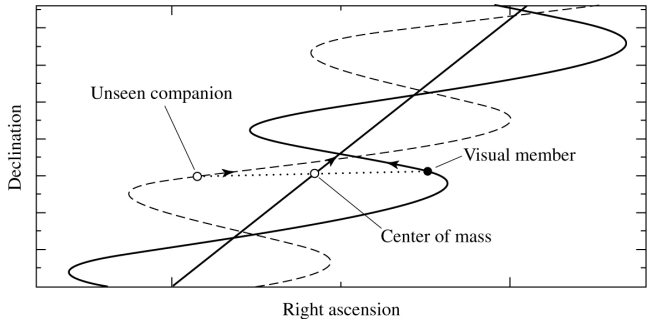

Figure 1.2: Astrometric binary. The unseen component is implied by the oscillatory motion of the observed element of the system (taken from Carroll & Ostlie (2006)).

Binaries	Visual	Spectroscopic	Eclipsing	Astrometric
P_{min}	1 yr	1 d	1 h	1 yr
P_{max}	-	30 yr	$\sim$ 1 yr	100 yr
i	yes	no	yes	yes

Table 1.1: Properties that might be derived from the different binary detection methods (Jorissen & Frankowski, 2008): P denotes the period and i the inclination.

For some binary systems only one star can be seen to wobble around a point in space (see Fig. 1.2), with no visible companion. For these **astrometric binaries**, the companion could be very faint, masked by the glare of its primary, or it could be an object that emits little or no electromagnetic radiation. Only the inclination and the semi-major axis of the whole system can be determined with this method (see Tab. 1.1 column 5).

Summarising, each method to detect a binary system has its restrictions in the availability of the different parameters. In addition, often not available or error-prone parameters like the distance from the sun to the system are necessary to derive certain values. Therefore, the results of different observational methods cannot be easily compared to each other.

1.2 Binaries in the field

To investigate a whole population of binary systems the binary frequency distribution and the distribution of the binary parameters is necessary. As we saw in Sec. 1.1, especial care has to be taken to compare or combine surveys. Furthermore, depending on the observed region and used methods, the conclusions of observations cannot be generalised.

Most binary population observations consider the field population, which consists of stars born in the field, ejected from a stellar cluster or resulting from the dissolution of different stellar

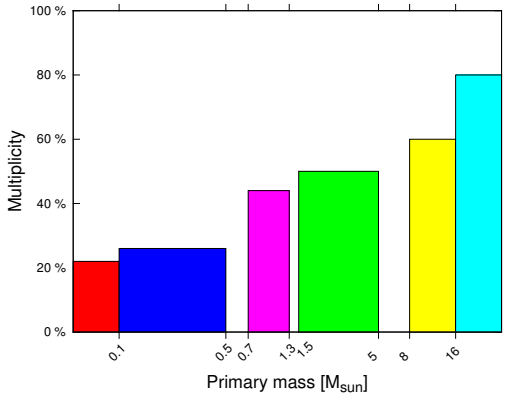

Figure 1.3: Multiplicity of population I main-sequence stars and field brown dwarfs for different primary masses The values were taken from Duchêne & Kraus (2013), who combined and updated several binary surveys, resulting in differences to the multiplicities given for a single survey in the text.

clusters (Goodwin, 2010). In the here investigated context, the field population is restricted due to observations and thus consists of all stars in the Milky Way close enough to be resolved as binary systems (see Sec. 1.1). The binary properties of this field population, and the main-sequence stars there, have been observed in several surveys targeting different primary mass ranges, which will be reviewed in the following. Eccentricity and mass-ratio distributions are seldom observed and the existing observations lead to an inconclusive results. Thus, only the multiplicity and period distribution depending on the primary mass are presented here.

In theses surveys, often the multiplicity, rather than the binary fraction, is used to compare different populations. The multiplicity can be defined using the number of systems (single - S, binary - B, triple - T, quadruple - Q, ...) in a population:

$$\text{multiplicity} = \frac{B+T+Q+...}{S+B+T+Q+...} \tag{1.10}$$

and is an upper limit for the binarity of a stellar population.

Fischer & Marcy (1992) examined the field population of M-dwarfs ($0.1\ M_\odot < m_1 < 0.5\ M_\odot$) in a vicinity of 20 pc around the sun and found that $42 \pm 9\%$ of their sample are part of a multiple system. Reid & Gizis (1997) performed a study for M-dwarfs within a distance of only up to 8 pc from the sun and determined a slightly lower multiplicity rate of 35%.

However, the multiplicity seems to depend strongly on the mass of the stars. Duquennoy & Mayor (1991) observed more massive solar-type stars (G-dwarfs $0.7\ M_\odot < m_1 < 1.3\ M_\odot$) in the solar neighbourhood ($r \leq 22$ pc) with CORAVEL radial velocity measurements and obtained a multiplicity of $\sim 60\%$. Thy restricted their sample to systems with $m_2/m_1 > 0.1$, where m_1 is the

primary (brighter / more massive) and m_2 the secondary (less bright / massive) star. More recent observations of Raghavan et al. (2010) considered a larger sample (454 stars within $r \leq 25$ pc), using different observational methods and various catalogues and radial-velocity monitoring programs. They determined the binary properties of solar-type stars ($\sim$ F6 $-$ K3) and found the fraction of binary stars to be 58%. For the very massive O-stars (> 16 M$_\odot$), the multiplicity seems to be even higher than for solar-type stars. Sana et al. (2012) observed O-stars and found a multiplicity of $\geq 80\%$. Figure 1.3 illustrates this increasing multiplicity with increasing primary mass, with typically 22% for brown dwarfs to at least 80% for high-mass stars. This means that for all primary masses, binary and higher order systems might have a huge impact on a stellar population. Therefore, the effect of binaries cannot be neglected when investigating stellar dynamics.

Also the period distributions differ for binary systems with different primary masses. The observations of binaries with solar-mass primaries of Duquennoy & Mayor (1991) and Raghavan et al. (2010) can be fitted with a Gaussian function of the form

$$f(\log P) \propto \exp\left\{\frac{-(\log P - \overline{\log P})^2}{2\sigma^2_{\log p}}\right\}, \tag{1.11}$$

(see Fig. 1.4a). Duquennoy & Mayor (1991) found a maximum of $\overline{\log P} = 4.8$ and a variance of $\sigma_{\log p} = 2.3$, with the period P in days. This values were corrected by Raghavan et al. (2010) to $\overline{\log P} = 5.03$ and $\sigma_{\log P} = 2.28$. The peak of the Gaussian fit of the period distribution of M-dwarfs by Fischer & Marcy (1992) is comparable to the results of G-dwarfs, but has a higher uncertainty (see Fig. 1.4b).

Figure 1.4c shows the period distribution of binary systems with A-type primary stars in the mass range 1.5 M$_\odot$ $< m_1 <$ 5 M$_\odot$. Carquillat & Prieur (2007) found an overabundance of short periods in spectroscopic binaries (pink in Fig. 1.4c). This confirms the finding of Abt & Levy (1985) (light blue in Fig. 1.4c), who studied 60 binary systems in the same mass range with spectroscopic and visual observation methods. It is important to notice that the observational methods limit the binary period to $< 10^4$ days and binaries only observable with other techniques are missing.

Figure 1.4d shows the cumulative period distribution for O-stars observed by Sana et al. (2012), which can be fitted using a power-law exponent of -0.55 ± 0.22. This period distribution significantly deviates from the period distribution resulting from Eq. 1.11 and shows a high percentage of close binary systems, which is equivalent to a lowering of the gradient towards higher periods in the cumulative plot (Fig. 1.4d). Again only binaries with periods $< 10^4$ days were observed in this survey and it remains unclear if larger periods are missing due to observational challenges or non existence.

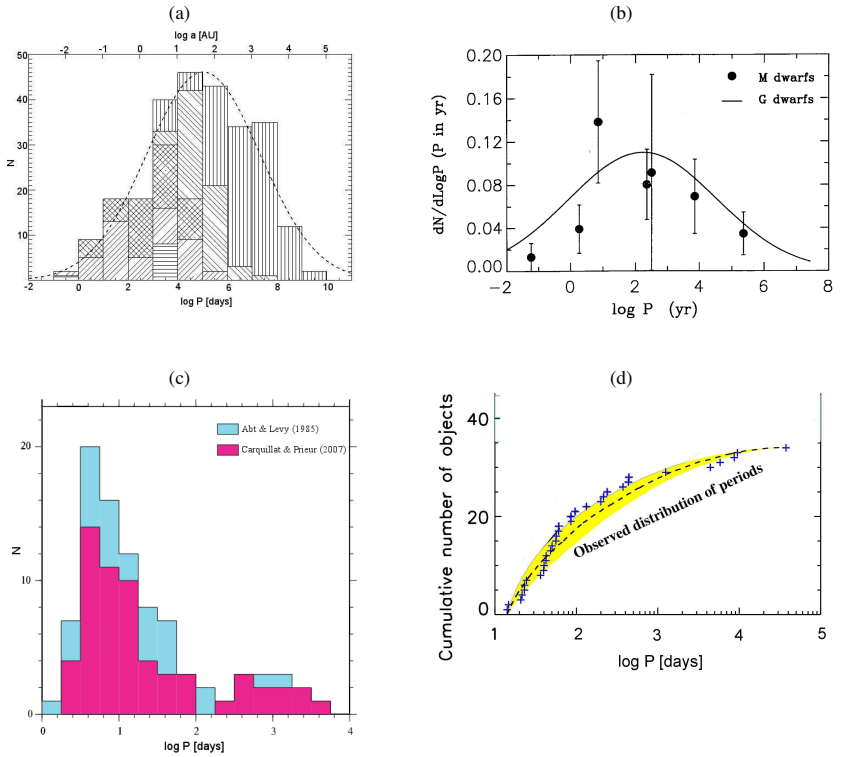

Figure 1.4: Period distribution of binary systems in different primary mass ranges and stellar types:
(a) F6-K3-dwarf primaries: A Gaussian fit to the data is plotted with $\overline{\log P} = 5.03$ and $\sigma_{\log P} = 2.28$. Image taken from Raghavan et al. (2010).
(b) M-dwarf primaries: The solid line shows the results for G-dwarfs of Duquennoy & Mayor (1991). Image taken from Fischer & Marcy (1992).
(c) A-star primaries: From spectroscopic and visual observations of binaries with $< 10^4$ days. Image taken from Carquillat & Prieur (2007)).
(d) O-star primaries: Cumulative distribution of binaries with $< 10^4$ days. Image taken from Sana et al. (2012).

Duchêne & Kraus (2013) reviewed recently the properties of main-sequence stars and brown dwarfs from the surveys mentioned above combined with data from Chini et al. (2012), Kraus et al. (2011), De Rosa et al. (2011), Kouwenhoven et al. (2005), and Abt et al. (1990). Figure 1.5 shows Gaussian fits to the observed period distributions of brown dwarfs (< 0.1 $M_\odot$, red line), low-mass stars ($0.1 - 0.5$ $M_\odot$, dark blue line) and solar-mass stars ($0.7 - 1.3$ $M_\odot$, magenta line). The maxima and widths of the distributions depend again on the primary mass. In the mass range $1.5 - 5$ $M_\odot$ the available data is sparse and two peaks are combined from different observations, suggesting a bi-modal fit (green line). For high-mass stars (> 16 $M_\odot$, light blue line) the Gaussian

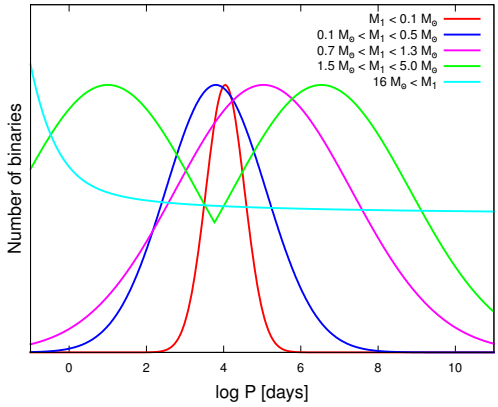

Figure 1.5: Combination of fits to period distributions in Fig. 1.4 of binary systems in different primary mass ranges and stellar types. The coloured mass ranges correspond to the colours in Fig. 1.3 (values taken from Duchêne & Kraus (2013) and references therein).

changes into a power law.

Thus, binary systems with different primary masses have distinct properties, suggesting that they form different or are processed in a different way or to a different degree during their evolution. Most likely the properties of binaries are changed during their early phase, where they are part of a star cluster. The formation of binary systems in such clusters is reviewed in the next section.

1.3 Formation on different scales

Stellar clusters are groups of stars, that form together within a small area. It is a point of discussion whether they are gravitationally bound at least in their formation phase. The cluster environment might be crucial for the development of stars and binary systems, since most, if not all stars form in such clusters (Lada & Lada, 2003). Star clusters form out of giant molecular clouds (GMCs), which are gravitationally bound entities of gas and dust with highly supersonic and turbulent velocity fields. The largest are cloud complexes with sizes of $20-80$ pc, temperatures of 15-20 K, velocities of 6-15 km/s^{-1} and particle densities of only 100-300 cm^{-3} (Padmanabhan, 2001). Within these complexes major fragments and single clouds with higher density and temperature exist. The smallest entity within a cloud are the clumps/cores with sizes of 0.05-1 pc from which stars form. There, temperatures up to 500 K, velocities of 1-10 km/s^{-1} and particle densities of $> 5 \cdot 10^9$cm^{-3} have been observed (Indriolo et al., 2013). Observations of many GMCs show dense gas and at the same time signs of star formation. This suggests that the stars form rapidly after the cloud has formed from the diffuse interstellar medium (Clark et al., 2005; Elmegreen,

2007). This opaque environment prohibits direct observation of the star formation process as much as the formation of binary systems.

1.3.1 Formation of single stars

Before looking at binary systems, here the formation process of single stars is summarised. The existing theory of star formation is well determined for low-mass stars (< 8 $M_\odot$), whereas the formation of high-mass stars (> 8 $M_\odot$) is still subject to current investigations. In the first stage of **low-mass star formation**, a so-called dark cloud core (Fig. 1.6a) forms from the molecular cloud. These cores collapse from an initial state determined approximately by the Jeans criterion (Fig. 1.6b). The minimum mass to fulfil this criterion is the Jeans mass M_J (e.g. Unsöld & Baschek, 2002), which decreases with decreasing temperature T and increasing density ρ:

$$M_J = \sqrt{\frac{3}{4\pi\rho}} \left(\frac{5kT}{G\mu}\right)^{3/2} \tag{1.12}$$

where k is the Boltzmann constant and μ the mass of one gas atom.

The density at the centre of these cores increases until it reaches a value of the order of 10^{11} cm^{-3}, where the central dense core of the cloud becomes opaque to the thermal infrared radiation from the dust grains. The thermal energy generated by the collapse being then no longer freely radiated away rises the temperature. The resulting thermal pressure might eventually halt the collapse. The so called hydrostatic core forms with a mass of about $5 \cdot 10^{-3}$ $M_\odot$, a radius of about 4 AU. However, the outer parts of the cloud continue to fall inwards and the hydrostatic core grows in mass by accreting more and more material. The density and temperature increase until, at a value of 2000 K, the hydrogen molecules begin to dissociate. This causes a second phase of dynamical collapse to begin at the centre of the core until the hydrogen at the centre is nearly all in atomic form.

The second hydrostatic core forms, which keeps growing in mass as material from the first core and cloud continues to fall in (Larson, 1973). This protostar (Fig. 1.6c), with a mass of $\sim 10^{-3}$ $M_\odot$, a radius of about 1 $R_\odot$ and a temperature of 2000 K is possibly surrounded by a disc, due to momentum conservation. During this stage the envelope material (first core and cloud) accretes onto the protostar or is swept away by characteristical bipolar outflows (Bachiller, 1996), which correlate with the onset of nuclear fusion. Then, the disc evolves around the now so-called T-Tauri star (Fig. 1.6d).

The disc accretion stops as soon as the star becomes a pre-main sequence star (Fig. 1.6e), where nuclear fusion and self-gravity become the only sources of energy. Now the star contracts, due to the loss of heat (Andre et al., 2000). According to the virial theorem, this energy is equally partitioned to increase the thermal energy and compensate the loss through radiation. Hence the

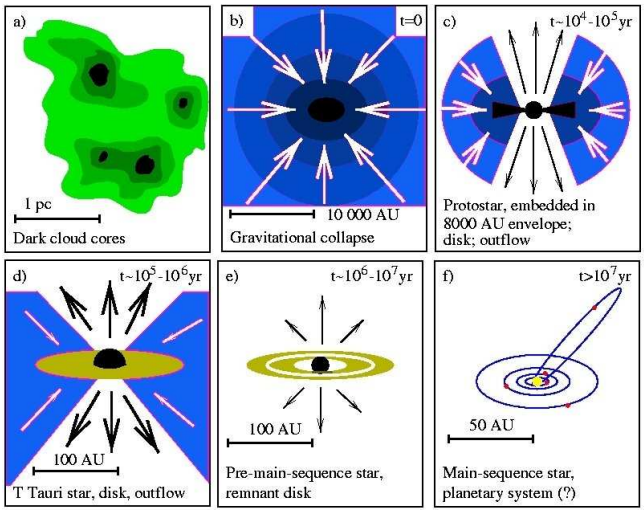

Figure 1.6: Star formation (image taken from Hogerheijde (1998) after Shu et al. (1987))

cooling of a star results in a rise of the internal temperature and negative heat capacity, on its way to becoming a main sequence star (Fig. 1.6f). Simultaneously the material in the disc might coagulate to form a single planet or even a planetary system (Shu et al., 1987). The above described process of star formation is believed to be valid for low-mass single stars.

The **formation of high-mass stars**, with masses higher than $\sim 8\,M_{\odot}$, is less well understood. Different formation models exist to overcome the pressure of the emitted radiation from the star, which pushes against the in-falling material.

For the so-called **core accretion** scenario, the radiation pressure has to be overcome, allowing the star to continue accretion. Theoretical work has shown that the production of a jet and outflow clears a cavity through which much of the radiation from a massive protostar can escape without hindering accretion from the disc onto the protostar (Banerjee & Pudritz, 2007; McKee & Tan, 2002). Thus, massive stars may be able to form using a mechanism similar to that of low-mass stars, because the spherical symmetry is broken.

When investigating the formation of massive stars, two differences to low-mass star formation have to be considered: (i) The star continues to accrete material while on the main-sequence (Kahn, 1974). (ii) The cores in which massive stars form are large enough that thermal motions are dominated by internal turbulence (Myers & Fuller, 1992; Caselli & Myers, 1995). The resulting 'turbulent core model' by McKee & Tan (2002, 2003) was able to overcome radiation pressure from a $\sim 100\,M_{\odot}$ protostar.

Additional processes are necessary to prevent the core from fragmenting and having enough material around from which they can accrete. In simulations, the fragmentation can be prevented

by surrounding lower-mass protostars (Krumholz & McKee, 2008) or magnetic field (Kunz & Mouschovias, 2009; Tan et al., 2013).

The necessary surrounding material could be provided by a disc (e.g. Kuiper et al., 2010, 2011). So far only a few observations are linked to discs around massive stars (e.g. Chini et al., 2004; Preibisch et al., 2011; Kraus et al., 2010; de Wit et al., 2011). This results from the discs diameters, which are typically ≤ 1000 AU Zhang et al. (2013) resulting in ≤ 0.5" at 2 kpc. Here instruments with high angular resolution like ALMA might provide more observations in the future.

Massive stars are usually found in a cluster environment. The theory of **competitive accretion** suggests that at birth all stars are much smaller than the typical stellar mass ($\approx 0.5\,M_\odot$), and that final stellar masses are achieved by the subsequent accretion of unbound gas. Stars with different stellar masses form when they are in a common gravitational potential and accrete from a distributed gaseous component. Hence, stars located near the center of the potential benefit from the gravitational attraction of the potential and accrete at much higher rates than isolated stars (Bonnell et al., 1997; Bonnell & Bate, 2006).

A third, mostly neglected massive star formation scenario is **coalescence** of two or more stars of lower mass. Bally & Zinnecker (2005) require for stellar merging by chance collisions a cluster density of the order of 10^8 stars pc^{-3} for the common formation of massive stars in less than 10^6 years. This density is 10^3 times higher than generally found in the cores of young stellar clusters. However, they predict a very short-lived and transient phase during which this high density is reached through contraction of the cluster's core. A second coalescence model which requires only a stellar densities of the order of 10^6 stars pc^{-3} was developed by Bonnell & Bate (2005). They predict a competitive accretion phase, in which a solar-mass binary system with separation of the order of 100 AU evolves to a binary system with separations of the order of 1 AU or less and masses of $10-30\,M_\odot$. These binaries typically have very eccentric orbits such that their periastron separation can be comparable to, or less than, the stellar radii, which might result in the merging of the binary system. Summarising, the common coalescence theories need very high stellar densities or a subsequent competitive accretion phase.

The evolution of stellar systems also influences the stellar radius. To visualise the radius evolution, Klassen et al. (2012) applied the stellar evolution model of Offner et al. (2009) to a star with a final mass of 100 $M_\odot$. Figure 1.7 shows the stellar evolution stages and their influence on the stellar radius. At stage 1 the object has collapsed to stellar densities and a radius of ~ 3 $R_\odot$ but the burning has not set in yet. Thus the radiation comes purely from gravitational contraction. The deuterium burning starts at stage 2 with $\sim 10^6$ K and in stage 3 the temperature rises again continuing the deuterium burning. The rising core temperature reduces the opacity and eventually the convection in the stellar core shuts down. At stage 4 the deuterium burns in a shell around the core and the radius contracts down from ~ 50 $R_\odot$ to a zero-age-main-sequence (ZAMS) radius

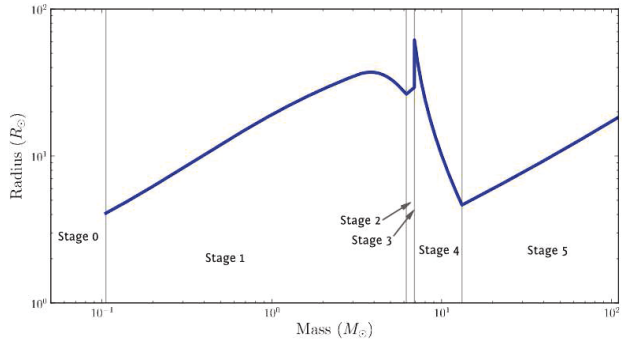

Figure 1.7: Radius evolution using the stellar evolution model of Offner et al. (2009). Image taken from Klassen et al. (2012).

of ~ 4 $R_\odot$. At the beginning of stage 5 the star has contracted enough to reach $\sim 10^7$ K. The hydrogen ignites and the star stabilises onto the main-sequence with a radius of ~ 20 $R_\odot$. These drastic variations in the stellar radius have to be taken into consideration when investigating stars which have not reached the main-sequence.

1.3.2 Formation of binary systems

Most of the stars are observed to be in multiple systems. Since a capture scenarios might be rare for sparse clusters or field stars, the formation of a binary system could also coincide with the star formation. Binary observation methods can only seldom observe binary systems during the formation (see Sec. 1.1). Thus, the formation of binary systems remains an open question. There are three possible formation scenarios that are considered to date for binary and multiple systems: (i) the fragmentation of a collapsing core, (ii) star formation inside a protostellar disc and (iii) dynamical formation in form of a capture process.

During the collapse of dense gas further **core fragmentation** can occur, which may lead to the formation of a binary system. Already Hoyle (1953) concluded, that a core will fragment further, as long as the gas remains optically thin and is able to cool efficiently. More recently, Inutsuka & Miyama (1992) and Tsuribe & Inutsuka (1999) showed, that the fragmentation of a collapsing, bound gas clump depends also on the ratio of thermal to gravitational energy $\alpha = 5c_s^2 r/(GM)$ and the ratio of rotational to gravitational energy $\beta = \Omega^2 R^3/(3GM)$, where c_s is the sound speed, R is the core radius, M the core mass, and Ω the orbital frequency of the core. For $\alpha\beta < 0.12$ and $\beta < 0.5$ cores are unstable. This restricts the possibilities of core fragmentation further, since only at a defined range in this parameter space fragmentation is possible. Turbulence is assumed to be an effective mechanism to produce situations which fulfil these restrictions. It induces over-densities or filamentary structures inside a core, which result in several collapses. Therefore,

Offner et al. (2009) and Offner et al. (2010) conclude that the turbulent fragmentation is the dominant mode of low-mass binary formation.

Alternatively, binaries could form due to **disc fragmentation**. As observations improve, more and more massive discs around young stars are observed at early epochs of star formation (Andrews & Williams, 2007; Andrews et al., 2009). In contrast to a disc which forms planets, these recent observed more massive discs, are able to form another star. The main discriminating feature between these low- and high-mass discs is the ratio between disc and stellar mass. While in pre-main sequence low-mass stars this ratio is < 0.1, for massive Young Steller Objects (YSO) the disc mass becomes comparable to or even greater than that of the star. Kratter et al. (2008, 2010) showed, that in such massive discs, the gas envelope of the star can feed the disc and induce instabilities which can trigger star formation. Fragmentation of the disc could lead to the formation of planets or even other stars. A disc fragments if the Toomre parameter falls below a critical value (Toomre, 1964):

$$Q_{crit} = \frac{c_s \kappa}{\pi \Sigma G} \ll 1 \tag{1.13}$$

where Σ is the surface density and κ is the epicyclic frequency, which is for Keplerian rotation equal to the rotation rate Ω. Additional to the small Toomre parameter, the cooling mechanism has to be fast. Gammie (2001) found $t_{cool}\Omega \leq 3$ as necessary condition, whereas other authors found that the critical cooling time depends on the equation of state of the gas, the thermal history of the gas, the distance from the central star, the local surface density or the stellar mass (Rice et al., 2005; Clarke et al., 2007; Meru & Bate, 2011).

The third scenario is the **capture** of one star by another in dense stellar environments. This can occur during the star formation process, where the surrounding disc assists the capture. Moeckel & Bally (2007) investigated discs which are representative for high-mass stars, within an environment of stellar density and velocity parameters like the Trapezium core, the central region of the Orion Nebular Cluster (ONC). They found that the capture rate after 1 Myr in this environment, could account for 50% of the massive stars having a companion. However, the binaries that form in their simulations have large semi-major axis and are perhaps easily disrupted. Even without discs, a transient binary system might form. In clusters like the Orion Nebular Cluster massive stars are most likely to form a binary star, whereas lower mass stars rarely do form binary or multiple systems (Pfalzner & Olczak, 2007).

It is still unclear which of these scenarios is the dominant one for binary system formation. In observations it is nearly impossible to observe the direct outcome of the star formation process. Hydro-dynamical simulations of star cluster formation by Bate (2009) produce no object that forms with a semi-major axis smaller than 10 AU, but after the complete cluster is formed many binary and triple systems with separations < 10 AU exist. Thus the processes during the early stages of stellar evolution seem to be important.

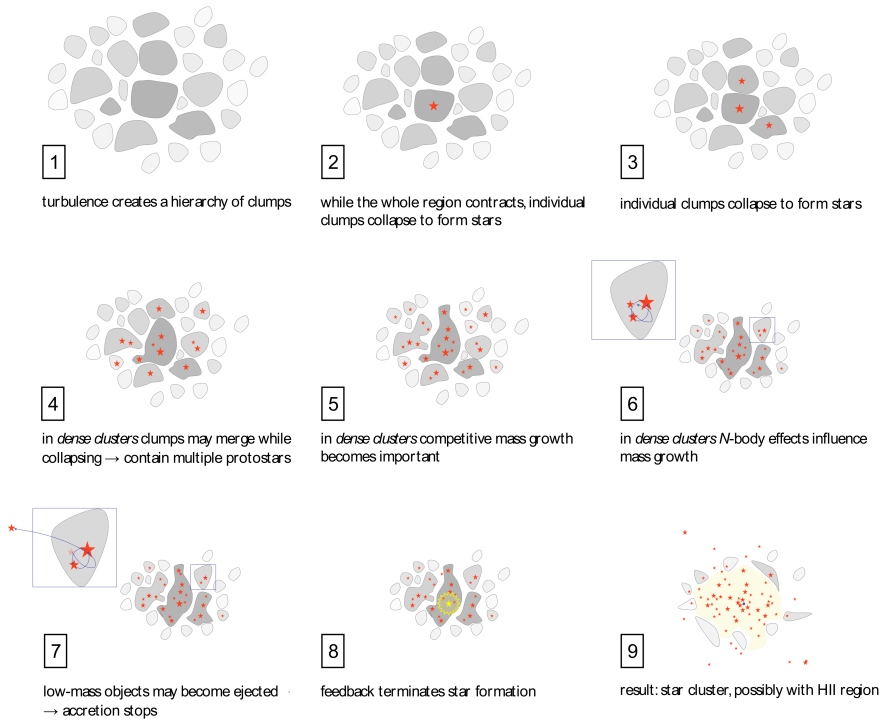

Figure 1.8: Cluster formation within a turbulent molecular cloud core (Image taken from Klessen (2011)).

1.3.3 Formation of stellar clusters

Since most stars and binary systems form in clusters, the question arises how such dense stellar environments form within the giant molecular clouds (GMCs). The turbulent dissipation timescales for GMCs are thought to be shorter than the cloud lifetime. This indicates that on global scales the clouds are stabilised against collapse by magnetic fields or internal turbulent pressure (Arons & Max, 1975; Myers & Goodman, 1988; Blitz, 1993). Physically, a collapse of dense gas occurs when the gravitational force exceeds the force of the gaseous pressure (Jeans criterion Eq. 1.12).

Cluster-forming cores experience significant fragmentation and gravitational instability, which leads to the formation of protostars. Numerical simulations (Klessen et al., 2000) suggest, that under typical molecular cloud conditions, a global GMC collapse can be prevented, but regions of enhanced density caused by strong shocks nevertheless can become gravitationally unstable and collapse. This results into the formation of dense cores which can decouple from the overall turbulent flow. Potential sites of cluster formation are the largest and most massive of these fragments. This process is depicted in Fig. 1.8, where the evolution of the cluster is followed until

the gas is removed. After the formation of the first stars (Fig. 1.8.1-3), the clumps created in the turbulent medium merge (Fig. 1.8.4) and accretion from a shared gas reservoir might increase the ability to accrete mass (competitive mass growth - Fig. 1.8.5). The interactions between the stars eject low-mass objects (Fig. 1.8.6-7) and the accretion stops. In the pictures 4-7 possible star-gas interactions are neglected and only the feedback which removes the gas (Fig. 1.8.8) and terminates star formation is included.

Observed cluster densities cover a wide range of possible values from 0.01 $M_{\odot}pc^{-3}$ up to 10^6 $M_{\odot}pc^{-3}$ at any cluster age (e.g. clusters in Wolff et al., 2006; Figer, 2008; Borissova et al., 2008). The same applies for the cluster size, which can vary from less than 0.1 pc up to more than ten pc. Pfalzner (2009) showed for observations of star clusters in the Milky Way, that the variety of observed cluster densities does not originate from an initial spread in the cluster densities but arises from two different cluster types. Her work reveals two distinct evolutionary tracks, which massive star clusters follow during their evolution. At the first evolutionary track, clusters start at very high densities of about 10^6 $M_{\odot}pc^{-3}$ and radii of about 0.1 pc and evolve to smaller densities of about 10^2 $M_{\odot}pc^{-3}$ and radii of a few pc and are called **compact clusters**. The evolution of clusters on the other track starts at densities below 10^2 $M_{\odot}pc^{-3}$ and radii of several pc and develops to densities well below 1 $M_{\odot}pc^{-3}$ and radii of several ten pc. These clusters are called **loose clusters** or OB associations. The evolution of both cluster types is characterised by an expansion of the cluster size and a resulting decrease of the cluster density over at least 20 Myr.

1.4 Binaries in young cluster environments

As shown in Sec. 1.2, multiplicities and period distributions are derived from main-sequence stars with most of them being part of the field distribution. To determine whether these properties of field stars are primordial or have developed from an initially different binary population, it is necessary to investigate the properties of young cluster binary populations. Since most of the stars and thus binary systems form in clusters (Lada & Lada, 2003), one ideally would like to use the observed initial properties of binaries in very young embedded clusters (< 0.1 Myr), because at such a young age the binary population is close to its primordial state. As we have seen in Sec. 1.1, the possibilities to observe binary properties are highly restricted for every observational method. Additionally, observations of binaries in such young dense embedded clusters face a number of observational difficulties such as absorption and scattering of the stellar radiation by dust and gas (extinction), crowding, and too low spatial resolution, which makes such observations nearly impossible. To simulate the influence of interactions between the stars including the gas, the populations of low density clusters are used to determine the initial conditions. It is assumed, that they are relatively unaffected by the influences of the stellar environment and therefore close to their primordial state. This neglects the possibility that different types of binaries might form

in less dense systems compared to dense systems. Caused by the low stellar density, wide binary systems might be more common, whereas close binary systems might be seldom.

Clusters show a typical distribution of masses of stars - the so-called **stellar initial mass function (IMF)**. It describes the initial stellar population in a young cluster and represents the outcome of the star formation process. Understanding the origin of the IMF means understanding the star formation process itself. Salpeter (1955) first quantified the IMF and suggested a power law of the form $f_m(m) \propto m^{-2.35}$. More recent investigations suggest a shallower dependence in the low-mass regime (Kroupa, 2001; Chabrier, 2001, 2002; Maschberger, 2013). This can be described with a multi-part power law

$$f_m(m) = k \begin{cases} \left(\frac{m}{0.08}\right)^{-0.3\pm0.7}, & 0.01\ \mathrm{M}_\odot \leq m < 0.08\ \mathrm{M}_\odot, \\ \left(\frac{m}{0.08}\right)^{-1.3\pm0.5}, & 0.08\ \mathrm{M}_\odot \leq m < 0.50\ \mathrm{M}_\odot, \\ \left(\frac{m}{0.08}\right)^{-2.3\pm0.7}, & 0.50\ \mathrm{M}_\odot \leq m < 150\ \mathrm{M}_\odot, \end{cases} \tag{1.14}$$

where k contains the desired scaling to describe the IMF over the entire range from the brown dwarf regime to high-mass stars (Kroupa, 2001). In the context of binaries it should be noted that the observational problem of unresolved binaries increases the inaccuracy of the IMF, leading to an overestimation of stellar masses.

One often used numerical way to produce a **mass-ratio distribution** of binaries is to randomly associate masses from the IMF (Kroupa, 1998). This means, that the stellar population is generated to fulfil the chosen IMF and two stellar masses from this population are randomly associated as a binary system until the chosen binary frequency is reached. By contrast, Kouwenhoven et al. (2007) characterised the binary population in the young and nearby OB association Scorpius OB2 using available observations of visual, spectroscopic, and astrometric binaries with intermediate-mass primaries. They found a mass-ratio distribution of the form

$$f_q(q) \propto q^{-0.4}. \tag{1.15}$$

Kouwenhoven et al. (2009) showed that this mass-ratio distribution reproduces the observations better than a random distribution. Since Scorpius OB2 is a young (5-20 Myr) association with a low stellar density ($\leq 0.1\ \mathrm{M}_\odot\mathrm{pc}^{-3}$), its current population is expected to be similar to the primordial population.

For the **eccentricity distribution** the information is more spares. Ambartsumian (1937) analytically calculated a thermal distribution with $f(e) = 2e$. Kouwenhoven et al. (2007) considered both the thermal distribution and a flat distribution $f(e) = 1$ for their observations, but concludes, that further radial velocity and astrometric surveys are necessary to characterise the underlying

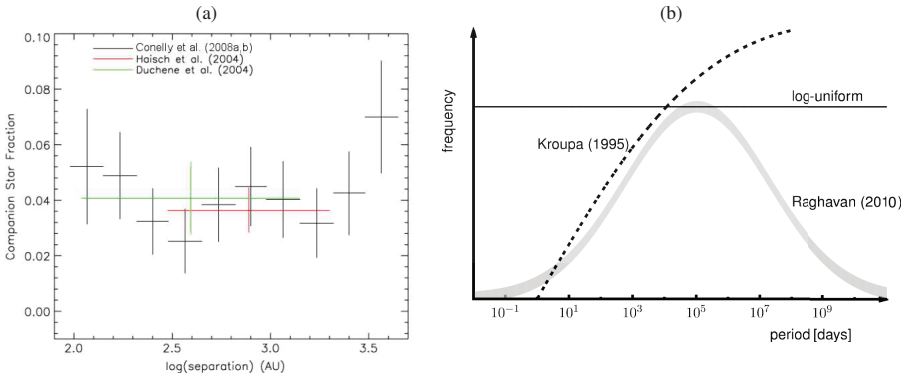

Figure 1.9: Observational and theoretical possible initial period distributions.
(a) The observations of young star-forming regions suggest a log-uniform initial period distribution. Image taken from Reipurth et al. (2014).
(b) Depending on the starting point of a simulation, the initial period distribution is chosen to be log-normal (thick grey line), rising (thick dashed line) or log-uniform (solid line). Image taken from Korntreff et al. (2012).

eccentricity distribution of Scorpius OB2.

Kouwenhoven et al. (2007) derived from the young association Scorpius OB2 also a **semi-major axis distribution** of the form:

$$f_a(a) \propto a^{-1}. \tag{1.16}$$

This distribution is limited to $a \in [0.02\,\mathrm{AU}, 10^5\,\mathrm{AU}]$. The limits represent the maximum separation at which binaries are (quasi-) stable in the galactic tidal field and a minimum separation, at which binary systems do not merge (for further information on binary merging see Sec. 1.5).

For a given stellar mass, this log-uniform semi-major axis distribution translates in a log-uniform period distribution using the Kepler equation (Eq. 1.4). Connelley et al. (2008a,b) confirm this finding in very young populations in Taurus, Ophiuchus, and Orion star-forming regions (see Fig. 1.9a). With the denser Orion Nebula Cluster excluded, these are all young populations in sparse regions. However, even in denser regions, an originally log-uniform period distribution is likely. For example, the HST observations by Reipurth et al. (2007) of binaries in the Orion Nebula Cluster (ONC) demonstrate that the semi-major axis distribution deviates from the log-normal distribution of the field period distribution (see Sec. 1.2) and is closer to a log-uniform distribution. Another example for an initial binary population, which is often use is a rising period distribution (dotted line in Fig. 1.9b) developed by Kroupa (1995a). For this distribution a pre-main sequence eigenevolution is assumed which is a primarily phenomenological model and not developed on the

basis of pre-main sequence observation data. Overall, no obvious mass dependency of the initial period distribution exist, which might be caused by the difficulties to observe still embedded stars.

In contrast to that the period distribution in the field has a rather different shape and depends on the mass of the binary system. For example, the period distribution of solar-mass primaries has a Gaussian shape in the field (grey line in Fig. 1.9b), but a log-uniform shape in young clusters. Thus, the detected period distributions in the field have to be a result of processes affecting binary systems during their evolution. Choosing an initial period distribution for a simulation depends on the evolutionary point at which the simulation stars. If gas is excluded from the simulation, the rising period distribution (dotted line in Fig. 1.9b) seems to be a reasonable choice, and for simulations of the field, the observations by Raghavan et al. (2010) can be chosen (grey line in Fig. 1.9b). However, for an initial period distribution which has not been processed by gas jet, the log-uniform distribution (solid line in Fig. 1.9b) matches best with observations of protostars (Fig. 1.9a).

1.5 Evolution of binary systems in a cluster environment

The environment influences a binary system considerably during its development. For the first $1-5\,\mathrm{Myr}$, stellar clusters are still embedded in their natal gas (Leisawitz et al., 1989). This is caused by the rather ineffective star formation process, because even within the dense clumps, in which clusters form, the star formation efficiency (SFE) does not reach 100% . Since the SFE is the fraction of stellar mass in a cluster divided by the total mass of stars and gas in the cluster, not all of the initial gas is used to form stars. The remaining gas is expelled from the cluster due to stellar feedback (e.g. Whitworth, 1979; Pelupessy & Portegies Zwart, 2012; Dale et al., 2012), low-mass star outflows (Matzner & McKee, 2000), and if massive stars exist, their photo-ionisation and supernova feedback (Zwicky, 1953; Eggleton, 2006). The resulting exposed clusters have initially still high stellar densities but expand rapidly until they find a new equilibrium state (Pfalzner, 2009).

The processes affecting binary systems can be divided in three types of interactions: The binary system interacts (i) with other stars, (ii) with the gas in the early embedded phase and (iii) with itself through mass transport between the two stars during the late stages of stellar evolution.

The latter type of interactions is mainly Roche lobe overflow (Paczynski, 1971), which is the mass transfer from one binary component to the other if its radius exceeds the Roche lobe. This is the point, where the gravitational pull of the stellar companion becomes dominant and mass is transferred either to the companion star itself or to the companion circumstellar disc. The mass transfers through the apex of the Roche lobe, which is the first Lagrangian point (for more details see Ivanova et al. (2013) and references therein). This mainly happens at late stages of stellar evolution (>5 Myr) or during a binary merger. In this thesis only the early stages of

stellar evolution are considered and thus only the two other interaction types are discussed in the following sections.

1.5.1 Dynamical evolution in a cluster environment

It is long known that binaries can be dynamically disrupted by three- and four-body interactions. These disruptions affect mostly wide binary systems (Heggie, 1975). The general effect of three-body interactions onto a binary can be described by looking at the energy of the star which interacts with the binary system. If after the interaction the star is slower than before, the internal energy of the binary increases due to energy conservation. This results in a wider binary system. On the other hand, in case of hardening a binary system the internal energy has to be reduced, which results in a higher velocity for the interacting star. From this, two types of binaries can be defined: **soft binaries** which become wider following three-body interactions and **hard binaries** which reduce their orbit following three-body scattering.

Three-body and even higher order interactions occur very often in star clusters during their lifetimes (Heggie, 1975). Therefor, it is not possible to calculate the changes of the binary population in the clusters analytically but numerical simulations have to be performed (e.g. Aarseth, 1971; Kroupa, 1995b; Kroupa & Burkert, 2001; Kroupa & Bouvier, 2003; Pfalzner & Olczak, 2007; Parker et al., 2009; Kouwenhoven et al., 2010; Marks et al., 2011). With simulations developed in the early 1960's, only the evolution of clusters with a very limited number of stars (e.g. Aarseth, 1963, with 25-100 stars) was possible. Due to improvements of the numerical techniques and of the computing hardware, simulations of up to several 100 stars for several 10^5 Myr (e.g. Banerjee et al., 2012) or several 10^5 stars for several 100 Myr can be performed nowadays.

Performing N-body simulations, Kroupa (1995a,b) showed that to reproduce the observed log-normal distribution of the field population, the initial number of wide binaries has to be significantly higher than observed, if all binaries are subject to dynamical evolution in a star cluster.

1.5.2 Binaries embedded in gas

Stars and thus binary systems do not only interact with each other, but also with their surrounding gas. Only recently Stahler (2010) suggest that the oscillating gravitational potential of a binary system would lead to a decrease in the binary orbit. The reason for this orbital decay is, that the binary potential torques the nearby gas, producing an outgoing acoustic wave and thus transports angular momentum from the binary to the gas. Figure 1.10 shows a sketch of a binary system with an outgoing acoustic wave. Each star launches an acoustic wave resulting in a spiral density wave with a wavelength of $\lambda = 2\pi c_s/\omega$, where ω is the angular rotation rate of the binary system and c_s the sound speed of the surrounding gas. As shown in the sketch, the outgoing acoustic wave is evaluated in the far field. However, the amplitude of this wave is calculated with a starting point

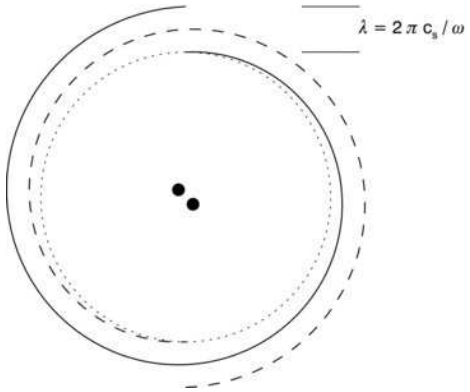

Figure 1.10: Binary system with two outgoing acoustic waves (solid and dashed lines), resulting in a wavelength of $\lambda = 2\pi c_s/\omega$. Image taken from Stahler (2010).

at the location of each star of the binary system, neglecting all processes which might dominate in this region (see Sec. 1.5.3).

Therefore, his analytic approach requires a number of approximations: (i) the wave generation itself is neglected and only the far-field considered, (ii) the binary orbit is assumed to be circular, (iii) the gas to be uniformly distributed, and (iv) the orbital velocity of the stars in the binary system to be higher than the sound speed of the gas.

The binary system is evaluated as a source of acoustic waves using circular orbits with radii a_1 and a_2 about the mutual centre. Starting with a given system mass, mass-ratio, semi-major axis and gas density of ρ_0, Stahler uses the linear approximation of the momentum conservation valid for small disturbances

$$\frac{\partial \vec{u_1}}{\partial t} = -\frac{c_s^2}{\rho_0}\nabla\rho_1 - \nabla\Phi_{binary}, \tag{1.17}$$

where $\vec{u_1}$ is the small induced velocity with corresponding density perturbation ρ_1 due to the binary potential Φ_{binary}. Furthermore, he uses the linearised equation of mass continuity

$$\frac{\partial \rho_1}{\partial t} + \rho_0 \nabla \vec{u_1} = 0. \tag{1.18}$$

The $\nabla\Phi_{binary}$-term in the momentum equation is relatively small, but cannot be discarded, as it describes the stellar gravity that is responsible for the excited waves. After calculating the resulting velocities of the gas and the reduced angular momentum of the binary system, Stahler obtains a

linear time dependence for the semi-major axis of the form

$$a_{tot} = a_0 \left(1 - \frac{t}{t_c}\right), \tag{1.19}$$

where a_0 is the initial binary separation, t the time and t_c is the so-called coalescence time, which is given by

$$t_c = \frac{15}{32\pi} \frac{(1+q)^2}{q} \frac{c_s^5}{\rho_0} \frac{a_0}{G^3 M_{\rm sys}^2} \tag{1.20}$$

with $q = m_1/m_2 \leq 1$.

In extreme cases the orbit does not only decrease, but an actual merger of the two stars can happen. For example, for an equal mass binary system with the total mass of 1 $M_\odot$ and a semi-major axis of 100 AU, surrounded by a gas with a sound speed of 2 km/s and a density of 10^7 cm^{-3}, Stahler's approximation predicts a merger within 1 Myr due to gas-induced orbital decay. In this context the stellar mass of each component is modelled as a point mass. Thus, a binary system is assumed to have merged, when the distance between the two stars is zero. This neglects, the highly variable radius of protostars (see Fig. 1.7) and processes like the Roche lobe overflow.

1.5.3 Disc formation, binary-disc interaction and accretion

Observations show that binary systems can be surrounded by a gaseous circumbinary disc. These discs were detected in low-mass systems (e.g. Garcia et al., 2013) as well as in high-mass systems (e.g. Sánchez-Monge et al., 2013). Even planets can form in such circumbinary discs (Doyle et al., 2011; Orosz et al., 2012a,b; Welsh et al., 2012).

Bate & Bonnell (1997) simulated the circumbinary disc formation for a binary system in a non-self-gravitating gas. In their simulation, the formation of such a circumbinary disc starts, if the specific angular momentum of the in-falling gas is high enough to stabilise a circular orbit outside of that of the secondary star, around the centre of mass. Including a magnetic field and a much higher ratio of rotational to gravitational energy, Zhao et al. (2013) and Zhao & Li (2013) showed, that rather a collapsing pseudo-disc is formed, whose rotation is strongly braked. For example, for an initial binary separation of 240 AU, the binary separation decays strongly in their simulation, resulting in a binary separation of $20-40$ AU after 0.8 Myr depending on the angle between the rotation axis and the magnetic field lines. Therefore they concluded, that the formation of the circumbinary disc and the semi-major axis evolution depends strongly on the ratio of rotational to gravitational energy.

The interaction of binary stars with the surrounding disc or molecular cloud includes many different physical processes and can be divided in several regions (see Fig. 1.11): A common

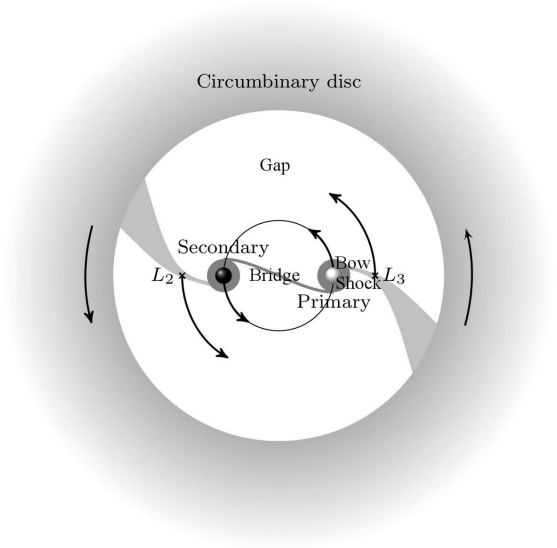

Figure 1.11: Diagram of a gravitationally bound binary system on a circular orbit surrounded by a circumbinary disc in Keplerian rotation. The gravitational interaction creates a central cavity (gap) at the tidal truncation radius. Local circumstellar discs form around each star from material from the circumbinary disc through the Lagrangian points L_2 and L_3. Image taken from de Val-Borro et al. (2011).

envelope around the binary system, bow shocks in front of the stars, a region of reduced density in the central part of the system (gap), the discs of the components, and a stationary shock between them having the form of a bridge. The spiral bow shocks form as a result of the supersonic motion of the circumstellar discs in the inter-component envelope. The presence of shocks leads to a redistribution of angular momentum in the common envelope, and the formation of the gap in the central part of the circumbinary disc. (de Val-Borro et al. (2011), Sytov et al. (2011) and references therein).

The radius where this gap ends and the circumbinary disc starts has been observed in only a few binary systems. This inner gas radius lies between two and four semi-major axis in binary systems with semi-major axis smaller than 1.1AU (Jensen & Mathieu, 1997; Najita et al., 2003; Jensen et al., 2007; Boden et al., 2009). Additionally, this inner radius of the circumbinary disc has been determined by hydrodynamic (HD) simulations to have a radius between 1.8 and 4 semi-major axis from the centre of mass of the binary system, depending on the binary geometry (Artymowicz & Lubow, 1994; Fateeva et al., 2011; Bisikalo et al., 2012). This is consistent with more recent three-dimensional magneto-hydrodynamic (MHD) simulations of circumbinary discs (Shi et al., 2012), where a gap with a radius of two semi-major axis of the binary system was found. Some simulations suggest, that this inner radius depends also on the mass-ratio and eccentricity of the

binary system, but so far only a few cases were simulated and no general dependency was found.

In all of these simulations usually only the mass transfer (accretion) from the discs onto the binary system is considered. Being computational expensive, these simulations keep the semi-mayor axis constant, simulating only the gas close to the stars, and/or consider only a few rotations of the binary system, corresponding to a time span of less than 0.1 Myr.

In contrast simulations with a changing semi-major axis were performed by Artymowicz et al. (1991). Their smoothed particle hydrodynamic (SPH) simulations show an angular momentum loss of the binary due to the strong torque of the binary. As a result the separation is reduced and additionally they found an increased eccentricity. These simulations are computationally expensive and only few special cases have been considered. In MHD simulations of Shi et al. (2012), it was shown, that for circular binary systems the angular momentum gained through accretion and the angular momentum loss due to the torques is nearly balanced. It is important to notice, that these simulations only consider a few examples of binary systems (mostly system masses $\leq 1\ M_\odot$) and no complete parameter study has been carried out so far.

In close binary systems, in addition to accretion and angular momentum transfer, tidal interactions become important. Zahn & Bouchet (1989) calculated that for pre-main sequence binaries with masses ranging from 0.5 $M_\odot$ to 1.25 $M_\odot$, circularisation takes place for periods $\lesssim 8$ days. Their theory is based on radiative damping of dynamic tides in the outer, non-adiabatic layers of the envelope of stars in close binary systems and seems to agree well with observations (Khaliullin & Khaliullina, 2010).

If the stellar radius even extends beyond its Roche lobe, mass is transferred between the two stars via their first Lagrangian point. A theoretical study of long-term behaviour of circular and eccentric systems, including stellar radiation, shows that the mass donor becomes small and underluminous, while the converse is the case for the accretor (Davis et al., 2013).

1.6 Thesis structure

In the above described context the here presented work addresses the following topics:

To investigate the evolution of a binary population, solar-mass star were investigated first, since here recent surveys exists. The dynamical stellar evolution in a cluster environment (Sec. 1.5.1) and the gas-induced orbital decay (Sec. 1.5.2) were combined in Chap. 2. It was found that for solar-mass stars, this could reshape the initial binary period distribution found in young clusters (Sec. 1.4) to the older distribution observed in the field (Sec. 1.2). In contrast, it is shown that the observations of other mass ranges cannot be reproduced with this analytic approximation.

As mentioned in Sec. 1.5.2 many approximations are necessary to calculate the orbital decay analytically. In a next step it is investigated how these approximations influence the result. This is done by means of hydro dynamical simulations of the dynamics of a single binary surrounded by gas. The development of such a hydro dynamical simulation code and simple physical test problems are described (see Chap. 3).

In Chap. 4 the results of these simulations are compared to the analytic approximation by Stahler. It is found, that the orbit decays much slower in the simulation than predicted by the analytic model. The main reason is that the wave generation mechanism and the changing binary parameters were included directly. Apart from requiring fewer approximations, the simulations have the advantage that the method can be extended to binary systems with eccentric orbits. It is shown, that eccentric orbits result in a faster decay than circular orbits. Chapter 5 discusses the implications of these results for the evolution of a cluster binary population. There, only one example is given, since the huge parameter space of binary and gas properties needs to be restricted by future observations.

2 Binary evolution in an ONC-like star cluster

In a first approach to understand the evolution of binary populations, I focus on solar-type stars. Even if most of all stars have masses around 0.5 $M_\odot$, observations of solar-mass stars in the vicinity of 25 pc are more complete. This is caused by their higher luminosity compared to stars with masses around 0.5 $M_\odot$, resulting in less problems with extinction. On the other hand, solar-mass stars remain in the main-sequence phase for up to 10^6 Myr, contrary to more massive stars with masses > 16 $M_\odot$ which have a main-sequence lifetime of a few Myr. This results in more stars around 0.5 $M_\odot$ being observable at a certain time and thus a better statistic.

Duquennoy & Mayor (1991) were the first to observe a log-normal period distribution of solar-mass main-sequence stars in the field. In a recent more complete study Raghavan et al. (2010) confirmed the log-normal period distribution. They observed 454 main-sequence stars of the spectral types F6-K3 and their lower mass companions, which roughly correspond to binary systems with primary masses in the range of $0.5\ M_\odot \leq m_1 \leq 1.5\ M_\odot$.

This observed log-normal period distribution in the field is in contrast to binaries in young star clusters where observations indicate that the period distribution is log-uniform (see Sec. 1.4). Processes like dynamical binary destruction caused by three-body interactions (Sec. 1.5.1), gas-induced orbital decay (Sec. 1.5.2) or binary-disc interactions (Sec. 1.5.3) are thought to be responsible for the change of the period distribution with time. In collaboration with T. Kaczmarek, I investigated the relative importance and affected regime of binary periods due to the former two processes.

T. Kaczmarek studied the influence of stellar interactions on binary systems in such dense cluster environments (here after called 'dynamical'). He did this by performing simulations of star cluster dynamics using N-body methods. In Sec. 2.2 the results of these simulations are presented. Complementary, I considered how the natal gas environment could alter the binary distribution. The method for this investigation, which was also used in my diploma thesis "Gas-induced orbital decay of binary systems in young embedded clusters" is summarised in Sec. 2.3. Combining the results of Sec. 2.2 and Sec. 2.3, we determined the total effect of the dynamical interactions and the influence of the gas on the binary properties in Sec. 2.4. In Sec. 2.5, the effect of orbital decay is evaluated for M-dwarfs, B- and O-stars and compared to observations. The limitations and shortcomings of this method are discussed in Sec. 2.6.

2.1 Cluster model

To allow a comparison of dynamical interactions and gas-induced orbital decay, the Orion Nebula Cluster (ONC) was chosen as a common model star cluster. It is one of the best-studied high-density clusters due to its vicinity of 414 pc to the sun (Menten et al., 2007). The ONC consists of about 4000 systems in the mass range $0.08\,\mathrm{M}_\odot \leq M_{star} \leq 50\,\mathrm{M}_\odot$, of which 30 are O- and B-stars (Hillenbrand, 1997). Studies on the stellar mass distribution (e.g. Hillenbrand & Carpenter, 2000) reveal it to be close to the canonical stellar IMF given by Eq. 1.14. Observational studies found for massive stars on average 2.5 companions (e.g. Grellmann et al., 2013) and a varying binary frequency from $\approx 50\%$ for solar mass stars to $\approx 75\%$ for massive stars (Preibisch et al., 1999; Köhler et al., 2006).

Many young dense clusters, including the ONC, are observed to be mass-segregated (Hillenbrand & Hartmann, 1998), meaning, that the most massive stars are found preferentially close to the cluster centre. Bonnell & Davies (1998) found that the observed mass segregation of the ONC is unlikely the result of the dynamical evolution of the cluster but primordial.

The ONC has also been investigated theoretically by means of simulations. Olczak et al. (2010) showed that the initial three-dimensional stellar density distribution

$$\rho_{\mathrm{star}}(r) \propto \begin{cases} (r/R_{\mathrm{core}})^{-2.3}, & 0 < r \leq R_{\mathrm{core}} \\ (r/R_{\mathrm{core}})^{-2.0}, & R_{\mathrm{core}} < r \leq R \\ 0, & R < r \leq \infty, \end{cases} \tag{2.1}$$

with a cluster core radius of $R_{\mathrm{core}} = 0.2$ pc and a cluster size of $R = 2.5$ pc, evolves into the current density distribution of the ONC after a simulation time of 1 Myr. They assumed that the cluster is initially in virial equilibrium and neglected primordial binary systems. The adopted model starts from a situation where all stars have already been formed. Figure 2.1 shows this initial density distribution (blue line) and the resulting distribution after 1 Myr (red line), which is a good fit to the observations (circles and dots).

Following these observations and simulations, the initial state of the here used model cluster can be described using mass segregation within the stellar density distribution specified above. To reproduce the observed mass segregation in the cluster simulations and to calculate the gas influence in Sec. 2.3, the most massive binary system is initially placed at the cluster centre. Additionally, the three next most massive systems are placed at random positions within a sphere of radius $R = 0.6\,\mathrm{R}_{\mathrm{hm}}$ around the cluster centre, where R_{hm} is the cluster half-mass radius of the cluster.

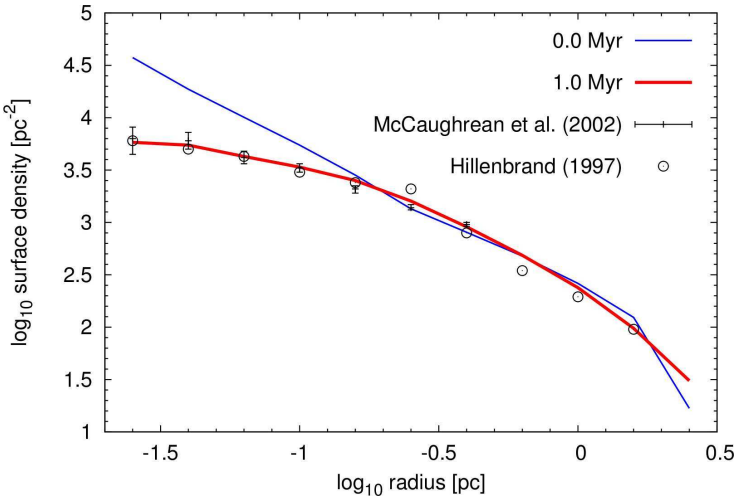

Figure 2.1: Projected density profiles from simulations compared to observational data (image taken from Olczak et al. (2010)). The initial profile (blue line) and the profile at a simulation time of 1 Myr (red line) are shown. The observational data are from a compilation of McCaughrean et al. (2002) and include also the values given by Hillenbrand (1997).

As suggested by the observations of Hillenbrand & Carpenter (2000), the system masses are sampled from the stellar IMF given by Eq. 1.14. They are limited to $[0.08\,\mathrm{M}_\odot, 50\,\mathrm{M}_\odot]$, where the upper mass limit corresponds to the mass of the most massive binary system in the ONC. The lower limit is the hydrogen burning limit, thus the margin between sub-stellar and stellar objects.

In contrast to the simulations by Olczak et al. (2010), the primordial binary frequency was assumed to be 100%, since the binary evolution is the prime focus here. This initial binary frequency is higher than observed, since the observed binary frequency results from a binary population probably already processed by dynamical interactions and gas-induced orbital decay. A binary frequency of 100% means that each star is initially part of a binary system. Thus, every system mass, sampled from the IMF, was split into the two binary components $M_{\mathrm{sys}} = m_1 + m_2$.

For the initial binary semi-major axis and mass-ratio distribution, the properties of Scorpius OB2 were used (see Sec. 1.4). This OB association has an age of $5-20$ Myr, but such binary populations are assumed to remain mostly unevolved (Kroupa & Bouvier, 2003). It remains unclear if this is the case, since recent theories of cluster evolution contradict this. Pfalzner (2011) shows, that denser clusters expand after gas-expulsion leading to the associations observed today.

In the absence of observations of younger binary populations, the above mentioned Scorpius OB2 observations are used. Thus, the initial binary properties are a primordial mass-ratio distribution of $f_q(q) \propto q^{0.4}$ with $q = m_2/m_1 \in [0,1]$ and a log-uniform primordial semi-major axis distribution $f_a(a) \propto d\mathrm{N}/da \propto a^{-1}$ where $a \in [0.02\,\mathrm{AU}, 10000\,\mathrm{AU}]$. Besides the observations in

OB associations, the log-uniform distribution was used here to test, whether the here investigated effects of cluster dynamics (Sec. 2.2) and gas-induced orbital decay (Sec. 2.3) can lead to the log-normal distribution observed in the field, when assuming this extreme initial period distribution This cluster setup is now used to study the past and future evolution of the ONC.

2.2 Dynamical evolution

Kaczmarek (2012) investigated the dynamical evolution of a binary population during the first 3 Myr. In this simulations the natal gas, in which the cluster is still embedded during $\approx$ 1Myr, is neglected. He used an ONC-like cluster, which is a cluster having the properties of the ONC described in Sec 2.1. In contrast to other simulation which used a initially rising period distribution (see Sec. 1.5.1) to investigated the evolution of primordial binary populations, he used a log-uniform initial period distribution, as suggested by observations of sparse clusters (Sec. 1.4 and 2.1).

The dynamical evolution of such a cluster was simulated, using the NBODY6 code by Aarseth (2003). This parallel, high-precision, direct N-body code follows the gravitational interactions of the stars constituting the model cluster. Beside the mass segregation, the initial positions and velocities of the stars are randomly distributed with respect to the chosen density and velocity distribution. It is possible that these random distribution results in over-densities in the cluster, which then dominate the cluster evolution. Thus, to improve statistics and ensure that the results are independent from this initial positions and velocities, 50 realisations of the same cluster were simulated and the results averaged. For a more detailed description of the simulation method see Kaczmarek et al. (2011).

The simulation results of Kaczmarek (2012) show a destruction of wide binary systems due to dynamical interactions with other cluster members. Figure 2.2 shows the normalised number of binary systems $\mathcal{N}_b$ as a function of the binary period with

$$\mathcal{N}_b(t) = \frac{N_b(t)}{N_b(0)}, \tag{2.2}$$

where $N_b(0)$ denotes the initial and $N_b(t)$ the number of binary systems within the cluster at time t. The dotted line in Fig. 2.2 shows the Gaussian fit to the observations of Raghavan et al. (2010). The thin solid line indicates the initial period distribution of binary systems with solar-mass primaries. For periods larger than 10^7 days, this distribution is not entirely log-uniform, which is caused by the random setup of the binary systems. During the setup, the random distribution of binary systems independent of their semi-major axis results in some cases where the local mean separation is smaller than the semi-major axis. Stars of wide binary systems tend to have a star closer than their binary companion, leading to fewer large-separation binaries than expected. This

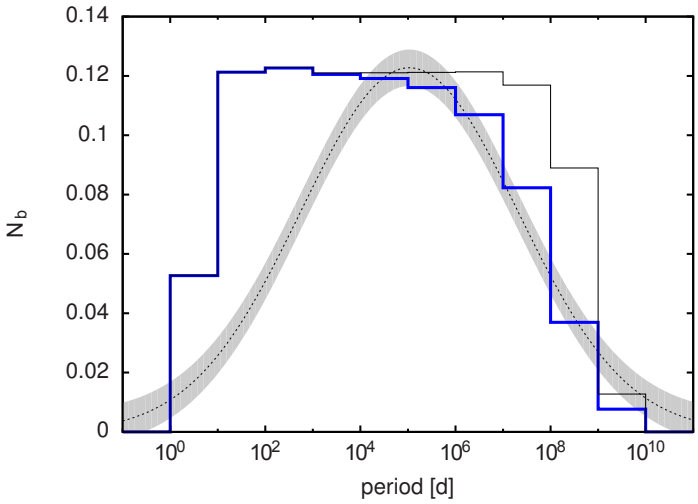

Figure 2.2: Chosen initial period distribution (thin solid line) and period distribution after 1 Myr (blue line) resulting from the NBODY6 simulations by Kaczmarek et al. (2011) compared with a Gaussian fit (dotted line) to the observations by (Raghavan et al., 2010). Due to shortcomings in the simulation setup, the initial distributions is not totally log-uniform (see text for a more detailed explanation). Image taken from Korntreff et al. (2012).

results in both stars being part of no higher order system.

After 3 Myr of dynamical development (blue in Fig. 2.2), the number of binaries with periods longer than $1.1 \cdot 10^5$ days, which roughly corresponds for systems with solar-mass primaries to binaries with separations exceeding 40 AU, is reduced whereas the number of binaries with smaller separations is basically unchanged.

The reason is that these wide binary systems have a lower binding energy than short period binary systems. Thus, wide binary systems can easily be disassociated due to three- and four-body encounters, where a perturber transfers some of its kinetic energy to the system. During this interaction, the binding energy of the binary may even become positive, leading to a destruction of the binary system (Heggie, 1975). In contrast to binaries with periods around 10^8 days, for binary systems with periods around 10^6 days these interactions might only widen the separation between the two stars, making the destruction after repeated encounters more likely.

Kaczmarek (2012) found that the solar-mass binary frequency is reduced by $19 \pm 7\%$ after 3 Myr, due to the destruction of the wide binary systems. However, short periods ($< 10^5$ days) are not affected by the dynamical destruction. Thus other mechanisms have to convert the short period side from a log-uniform to a log-normal period distribution.

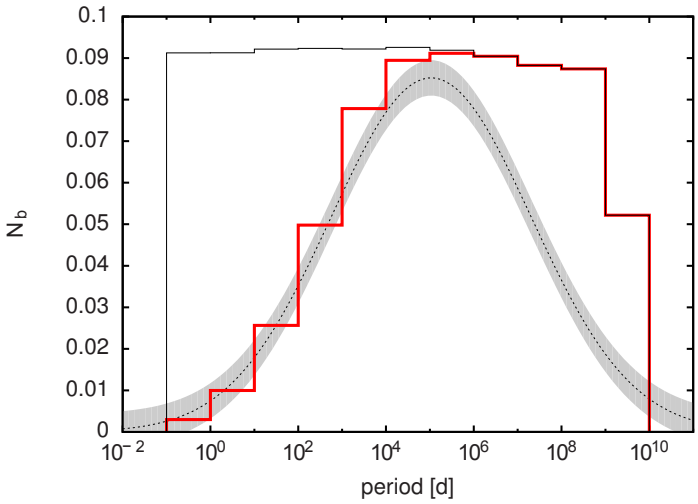

Figure 2.3: Chosen initial period distribution (thin black line) and period distribution after 1 Myr (red line) for binaries embedded in an r^{-2} gas density distribution with $\rho_{max} = 10^5$ cm^{-3} and a sound speed of 0.49 km/s, compared to a Gaussian fit (dotted line) to the observations by (Raghavan et al., 2010). Image taken from Korntreff et al. (2012).

2.3 Gas-induced orbital decay of solar-mass stars

Above simulations neglect the gas in which stars are still embedded during the first Myr. I investigated the effect of this gas on the binary population, namely the orbital decay induced by the interaction of the binaries with the surrounding natal gas. More specifically, this interaction leads to the excitation of waves in the surrounding gas, which reduces the angular momentum of the binary. The result is a smaller distance between the two stars.

To include this effect in the above described simulations of ONC-like clusters, the analytic approximation by Stahler (2010) (see Sec. 1.5.2: Eq. 1.19 and 1.20) was applied to a binary population as described in Sec. 2.2 and evaluated for solar-mass stars. This approximation is based on the assumptions, that

(i) the wave generation itself is neglected (far-field approximation),

(ii) the binary orbit is circular,

(iii) the gas is uniformly distributed, and

(iv) the orbital velocity of the stars in the binary system is higher than the sound speed of the gas.

This approach extends the work of my diploma thesis, where only the overall effect onto the binary population independent of their primary mass was investigated.

For gas-induced decay, the gas density distribution in the cluster is of vital importance. Gas densities of up to $10^7 \mathrm{cm}^{-3}$ were observed in star forming infrared dark clouds (Padmanabhan, 2001) and around high-mass protostars Indriolo et al. (2013) observed densities $> 5 \cdot 10^9$ cm^{-3}. The different mean densities in these observations result from the different dimensions. Since infrared dark clouds ($\approx$ 2pc) contain several clumps which might form stars and an in-between zone with much lower density. Therefore, the mean density of this observation has to be much smaller than the gas density surrounding high-mass protostars ($\approx$ 0.1pc).

Additionally, the density of the gas depends also on the position of the star inside the cluster. The densest regions are assumed to be at the cluster centre, but the there formed massive stars might remove the gas very quickly. This leads to a shorter embedded time span, but within a high density gas. In contrast, the density at the cluster outskirts is assumed to be lower, but caused by the lack of massive stars it might be removed last, resulting in a longer interaction time of a low density gas and the binary system. Since it is not known how exactly the density of the star forming gas relates to the mass of the formed binary system and its position inside the cluster, an isothermal gas density which follows the stellar density distribution was assumed. To prevent the distribution from diverging at the centre, the density is kept constant at a value ρ_{max} inside the cluster core radius $R_{\mathrm{core}} = 0.2$ pc. Outside this region, the density decreases isothermally. Thus, the gas density distribution can be described by the equation

$$\rho_{\mathrm{gas}}(r) = \rho_{\mathrm{max}} \begin{cases} 1, & r < R_{\mathrm{core}} \\ (R_{\mathrm{core}}/r)^2, & R_{\mathrm{core}} < r < R_{\mathrm{cluster}}. \end{cases} \tag{2.3}$$

Using this gas density distribution, core densities ρ_{max} in the range from $10^3 - 10^9 \mathrm{cm}^{-3}$ were investigated. A core density of $\rho_{\mathrm{max}} = 10^5 \mathrm{cm}^{-3}$ fits best, when comparing the resulting final period distribution of solar-mass binary systems to observations. For the core density of an isothermal density distribution a sound speed of $c_s = \sqrt{2\pi G \rho_{\mathrm{max}} r_{\mathrm{core}}^2} = 0.49$ km s^{-1} can be approximated (e.g. Binney & Tremaine, 1987, Eq. 4.123). This might underestimate the sound speed, since velocity dispersions of up to 2.5 km s^{-1} have been observed in infrared dark clouds (Sridharan et al., 2005), which are commonly used to represent the sound speed (Huff & Stahler, 2007).

The orbital decay was investigated for 1 Myr, since then the gas is expelled (Leisawitz et al., 1989) and the binary - gas interaction stops. It was found that the overall effect of the gas-induced orbital decay on the binary population in the cluster is to reshape the period distribution by pushing binaries to tighter orbits leading also to mergers.

Figure 2.3 shows the initial period distribution of binaries with solar-mass primaries as thin solid line and the final period distribution as red line. Since the orbital decay is more rapid for tighter binaries (see. Eq. 1.20), close binary systems are the first to be altered. As time proceeds,

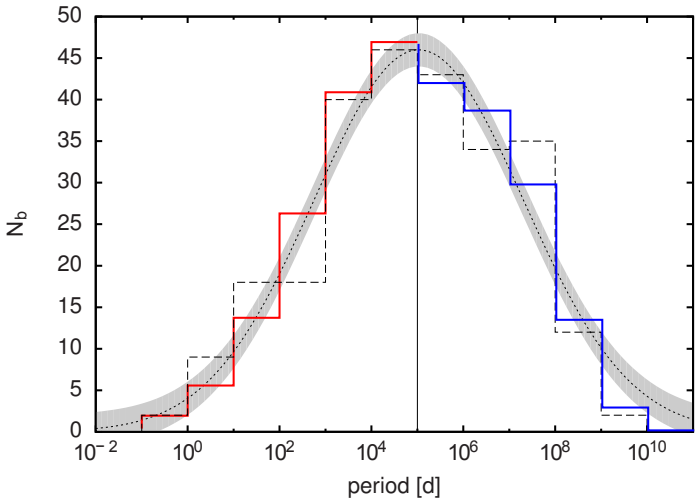

Figure 2.4: Comparison of the period distributions resulting from the orbital decay of embedded binaries (red line for $< 10^5$ days) and the dynamical destruction (blue line for $> 10^5$ days), with the observations of Raghavan et al. (2010) (dashed line). Additionally, the log-normal fit by Raghavan et al. (2010) is shown as dotted line. Image taken from Korntreff et al. (2012).

binaries with even larger orbits are affected until the orbital decay process stops when the gas is expelled from the cluster. In extreme cases orbital decay can even lead to the merging of a binary. The process of orbital decay reduces the number of short period binaries. Within 1 Myr, 12% of all solar-mass binary systems have merged and for periods shorter than $5.5 \cdot 10^4$ days a shift towards even shorter periods occurs.

2.4 Combination of orbital decay and cluster influences

In contrast to the orbital decay, the stellar interactions in the cluster continue after the gas expulsion and therefore are simulated for 3 Myr. Overall, the orbital decay only influences periods shorter than $P_{\mathrm{orb}} = 5.5 \cdot 10^4$ days, whereas dynamical interactions influence periods longer than $P_{\mathrm{dyn}} = 1.1 \cdot 10^5$ days. Thus, the period range $5.5 \cdot 10^4 - 1.1 \cdot 10^5$ days is neither effected (less than 3% change in comparison to the initial conditions) by orbital decay nor dynamical destruction. Additionally, it was found that only in $\ll 1\%$ of all cases binaries that exchange partners and become more strongly bound (binary hardening) transfer to the regime where orbital decay takes place. This means that both processes can be combined in an additive way, to get an idea of the evolution of an entire binary population in a cluster.

In a next step the combined simulation results are compared to the observations of Raghavan et al. (2010). The combined effect of both processes on the period distribution is shown in Fig. 2.4,

for the same mass range as the observation, namely 0.5 $M_\odot \leq m_1 \leq 1.5\ M_\odot$. The dashed line shows the observations of Raghavan et al. (2010) and their log-normal fit is shown as dotted line. The simulated distribution (solid line) matches the observed distribution in six of eleven period bins well with a maximum error of 2%. For four bins, the maximum error is 10 % and one bin has an error of ≈ 20 %. Overall, the simulated distribution matches the log-normal distribution fitted to the observations.

Thus, as a result of these two processes, the log-uniform period distribution of binaries born in dense, embedded clusters is transformed to the log-normal period distribution found for older systems in the field. As long as the cluster is embedded in its natal gas (about 1 Myr), the orbital decay of the embedded binaries depopulates the left-hand side of the period distribution. This process ends with the expulsion of the gas. At the same time the dynamical evolution of the cluster destroys wide binaries, depopulating the right-hand side of the period distribution. This process can in principle still take place when the gas has left the cluster, but will do so less as gas expulsion causes cluster expansion and decreasing cluster density (Pfalzner & Kaczmarek, 2013). The combined effect of these processes is that the final period distribution of the binary population in the star cluster has become log-normal, although it was initially log-uniform.

2.5 Gas-induced orbital decay for other stellar masses

Although the period distribution of solar-mass stars in the field is reproduced very well with this approach, it has to be analysed how the period distribution is processed for other stellar masses. In this section only the gas-induced orbital decay is investigated. Therefore, only binaries with periods $\leq 10^5$ days are shown in the following, since binaries with periods $> 10^5$ days are mostly influenced by dynamical destruction (see Sec. 2.2).

The cluster model described in Sec. 2.1 was used and the resulting period distribution calculated via the gas-induced orbital decay Eq. 1.19 was evaluated for binary systems with

- M-dwarf primaries: $0.1\ M_\odot < m_1 < 0.5\ M_\odot$,
- B-star primaries: $1.5\ M_\odot < m_1 < 5.0\ M_\odot$, and
- O-star primaries: $16\ M_\odot < m_1$.

Finally, the resulting period distribution of each mass-range was compared to observations of main-sequence binary populations.

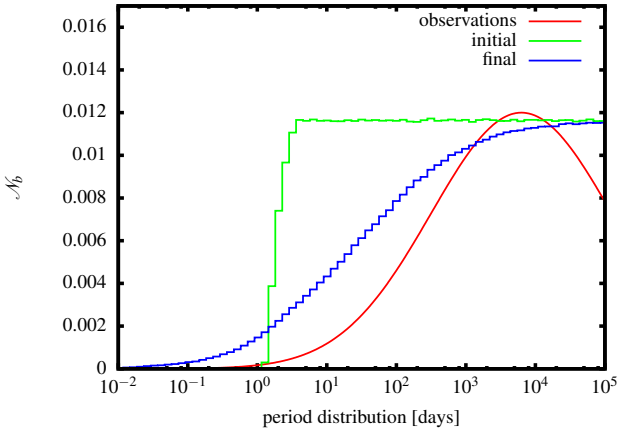

Figure 2.5: Observed field period distribution (red line) by Fischer & Marcy (1992) and effect of the orbital decay (blue line) on a initially log-uniform distribution (green line) for the primary mass range $0.1\ \mathrm{M}_\odot < m_1 < 0.5\ \mathrm{M}_\odot$.

2.5.1 Binary systems with M-dwarf primaries

First the period distribution of binary systems with a primary mass range of $0.1\ \mathrm{M}_\odot < m_1 < 0.5\ \mathrm{M}_\odot$ is evaluated. The initially log-uniform period distribution (green line, Fig. 2.5) is processed by the orbital decay for 1 Myr resulting in a similar period distribution (blue line, Fig. 2.5) as calculated for solar-mass primaries. The red line indicates a fit to the data of Fischer & Marcy (1992), who observed binary systems with M-dwarf primaries within the vicinity of 20 pc. Since here only the short period side is shown, it is not possible to normalise these distributions.

Even though the period distribution resulting from the simulations (blue line) shows a similar trend as the observations (red line), in most of the short period bins more binary systems exist than were observed. This results in a different slope which does not reproduce the observed peak. There are a variety of possible explanations for this discrepancy. First, the observations show a huge error (see Fig. 1.4b), which results especially in an unreliable slope. Thus, the overabundance of short period binaries from the simulations could still fit the data if the slope of the observation fit was flatter. Second, by applying the analytic formula by Stahler (2010) to a whole binary population, all approximations made in his derivation are included. The detailed limitations and approximations which follow from this will be discussed in Sec. 2.6. Additionally, the initial gas properties were chosen to match the observations of solar-mass binaries best, neglecting that the surrounding gas density might depend on the star which is formed. For this no scaling law has been established so far, but the observations of a gas density of $10^7\ \mathrm{cm}^{-3}$ in infrared dark clouds (Padmanabhan, 2001) suggests, that the chosen value of $5 \cdot 10^5\ \mathrm{cm}^{-3}$ might be to low for solar-mass stars and even M-dwarfs.

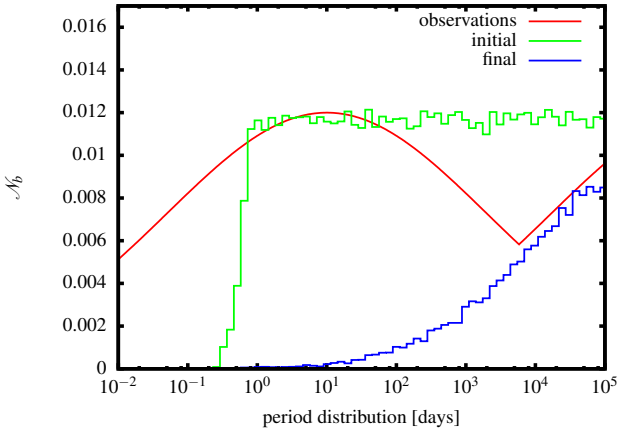

Figure 2.6: As in Fig. 2.5, but for a the primary mass range of 1.5 $M_\odot < m_1 < 5.0\ M_\odot$.

2.5.2 Binary systems with B-star primaries

In the observations of the primary mass ranges 1.5 $M_\odot < m_1 < 5.0\ M_\odot$ a short period peak at ≈ 10 days was found for spectoscopic binaries (Carquillat & Prieur, 2007) and Duchêne & Kraus (2013) report a long period ($\approx 5 \cdot 10^6$ days) peak for visual binaries. These findings have to be reviewed with caution, since the first follows from the observations of only spectroscopic binary systems (see Fig. 1.4c) and the latter from a private communication, where no data has been published so far. Thus, the simulation data is only compared to the peaks of the observations and not the slopes of the fitted curve (see red line in Fig. 2.6) due to their high uncertainty. Therefore, the apparent reproduction of the slope for periods $\geq 5 \cdot 10^3$ days is not relevant. Further observations of this mass range are necessary to compare the observed period distributions to theoretical investigations. Additionally, the observed peak for short periods cannot be reproduced by the calculations (blue line), since most of these binaries already merged. In contrast to the mass range $0.1\ M_\odot < m_1 < 0.5\ M_\odot$, one would expect a higher gas density around these binaries, than around solar-mass stars. Since this would lead to an even higher merger rate, the analytic approach might overestimate the orbital decay for binaries with primary masses $> 1.5\ M_\odot$.

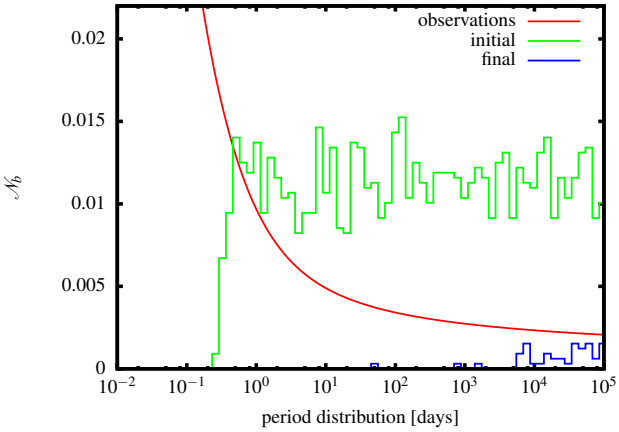

Figure 2.7: As in Fig. 2.5, but for a primary mass of $m_1 > 16\ \mathrm{M}_\odot$.

2.5.3 Binary systems with O-star primaries

For binary systems with $m_1 > 16\ \mathrm{M}_\odot$ (Fig. 2.7) nearly all short period binaries merge in the calculation (blue line) and the observed period distribution (red line) cannot be reproduced. Here, the largest homogeneous sample to date was observed by Sana et al. (2013), who studied 360 O-type stars (see Fig. 1.4d). Their distribution favours short period binary systems. This strongly contradicts the analytic approximation, since there binary systems with small periods and high masses are affected first by the gas-induced orbital decay. Thus, the dependency of the orbital decay approximation on the initial semi-major axis $\propto 1/a_0$ and system mass $\propto M_{sys}^2$ (see Eq. 1.20) should be questioned in further investigations.

Furthermore, the environment of high-mass stars is difficult to constrain, since their formation process is still not entirely clear (see Sec 1.3.1). From observations it is known that binary systems with primaries $m_1 > 16\ \mathrm{M}_\odot$ are preferentially formed in very massive star clusters. The radiation pressure of high-mass stars removes the gas faster than low-mass stars, resulting in these binaries being exposed shorter (< 1 Myr) to the effect of orbital decay than in sparse clusters or the outskirts of dense clusters. However, the surrounding gas might be even denser ($\geq 5 \cdot 10^9$ Indriolo et al., 2013) for this short time span, increasing the effect of orbital decay. Thus, it cannot be said if these two effects result in a larger or smaller semi-major axis reduction for this mass range. Additionally, high-mass stars evolve faster than low-mass stars and only a few high-mass binary systems with circumbinary discs were observed so far (e.g. Sánchez-Monge et al., 2013). Therefore, it remains unknown if the lack of discs is due to the fast evolution of massive binary systems or due to their high radiation pressure, which might lead to a fast destruction of a disc and expulsion of other circumbinary gas.

2.6 Limitations and approximations

To associate these results with the context of binary evolution, the limitations and approximations for using the analytic approach itself have to be taken into account. In above described model, using Stahlers far-field approximation for the orbital decay required to assume all binaries to be on circular orbits and to neglect the wave generation process within the gas. This is a gross over-simplification as most binaries are on eccentric orbits with ≈ 96 % having eccentricities > 0.2 (see Sec. 1.4). On the other hand, the consequences of the wave generation mechanism is unknown. The here used approximation of Stahler (2010) converts the stellar masses into density perturbations, which induce the outgoing acoustic wave. This is an idealisation and might overestimate the effect of orbital decay or result in false dependencies on the binary and gas properties. Binary systems with a circumbinary disc are observed to have a region of lower density surrounding the binary, which extends to approximately two semi-major axis (see Sec. 1.5.3). Thus, the coupling mechanism between binary system and gas has to be represented by a gravitational binary potential which acts at a distance larger than the semi-major axis onto the surrounding gas.

Also the cluster setup limits the calculation to only one cluster case. This neglects that the low-mass field population results from different cluster types. The field population is clearly a mixture of binaries originating from different star formation environments. They might have formed in isolation, sparse (e.g. Taurus), dense (e.g. ONC), or very dense (e.g. Arches) clusters. This means that the here calculated results need to be combined with the results from other cluster types to give a complete picture of the field binary period distribution. Associations such as the Taurus clusters probably never had a gas density above $10^4 \mathrm{cm}^{-3}$ and the current stellar density is below 10 stars pc^{-3} (Luhman et al., 2009). This low mean gas density suggests that the resulting density surrounding the binary system is lower in such a sparse system than in the centre of a massive cluster. This would lead to less binaries which merge and thus lead to an even higher difference between the observations and calculations.

On the basis of actual observations, one can only speculate how many stars are born in these different density regions. While Bressert et al. (2010) stated that the minority of all stars in the solar neighbourhood formed in high density regions, it is unclear whether this is also true for all of the galaxy. Dukes & Krumholz (2012) concluded that 1/2 - 2/3 of all stars are formed in clusters consisting of more than 1000 stars. As such massive clusters initially had much higher stellar densities (Pfalzner, 2009), which indicates that environmental effects are important for these clusters.

In addition to the ONC-like model clusters studied here, further investigations should include a variety of initial conditions: different stellar and gas density distributions (Kroupa, 1995b; Parker et al., 2011), a range of cluster densities (Olczak et al., 2010; Marks et al., 2011), and different virial states of the cluster (Allison 2009).

For the initial conditions of the binary system, the property distributions of sparse associations were used. Therefore, to verify the initial conditions, observations of very young (< 0.1 Myr) binary populations have to be performed. This would exclude that other processes have already altered the population, but these observations hold other difficulties. Any conclusions about such a young binary distribution would be biased due to small number statistics. In this evolutionary stage, most stars are deeply embedded in gas resulting in high extinction. Thus, only ten to hundred stars are usually observable, even for clusters with a few thousand stars. The effect, that not all stars are formed at the same time adds to the observational bias.

The initial conditions of the surrounding gas are also idealised. To match the observed solar-mass distribution a isothermal density distribution with a density of 10^5 cm^{-3} at the cluster centre is used. This is a good approximation for the mean gas density of a cluster, but it neglects that stars form in a filamentary structure. As a consequence, the gas surrounding a binary system is probably much denser. Especially for high-mass protostars surrounding gas densities $> 5 \cdot 10^9$ cm^{-3} were observed (Indriolo et al., 2013).

Additionally, the here investigated gas-induced orbital decay might not be the only mechanism processing the short period range. For example, through accretion events the binary system could also gain angular momentum (Shi et al., 2012), leading to a slower orbital decay. In the here performed calculations, accretion of gas onto the binary components has been neglected, since this is vital for Stahler's far-field approximation.

Summarising, further theoretical investigations are necessary to test if the calculated binary population development differs if one reduces the approximations. The two strongest approximations are the use of only circular orbits and to neglect the wave generation. In the next chapter a self-consistent hydrodynamic simulation is developed, including the wave generation and allowing to treat binaries on eccentric orbits. With such a simulation, the effect of a direct wave generation is investigated and the parameter range is extended to eccentric orbits.

Before understanding the simulated orbital decay of a whole cluster population, it is important to understand the effect of the newly introduced mechanisms. Thus, in the following chapter, the simulation only covers the evolution of one single binary system. To investigate the evolution of such a gas-embedded binary system in different environments, a parameter study is carried out to cover probable binary and gas properties.

3 Numerical simulation

Here the self-consistent hydrodynamic code developed to study the feedback of the gas onto an embedded binary systems is described. Section 3.1 identifies the physical properties necessary to describe the evolution of the binary system and its gas environment and specifies the differences to the analytic approximation. The mathematical descriptions, which can be used to calculate the physical properties of the here used setup are introduced in Sec. 3.2. Since the equations describing the physical properties need to be solved numerically, they are discretised and the used numerical methods are presented in Sec. 3.3. A set of physical test problems were studied in Sec. 3.4 and the convergence and accuracy of the numerical calculations were determined.

3.1 Physical processes

As mentioned in Sec. 1.5, the interaction of binary stars with the surrounding gas includes many different physical processes. Here the early evolution, where the binary system has just formed, is investigated. The environment of such a binary system depends on the formation mechanism (see Sec. 1.3). In the case of disc fragmentation or disc-assisted capture, the binary system ends up embedded in a circumbinary disc, which has been observed for a variety of systems masses (see Sec. 1.5.3). For high-mass stars no simulations have been performed so far, but for solar-mass stars simulations (Artymowicz & Lubow, 1994; de Val-Borro et al., 2011; Fateeva et al., 2011) show three distinct zones of interaction for systems with circumbinary discs: (i) the accretion discs around the individual stars, (ii) the circumbinary disc and envelop surrounding the entire binary system, and (iii) an in-between zone (see Fig. 1.11). The latter describes the region where the density drops by several orders of magnitude producing a 'gap'. To reduce the effects which need to be considered in the simulation, only the circumbinary gas was included and the processes of the circumstellar accretion discs were neglected.

In contrast to the circumstellar disc in the disc fragmentation or disc-assisted capture case, the binary system might be fully embedded in gas when it forms via core fragmentation. Due to the surrounding gas from all sides, the observational information is sparse. One would expect that the gas properties surrounding a binary formed via core fragmentation is quite similar to the ones for binaries formed via disc fragmentation or disc-assisted capture. However, simulations suggest, that the gas could be even closer to the binary system (Machida et al., 2008) if the former

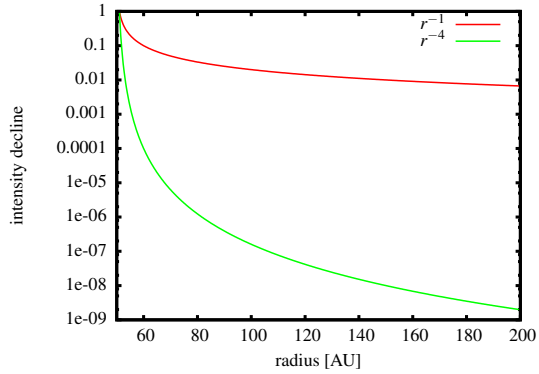

Figure 3.1: Intensity decline with radius for a density (r^{-1} - red) and a quadrupole moment (r^{-4} - green)

formation scenario took place. In their simulations the newly formed binary system is surrounded by a density of $\approx 10^{10}$ cm^{-3}.

The here simulated binaries are surrounded by a spherical symmetric gas cloud. This surrounding gas starts at the inner radius r_{in}, which corresponds to the outer edge of the low-density zone. Within the low-density zone, only the binary system itself is simulated. This means, that the low-density gas in this zone and the circumstellar accretion discs are neglected. Simulations with different inner radii were performed covering the observed and simulated binary-gas distances for all three formation scenarios.

This is the mayor difference between the analytic approximation by Stahler (see Sec. 1.5.2) and the here developed numerical simulation, since the wave generation itself was neglected in the approximation. In the here developed simulations, the outgoing wave in the circumbinary gas is generated at the inner radius.

Stahler's analytic approach converts the quadrupole moment of each star into a density perturbation, since all static terms (and thus the monopole moment) are neglected. This perturbation induces the acoustic wave, which travels outwards. For a circular, equal mass binary system with a semi-major axis of 100 AU, the acoustic wave start at 50 AU from the centre of mass (origin of the system), which is the directly at the orbit of the binary system. In a 3D sphere this density decreases with r^{-1} (red line in Fig. 3.1). In the numerical simulation, the quadrupole moment of the binary system generates a wave at the inner radius of $r_{in} = 2a = 200$AU. Thus the intensity of the force which acts onto the gas declines with r^{-4} (green line in Fig. 3.1) and is then converted into a density perturbation.

This two curves in Fig. 3.1 cannot be compared directly, since the red line shows a declining density perturbation, whereas the green line shows a declining force. Therefor, it needs to be taken into account how the force acts at the inner radius on the surrounding gas and the resulting

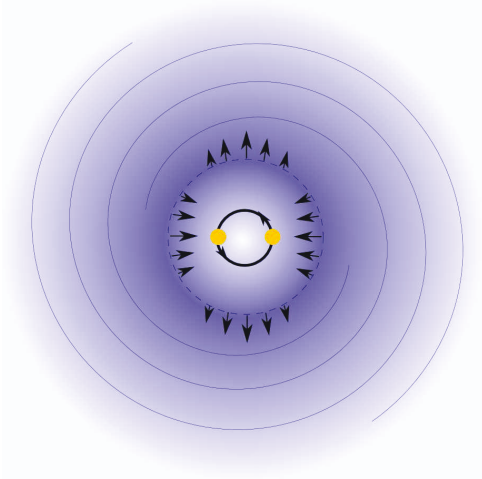

Figure 3.2: Schematic picture of the effect of the binary system onto the surrounding gas. The arrows represent the quadrupole moment of the oscillating gravitational potential of the rotating binary system and the spiral arms are the outgoing acoustic waves.

amplitude needs to be compared to the amplitude of the analytic approximation at this inner radius. Thus the results are expected to show major differences, depending on the inner radius and the efficiency of wave generation, but is presumably lower than the approximation by Stahler. These effects will be investigated in Sec. 4.2. The outer radius of the surrounding gas is chosen to be lower than the Jeans radius (= radius of a gas cloud which contains the Jeans mass), since otherwise the gravitation of the gas would be dominant (see Sec. 1.3.1).

Typically, gas expulsion in young clusters occurs at a cluster age of 1-3 Myr. Since this can be assumed to be the time where most young stellar systems are still embedded in their natal gas (Leisawitz et al., 1989), here the binary development over the first Myr was studied. This is a good timescale for the embedded phase, because not every star is born at the same time and those first born stars are likely to be located at the centre of a cluster where the most massive stars are preferentially born and thus the gas starts vanishing first.

A schematic picture of the simulated process is given by Fig. 3.2, which shows a binary system embedded in its circumbinary gas. The two stars (yellow circles) orbit each other. The quadrupole moment of the oscillating gravitational potential of the binary system, here represented by arrows, is the part of the potential responsible for the here investigated effect. This potential produces outgoing acoustic waves, which are depicted as two outgoing spiral density wave fronts. With them, angular momentum is transferred from the binary system to the gas and transported outward. As a result of this angular momentum loss the binary looses kinetic energy, which in turn leads to a smaller distance between the two stars.

The binary system is defined through its semi-major axis, eccentricity, mass-ratio and system mass. The effect of orbital decay depends on the properties of the binary itself but as well on those of the gas. The relevant gas properties are its density, sound-speed and the inner radius r_{in} where the surrounding gas starts.

3.2 Mathematical description

Mathematically this situation can be described in the following way: The gas is modelled using the Navier-Stokes equation for an isothermal, compressible fluid without viscosity (e.g. Eq. 1.7 Thompson, 2006) - also called Euler equation:

$$\rho\left(\frac{\partial \underline{v}}{\partial t}+\underline{v}\cdot\nabla\underline{v}\right)=-\nabla p+\underline{f} \tag{3.1}$$

and the continuity equation

$$\frac{\partial \rho}{\partial t}+\nabla\cdot(\rho\underline{v})=0, \tag{3.2}$$

with the density ρ, velocity $\underline{v}$ and pressure p of the gas and the external force $\underline{f}=-\nabla\Phi$. Here, $\Phi=\Phi_{binary}$ is the potential of the binary system. If one neglects self-gravity and uses the definition of the sound speed $c_s=\frac{\partial p}{\partial \rho}$, the pressure can be calculated via the density as,

$$\nabla p=(\nabla p)\cdot\frac{\partial \rho}{\partial \rho}=\frac{\partial p}{\partial \rho}\nabla(\rho)=c_s^2\nabla\rho.$$

Modelling the binary system as two point masses, the potential of the binary is given as,

$$\Phi_{binary}=\Phi_1+\Phi_2=-G\left(\frac{m_1}{r_1}+\frac{m_2}{r_2}\right),$$

where $\Phi_{1,2}$, $m_{1,2}$ and $r_{1,2}$ are the potential, mass and distance from the origin to star 1 and star 2 of the binary system, respectively.

The equation of motion for the binary system includes the force of the gas onto the binary system. For star 1 it is given by

$$\underline{a_1}=\frac{Gm_1\underline{r}_{1-2}}{|\underline{r}_{1-2}|^3}-\int dV\frac{G\rho\underline{r}_{1-gas}}{|\underline{r}_{1-gas}|^3}. \tag{3.3}$$

where $\underline{r}_{1-2}$ is the distance vector between the two stars and $\underline{r}_{1-gas}$ the vector between star 1 and the gas volume element.

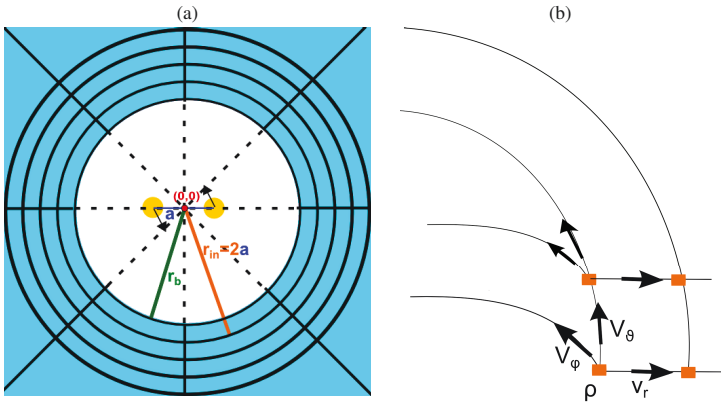

Figure 3.3: (a) Only the circumbinary gas is simulated with the boundary conditions at r_b and the innermost gas cell at $r_{in} = 2a$.
(b) Staggered grid. The density ρ is evaluated at the grid points (orange) and the velocities are evaluated between two grid points.

3.3 Numerical implementation

Here finite differences (Larsson & Thomee, 2003) are used to find a numerical solution of Eq. 3.1. The simulation is performed in spherical coordinates (r,ϕ,θ) and the area of the gas is restricted to $(r,\phi,\theta) \in ([r_{in},r_{out}],[0,2\pi],[0,\pi])$. The innermost gas cell is located at an inner radius of r_{in} from the centre of mass of the binary, since only the circumbinary gas is investigated (see Fig. 3.3a). This corresponds to the outer edge of the gap observed in circumbinary discs of solar-type stars (see Sec. 3.1).

In order to discretise the area where the gas is simulated, a staggered grid was used, meaning that the density ρ is evaluated at the grid points and the velocity $\underline{v}$ between two grid points (see Fig. 3.3b). Using a staggered grid reduces the distances for the derivation calculation effectively. To calculate for example the first derivation of the velocity at the grid point of the density, the distance between the necessary velocities is reduced from two to only one cell.

Our boundary condition for the innermost grid point assures, that no mass is transported inward or outward. With r_{in} being the inner radius of the first gas cell inside the simulation area and $r_b = r_{in} - dr$ is the radius of the inner gas boundary (see Fig. 3.3a), the density and velocity at r_b are set to

$$\rho(r_b) = \rho(r_{in}), \qquad v_\phi(r_b) = v_\phi(r_{in}) * r_b/r_{in},$$
$$v_r(r_b) = v_r(r_{in}), \qquad v_\theta(r_b) = v_\theta(r_{in}) * r_b/r_{in},$$

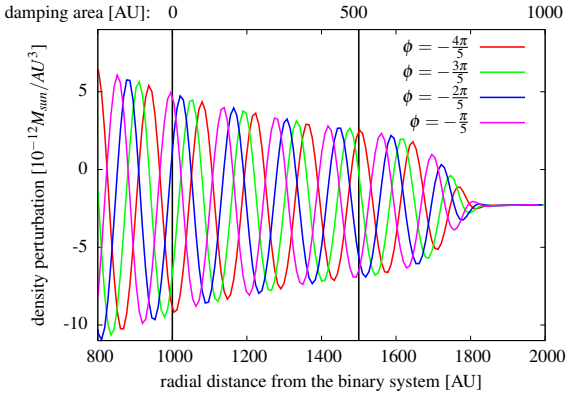

Figure 3.4: Radial cut through the gas cloud surrounding the binary system for different ϕ-directions. A damping zone at the outer boundary $r > r_{start\ damping}$ reduces the radial velocity and thus the amplitude of the waves.

where $\underline{v} = (v_r, v_\phi, v_\theta)$ is the velocity in spherical coordinates.

Since the origin $r = 0$ corresponds to the binary's centre of mass, and the gas always starts outside the gap with $r_{in} > 0$, the singularity at $r = 0$ is excluded from all simulations. In ϕ- and θ- direction periodic boundary conditions were implemented. An additional advantage of the staggered grid is, that only the velocity in θ-direction has to be known at the poles $\theta = 0$ and $\theta = \pi$. Here for every radius r the mean value of all values at $\theta = d\theta$ and $\theta = \pi - d\theta$ was calculated: $v_\theta(r, \phi, \theta = 0) = \sum_\phi v_\theta(r, \phi, \theta = d\theta)$

A damping zone surrounds the simulation area at the outer boundary to mimic open boundary conditions and thus avoid reflections. This was implemented by reducing the velocity in r-direction slowly in the damping zone

$$v_r(r_i) = v_r(r_i) - v_r(r_i) \cdot \left(1 + \tanh\left(10 \frac{r_i + dr - r_{\text{start damping}}}{r_{out} - r_{\text{start damping}}} - 8\right)\right)/2.$$

Figure 3.4 shows the resulting smooth damping zone with $r_{\text{start damping}} = 1001\ AU$ for 4 ϕ-angles in the orbital plane. Within the first 500 AU of the damping area (r=1000 - 1500 AU) no damping is visible to the eye. This very slow first damping phase prevents reflections of the acoustic waves, which enter this region. Within the next 500 AU the damping increases until finally the amplitude is zero.

The relative motion between the binary star and the gas and all accretion processes were neglected and only the circumbinary gas was simulated. To realise this, the initial conditions of the gas were set to $\underline{v}(t = 0, \underline{r}) = 0$ and $\rho(t = 0, \underline{r}) = \rho_0$. For the binary system the initial conditions were calculated at its periastron using $r_p = a(1 - e)$ and $v_p = \sqrt{\frac{G \cdot M_{sys}}{a \cdot |1 - e^2|}}$. In a first relaxation phase of the simulation the calculated binary potential is increased slowly to avoid shocks in the gas

medium. This shocks would be artificial, since they were caused by the abrupt appearance of a binary system in a otherwise quiescent gas. Only after the correct binary potential is reached, the effect of the gas mass onto the binary is calculated (second term of Eq. 3.3) to simulate the angular momentum loss and the resulting change of their orbit.

The static terms of the binary system would lead to gravitational attraction of the gas onto the stars, leading to the accretion of gas. Usually this mechanism is counteracted by the rotation of the surrounding gas. Since the initial velocity is set zero, also the static terms (Φ^{static}) of the potential up to the quadrupole order were subtracted, to counterbalance the initial density and velocity settings. Additionally, the gas inside the gap, which is the main resource of these accretion mechanisms, is neglected a priori. The subtraction of the static term was also used in the approximation by Stahler. There the gravitational potential is expressed as a sum over multipoles (see Eq. 4.2 Jackson 1962 for the electrostatic expansion)

$$\Phi(x) = -4\pi G \sum_{l=0}^{\infty} \sum_{m=0}^{l} \frac{q_{lm}}{2l+1} \frac{Y_{lm}(\theta,\phi)}{r^{l+1}}$$
$$q_{lm} = \int Y^*_{lm}(\theta',\phi')(r')^l \rho(\underline{x}) d^3x'.$$

Y_{lm} are the spherical harmonics, with the primed coordinates referring to the source points and the unprimed coordinates to the points in the field. Static means that the terms have to be independent of the source coordinate ϕ', since the binary ϕ'-coordinate varies with time and the variation of r' with time can be neglected. This is the case for all terms with m=0. Since the term for $l = 1$ is zero, only the terms for $l = 0$ and $l = 2$ have to be subtracted from $\Phi_{binary} = \Phi_1 + \Phi_2 - \Phi_{static}$ resulting in

$$\Phi_{static} = -\frac{G(M_{\rm sys})}{r} + \frac{G(r_1^2 m_1 + r_2^2 m_2)}{4r^3} \cdot 3(\cos(\theta)^2 - 1).$$

Given computational limitations, special considerations have to be made in the numerical setup, to implement these physical effects correctly :

- An artificial numerical viscosity was added into the numerical solution to improve the stability and accuracy of the numerical method.
- The stellar radii are only used to compare them to the semi-major axis in order to test for possible merging. Here it is assumed that the two stars merge if the semi-major axis is lower than the sum of their radii. This is a simplification, since effects like Roche-lobe overflow are neglected (see Sec. 1.5).
- As the binary system shrinks, the gas boundary moves inward. To accommodate this situation new grid points are added to the inner gas boundary. This is done if the distance

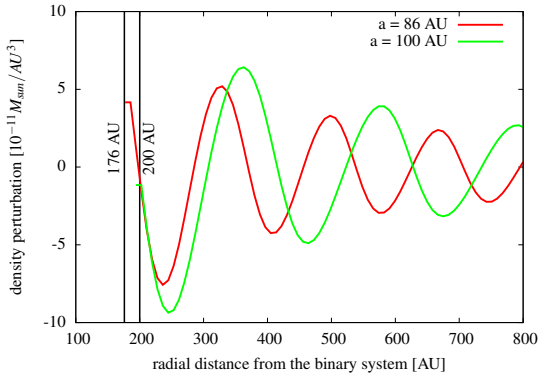

Figure 3.5: Radial cut through the gas showing the density perturbation for a binary system with semi-major axis of 100 AU (green). At a later time-step, the separation of the binary system is reduced to 86 AU, due to orbital decay, and the radial distance from the cluster centre is reduced too (red).

between the centre of mass and the first grid point exceeds the inner radius $r_{in} = x * a$ with a being the semi-major axis of the star and x the selected constant for the inner radius (see Tab. 4.1). Figure 3.5 shows a radial cut through the gas for two different time-steps. Initially the binary system has a semi-major axis of 100 AU and thus the innermost gas cell starts at 200 AU (green). During the simulation, the semi-major axis shrinks continuously to 86 AU due to orbital decay. As the gas also moves further inwards, now the innermost gas cell starts at 172 AU (red). The decay of the semi-major axis means that the period of the binary system becomes shorter, too. As a result, the binary system induces an acoustic wave with a shorter wavelength (red) than initially (green). Normally one would expect the amplitude of the red wave to be higher than the green one, but here the evolution of the semi-major axis has to be considered. In Sec. 4.2 it will be shown, that the lower amplitude of the shorter wavelength results from the shorter interaction time with the binary system, since the orbital velocity increases for a decreasing semi-major axis.

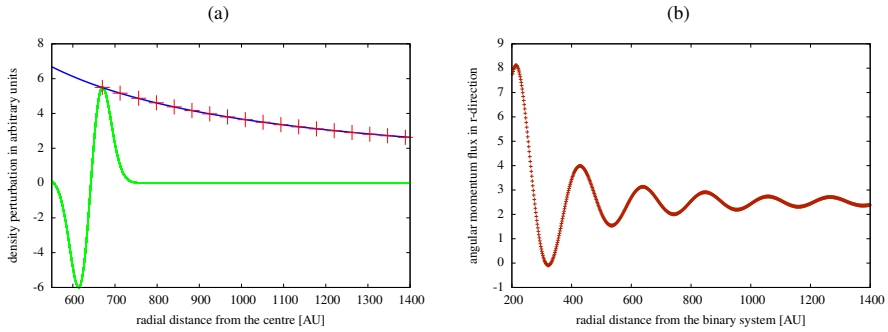

Figure 3.6: (a) Radial cut through the gas is shown. An artificial perturbation travels through the gas - green line for perturbation at $t = 0$. For $t > 0$ only the maximum (red crosses) is shown and fitted with r^{-1} (blue).
(b) Angular momentum transport in r-direction as a function of the radial distance from the binary system.

3.4 Tests of the numerical scheme

A series of tests are performed to investigate if the numerical implementation represents the physical setup correctly. First the implementation of the Navier-Stokes equation, the amplitude decay and the angular momentum transport, and then determine the convergence and accuracy of the numerical code is tested.

3.4.1 Physical conditions

A density perturbation in an idealised gas should travel with the **speed of sound** c_s. In the here presented simulation the sound speed is given and thus measuring the distance which a sound wave travels in a certain time provides a basic test, if the equations were implemented correctly. For this test, an artificial perturbation which travels from the inner gas radius to the beginning of the damping zone was simulated. For different points in time, the distance covered by the perturbation was measured and the sound speed calculated. Comparing this measured value c_s^m to the input value $c_s^i = 0.4$ AU/yr leads to $c_s^m - c_s^i = \pm\ 10^{-12}$, which means that the sound speed is well preserved.

Due to energy conservation, in a spherical volume the **amplitude** of the density should decline with r^{-1}. In a spherical wave of radius r, the energy of the wave front is spread out over the spherical surface area $4\pi r^2$. Therefore, the energy per unit area of an expanding spherical wave decreases as r^{-2}. Since energy is proportional to amplitude squared, an inverse square law for energy translates to a decay law for the amplitude $A \propto r^{-1}$. Figure 3.6a shows such a radial cut through such a spherical wave (green at t=0). The measured decay of the wave maximum with

time is marked with red crosses and an r^{-1} fit (blue) agrees well with this decay, with a deviation error of only 0.01%.

In the process of orbital decay, **angular momentum** is transported outwards. The angular momentum transported in r-direction (Γ) can be calculated starting from the total angular momentum L. With ρ being density, p the pressure, v the velocity of the gas, and (r,ϕ,θ) the spherical coordinates, the angular momentum vector is given by

$$\underline{L} = \vec{r} \times \vec{p} = r \begin{pmatrix} 0 \\ p_\theta \\ p_\phi \end{pmatrix}. \tag{3.4}$$

Due to the geometry of the binary system, only the z-component of the angular momentum is non-zero

$$\underline{r} \times \underline{p}|_z = \cos(\theta)[\underline{r} \times \underline{p}]|_r - \sin(\theta)[\underline{r} \times \underline{p}]|_\theta = -\sin(\theta) r p_\phi .$$

From this the angular momentum flux $\underline{j}$ can be calculated

$$div\,\underline{j} = -\sin(\theta) r \partial_t p_\phi = \sin(\theta) r (div[\rho(\underline{v} \times \underline{v}) + c_s^2 * \rho \underline{\underline{1}}])_\phi ,$$

because

$$\partial_t p_\phi = \partial_t(\rho \underline{v}) = -\nabla[\rho(\underline{v} \times \underline{v}) + c_s^2 * \rho \underline{\underline{1}}].$$

This leads to the angular momentum flux in r-direction

$$\begin{aligned} j|_r &= \sin(\theta) r [\rho(\underline{v} \times \underline{v}) + c_s^2 * \rho \underline{\underline{1}}]_{r\phi} \\ &= \sin(\theta) r \rho v_\phi v_r \end{aligned}$$

and finally the angular momentum transported in r-direction

$$\Gamma = \sum_{\phi,\theta} r^2 \sin(\theta) d\phi d\theta \, j_r \tag{3.5}$$

$$= \sum_{\phi,\theta} r^3 \sin^2(\theta) d\phi d\theta \rho v_\phi v_r . \tag{3.6}$$

Figure 3.6b shows this angular momentum transport in r-direction for every grid-point. Apart from a periodic fluctuation, there is a net outward transport of angular momentum, as predicted by the far-field approximation. The fluctuation results from a small fluctuation in v_r, which gets amplified in the calculation.

Grid	LA1	LA2	LA3	standard simulation	HA1	HA2
dr [AU]	2.8	2.8	4.2	2.8	1.9	1.4
dϕ [π]	0.2	0.33	0.2	0.2	0.1	0.067
dθ [π]	0.2	0.2	0.2	0.2	0.1	0.067
dt(t=0) [days]	664	578	578	578	269	143

Table 3.1: Grid parameters for the standard simulations and simulations with higher and lower accuracy.

3.4.2 Accuracy

The gas and stellar motion is integrated using the Cash-Karp integration method. This is a 4$^{\text{th}}$ order Runge-Kutter integrator with a adaptive time step criterion (Cash & Karp, 1990). Thus, each step the time step dt is adjusted depending on the error between the 4$^{\text{th}}$ order and 5$^{\text{th}}$ order Runge-Kutter calculation for this time step.

Since two stars are rotating and producing two waves, the resulting wavelength of the density perturbation in the gas, which surrounds the binary system, is given by $\lambda_{gas} = c_s \cdot T_{binary}/2$ with T_{binary} being the binary period. The radial grid points of the gas were chosen to have 75 grid points per induced wave at the beginning of the simulation. Thus for the standard wave-length of 200 AU the wave is still represented with 7.5 grid points even if the wavelength is reduced to 20 AU. Due to the symmetry of the problem for circular orbits only a few grid points in $\theta-$ and $\phi-$ direction are required, leading to $d\phi = d\theta = \pi/5$. The first time step is chosen with a Courant-Friedrichs-Lewy (CFL) Number of cfl $= 0.5$. The CFL-condition is a necessary condition for the stability of finite difference schemes (Courant et al., 1928). For an explicit scheme as used here the CFL-condition is fulfilled for $1 >$ cfl $= v^{max} + c_s \cdot dt/dx$. Using this equation the appropriate time step can be calculated. Adding terms for the numerical viscosity, this equation translates for spherical coordinates into

$$dt = \text{cfl}\left(\frac{v_r^{max}+c_s}{dr} + \frac{v_\phi^{max}+c_s}{r\sin(\theta)d\phi} + \frac{v_\theta^{max}+c_s}{rd\theta} + \frac{\mu}{dr^2} + \frac{\mu}{(r*d\theta)^2} + \frac{\mu}{(r\sin(\theta)d\phi)^2}\right). \quad (3.7)$$

During the simulation, it is checked if the time step adjusted by the Cash-Karp method still fulfils this criterion.

To determine whether the choice of parameters is reasonable, the convergence of the simulation is tested by performing simulations with lower (LA1-3) and higher (HA1-2) accuracy than in the standard simulation. Table 3.1 shows the step size of each of these simulation for the three spatial directions and the time. Figure 3.7 shows the relative error of the differences between the semi-major axis of the most accurate simulation (HA2) and all other simulations. Although all simulations lead to a reduction in the binary separation, the relative error shows, that in contrast to

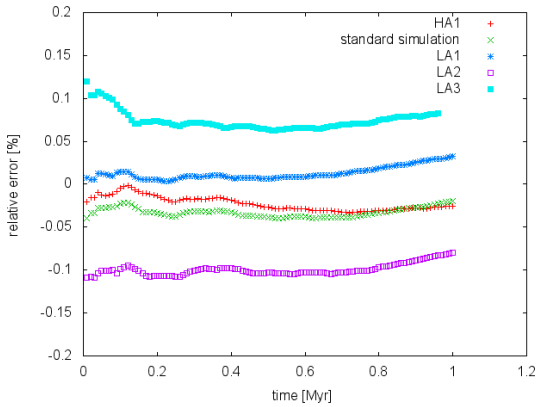

Figure 3.7: Comparison between the standard simulation (green) and a simulation with higher (red) and lower (dark blue, purple, light blue) accuracy (see Tab. 3.1). For all simulations only the relative error of the differences between the simulated semi-major axis of the most accurate simulation (HA2) and their simulated semi-major is shown.

simulations with lower accuracy, the standard simulation deviates only minimal from simulations with higher accuracy. Thus, the code does treat the physical equations accordingly and can be used to calculate the gas density perturbation induced by the binary system and the resulting orbital decay of the binary in the next step.

4 Results of hydrodynamical simulations

In this chapter, the dependency of the orbital decay on the binary and gas properties is investigated. This includes a comparison between the numerical results and the analytic approximation by Stahler (2010). The main difference is that the numerical simulation calculates the wave generation and gravitational interaction between the binary system and the surrounding gas directly (see Sec. 3.1), whereas Stahler's approach uses a far-field approximation (see Sec. 1.5.1).

In Sec. 4.1, a qualitative analysis of the outgoing density wave is presented. It is studied, how the density distribution of these waves in the circumbinary gas depends on the initial binary properties. Here, three different cases are considered: a binary system with circular orbit and equal masses, one with unequal masses, and a binary system with equal masses and an eccentric orbit.

The parameter study of different binary and gas properties is presented in Sec. 4.2. The numerical results are compared to those of the analytic approximation by Stahler (2010). Then the numerical results are approximated by a fit formula covering all gas and binary parameters studied in this investigation (Sec. 4.3). Furthermore, the accuracy of this fit is determined.

The analytic approach can only treat circular orbits. In contrast, the numerical simulations make it possible to investigate eccentric orbits as well. The dependency on the degree of eccentricity is analysed in Sec. 4.4.

4.1 Basics of the density perturbation

The initial parameters of the binary system and the surrounding gas determine the evolution of the binary system orbit. First, the shape of the outgoing density waves is considered qualitatively in three exemplary cases. It is investigated how the binary properties influence the resulting density perturbation of the circumbinary gas. This is important, since the resulting density perturbation determines the orbital evolution of the binary system.

Figure 4.1 shows the simplest case - that of an equal-mass binary on a circular orbit. Three different perspectives within a non-rotating reference frame are shown. On the left hand side, the plot indicates the orbit of the two binary stars in yellow and red. The actual positions of the stars are marked with crosses. This plot shows only the inner simulation area, where the gas is not treated explicitly (see Sec 3.3). Zooming out, a 2D cut $(r, \phi, \theta = 90^\circ)$ through the surrounding 3-dimensional gas sphere in the plane of the binary orbit is visible in the middle panel. Here the

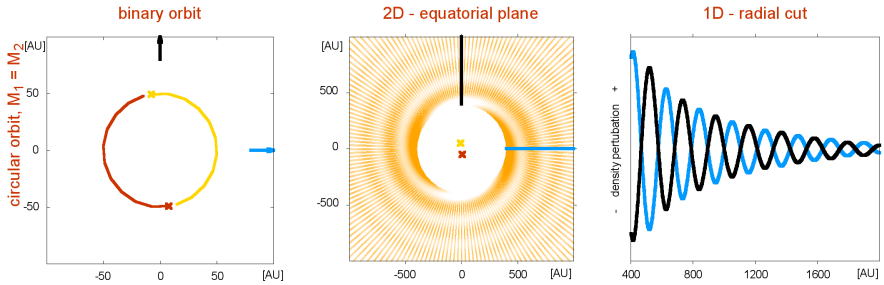

Figure 4.1: Simulation results for a circular binary system with equal masses. The left hand panel shows the orbit of the two binary stars. This is the region where the gas is neglected. In the middle panel the density perturbation of surrounding gas lying in the orbital plane is visible. Cuts through this plane are shown in the right hand panel. The black and blue lines in the first two plots indicate this cuts at $\phi = 0^\circ$ (black line) and $\phi = 90^\circ$ (blue line),

density perturbation is shown in colours from white to orange. White is equivalent to the lowest gas densities, and thus a negative density perturbation amplitude, and orange is equivalent to the highest gas densities, and thus a positive density perturbation amplitude. In the circular orbit, equal mass case, the gravitational potential of the two stars produces an outgoing spiral wave with two symmetric arms. With these outgoing waves, angular momentum is transferred from the binary system to the gas. This angular momentum loss ultimately leads to a shrinkage of the binary orbit. The symmetry of the problem is also visible in the 1D plot of the density perturbation. On the right hand side of Fig. 4.1 a 1D cut through the gas lying in the orbital plane is presented. This plot shows the density perturbation at $\phi = 0^\circ$ (black line) and $\phi = 90^\circ$ (blue line). The position of these cuts is also indicated in the two other plots by black and blue lines, respectively. The envelope of the amplitude decays with its distance from the centre of mass as r^{-1}, which is due to energy conservation in a 3D sphere. Figure 4.2 and 4.3 show three similar plots, but for different binary examples.

In Fig. 4.2 the case of unequal-masses is illustrated for the example of a mass-ratio of $q = 0.5$. Here the mass-ratio $q = m_2/m_1$ is defined in such a way that the more massive star has the mass m_1 and the less massive star the mass m_2. In a non-rotating reference frame, the orbital motion of an unequal mass binaries involves an outer and an inner star (left hand panel). The more massive star's orbit (red) is always inside that of the less massive star (yellow). This means that the less massive star is located closer to the surrounding gas. For binaries with unequal masses only one outgoing wave is visible in the middle panel of Fig. 4.2. The reason is, that the perturbation of the less massive star dominates the surrounding gas.

The inner star is more massive than the outer one, but also has a larger distance to the surrounding gas. In the here shown example the circumbinary gas starts at an inner radius of $r_{in} = 200$ AU and the binary system has a semi-major axis of $a = 100$ AU. As the system mass is $M_{sys} = 1\ M_\odot$

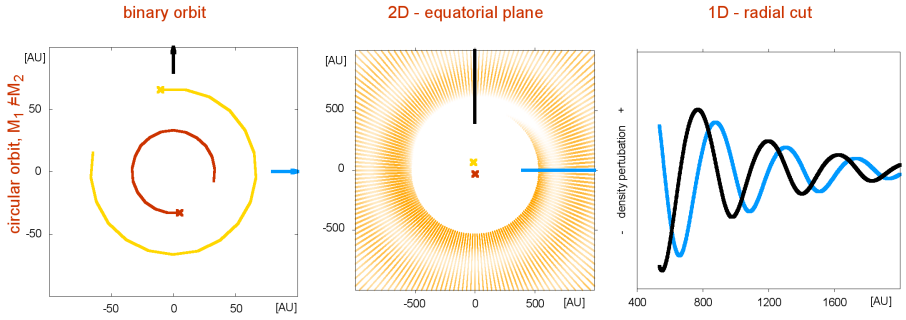

Figure 4.2: Same as Fig. 4.1. but for a binary system with a mass-ratio of q=0.5, with the outer star (yellow) being the less massive one.

and the mass-ratio $q = 0.5$, the inner star has a mass of $m_1 = 0.66\ \mathrm{M}_\odot$ and an orbital radius of $r_1 = 33$ AU and the outer star has the properties $m_2 = 0.33\ \mathrm{M}_\odot$ and $r_2 = 66$ AU. Since the static terms of the gravitation potential are subtracted (see Sec. 3.3), only the quadrupole terms of the potential remain, which are proportional to $m_{1/2}/(r_{in} - r_{1/2})^3$. This leads to a gravitational force acting on the gas with $F_{1/2} \propto m_{1/2}/(r_{in} - r_{1/2})^4$. The ratio of the resulting gravitational forces at the inner radius is $F_1/F_2 \approx 0.83$. The gravitational force of the outer, less massive star is stronger than the gravitational force of the inner, more massive star. So it is the less massive star that produces the dominant spiral wave. But in fact the spiral wave seen in Fig. 4.2 is a superposition of two equal frequency waves with a phase shift, the second wave being the much smaller contribution of the more massive star. It manifests itself in the spiral wave being much broader than the waves for equal mass binaries (Fig. 4.1). Having only one visible spiral arm results in the 1D density perturbation waves at $\phi = 0°$ and $\phi = 90°$ being shifted by exactly 90°. This is the case for all unequal mass where the less massive star becomes more dominant.

The mass-ratios, where the less massive star is more dominant than the more massive can be calculated via the quadrupole moment of the gravitational force. For an inner radius of $r_{in} = 2a$ and the stellar positions being defined by $r_{1/2} = m_{2/1}/M_{sys} \cdot a$, this leads to:

$$1 > \frac{F_1}{F_2} = \frac{m_1}{m_2}\left(\frac{r_{in} - r_2}{r_{in} - r_1}\right)^4 = \frac{m_1}{m_2}\left(\frac{2m_2 + m_1}{2m_1 + m_2}\right)^4 = \frac{1}{q}\left(\frac{2q+1}{2+q}\right)^4. \tag{4.1}$$

This equation is valid for $1 > q > 0.1$. This means the density perturbation of the less massive star is dominant for all unequal mass binaries with $q > 0.1$. For $q \leq 0.1$ the mass of the less massive star is so low, that both stars have an equally but very low influence on the surrounding gas.

The next case investigated here is that of an equal mass binary on an eccentric orbit. As seen in the unequal mass case, the distance to the gas is crucial for the resulting density perturbation.

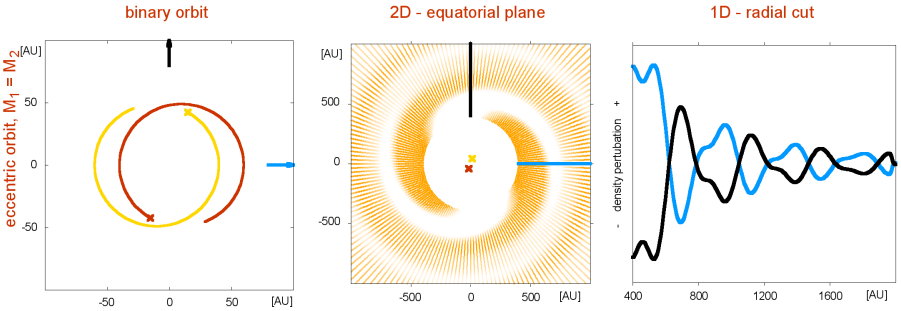

Figure 4.3: Same as Fig. 4.1. but for a binary system with an eccentricity of 0.2.

The eccentric case is even more complex than the case of an unequal mass binary, because the distance between each star and the gas changes throughout the orbit. At the apastron the star has the highest gravitational influence (F_a) on the gas, whereas the influence is lowest at the periastron (F_p) resulting in a ratio only depending on the eccentricity

$$\frac{F_p}{F_a} = \frac{m_1}{m_1}\left(\frac{r_{in}-r_p}{r_{in}-r_a}\right)^4 = \frac{2a-a\cdot(1-e)}{2a-a\cdot(1+e)} = \frac{1+e}{1-e}. \tag{4.2}$$

For an eccentricity of $e = 0.2$, the apastron influence is 1.5 times the periastron influence and for $e = 0.8$ the aproastron influence is even 9 times the periastron influence.

The left panel in Fig. 4.3 shows the orbit of an equal mass binary system with an eccentricity of $e = 0.2$ and a system mass of $M_{sys} = 1\ \mathrm{M}_\odot$. For eccentric orbits, two spiral wave arms are induced (middle panel). The maximum of the density perturbation varies within each spiral arm. This variation results from having double and single peaks throughout one wave (right panel). The single peak results from the apastron passage of each star, where the influence of the other star is lowest. A double peak is produced when both binaries have a nearly equal influence on the gas and pass the same point of the gas shortly after each other. These double peaks result in a much broader spiral arm than observed in the circular case.

For the three cases discussed here, a video is available under http://tinyurl.com/embedded-binary. It shows how the stars produce a density perturbation into an initially uniform gas, finally resulting in the density waves shown as snapshots above.

In this section only three specific examples were presented. However, the general picture remains the same, if other binary and gas parameters are changed. The difference is the amplitude and width of the density perturbation and consequently the impact on the orbital decay. These dependencies are presented in the following.

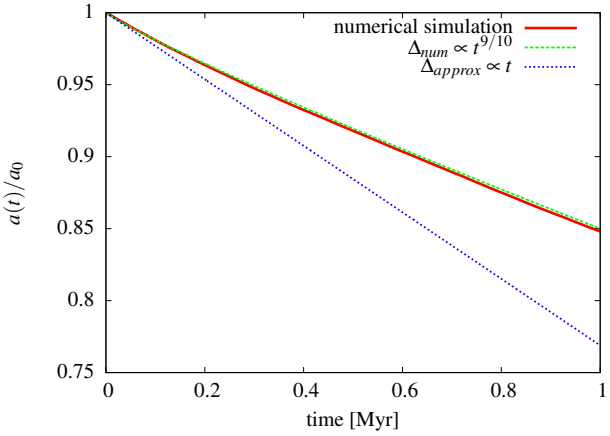

Figure 4.4: Decrease of the semi-major axis with time for the analytic approximation (blue line with $\rho = 5 \cdot 10^5 \mathrm{cm}^{-3}$) and numerical simulation (red line with $\rho = 10^9 \mathrm{cm}^{-3}$). The green line indicates a fit to the simulation data.

4.2 Evolution of binaries with circular orbits

In this section the results of the numerical simulations are compared to the analytic approximation of Stahler (2010). His approach is only applicable to circular orbits, therefore this case is investigated first. Stahler obtains a linear time depend semi-major axis $a_{approx}(t)$ (see Eq. 1.19 and 1.20), where the change Δ_{approx} depends on the initial binary and gas properties.

$$a_{approx}(t) = a_0(1 - \Delta_{approx}) \tag{4.3}$$
$$\Delta_{approx} = \frac{32\pi}{15} \frac{q}{(1+q)^2} \frac{\rho_0}{c_s^5} \frac{G^3 M_{\mathrm{sys}}^2}{a_0} t.$$

In the simulations the binary evolution was followed over a time span of 1 Myr as this is the typical duration of the gas-embedded phase in the most massive clusters in the solar neighbourhood (Sec. 1.3.3). Figure 4.4 shows the relative change of the semi-major axis as a function of time $(a(t)/a_0)$ for a circular binary system. The simulations can be fitted with $\Delta_{num} \propto t^{9/10}$ (green line), with $a_{num}(t) = a_0(1 - \Delta_{num})$. Like the analytic approximation, the time dependency of the numerical simulations (red line) is nearly linear.

As shown later, the orbital decay is slower for shorter semi-major axis. Therefore, the decrease of the semi-major axis during the simulation also causes the orbital decay to slow down. This results in the time dependency of the orbital decay being only nearly linear in contrast to the linear dependency in the analytic approximation.

	variation range	default parameters
binary parameters		
mass-ratio q $[m_1/m_2]$	[0.01:1]	$q^d =$ 1
system mass $M_{\rm sys}$ [$M_\odot$]	[0.5:20]	$M^d_{\rm sys} =$ 1
initial semi-major axis a_0 [AU]	[20:150]	$a^d_0 =$ 100
eccentricity e	[0:1)	$e^d =$ 0
gas parameters		
embedded time t [Myr]	[0:1]	$t^d =$ 1
initial gas number density ρ_0 [cm^{-3}]	$[10^7 : 10^{10}]$	$\rho^d_0 =$ 10^9
gas sound speed c_s [km/s]	[0.2:2.5]	$c^d_s =$ 2
inner radius r_{in} [semi-major axis]	[1.5:4.5]	$r^d_{in} =$ 2

Table 4.1: Binary and gas parameters.

The net orbital decay for circular orbits is considerably lower in the simulations than the analytic approach predicts. This is caused by the generally higher amplitude of the density perturbation at the inner radius r_{in} in Stahler's approximation (for a detailed discussion see Sec. 3.1). In contrast, the amplitude of the density perturbation in the numerical simulations depends on the efficiency of the wave generation, which will be discussed in the following. Thus, to put the approximation and the numerical case side by side, one can for example reduce the gas density for the approximation from 10^9 cm^{-3} to $5 \cdot 10^5$ cm^{-3} (blue line in Fig. 4.4).

To evaluate the influences of the different initial binary and gas properties only one of the properties will be varied at a time and all other properties kept fixed at the value given in Tab. 4.1 as default parameters. The standard system is a circular equal mass ($q = 1$) binary system of $M_{sys} = 1$ M$_\odot$ with a semi-major axis of $a = 100$ AU embedded for 1 Myr in a gas sphere which starts at two semi-major axis (from the centre of mass of the binary system) with a density of $\rho = 10^9$ cm^{-3} and a sound speed of $c_s = 2$ km/s.

Binary properties

First it is investigated how the orbital decay depends on the binary properties themselves, starting with the mass-ratio of the binary system. As discussed above, the mass-ratio between the two stars constituting the binary determines the type of outgoing wave (Fig. 4.2). According to the definition of the mass-ratio $q = m_2/m_1$ with $m_2 \leq m_1$ used here, the maximum of the mass-ratio lies at $q = 1$ corresponding to the equal mass case. This case is used as a standard scenario, but the range of $q \in [0.01 : 1]$ is covered in the parameter study as well. For a binary system with a system

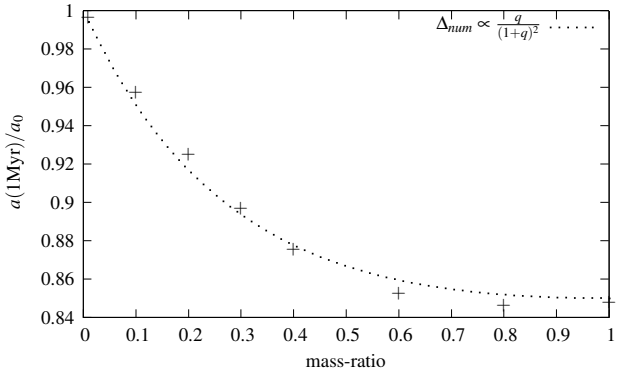

Figure 4.5: Relative semi-major axis after 1 Myr for different mass-ratios. The crosses depict the simulation results and the dotted lines show a fit to these results.

mass of $M_{\mathrm{sys}} = 1\ \mathrm{M}_\odot$, a mass-ratio of $q = 0.01$ corresponds to a primary mass of $m_2 = 0.99\ \mathrm{M}_\odot$ and a secondary mass of $m_2 = 0.01\ \mathrm{M}_\odot$. The secondary mass is even below the hydrogen burning limit at $0.08\ \mathrm{M}_\odot$. On the other hand, for a system mass of $M_{\mathrm{sys}} = 100\ \mathrm{M}_\odot$, such a mass-ratio leads to $m_1 = 99\ \mathrm{M}_\odot$ and $m_2 = 1\ \mathrm{M}_\odot$. The most massive stars observed have a mass of $\approx 150\ \mathrm{M}_\odot$ (Sec. 1.3.1) and it is shown later, that such massive stars do not need to be considered here since for them the effect of orbital decay is very small < 3 % after an embedded time of 1 Myr.

Figure 4.5 shows the simulation results for binary systems with different mass-ratios (crosses). They can be fitted with $\Delta_{num} \propto q/(1+q)^2$ (dotted line). This is the same dependency as predicted by the analytic approximation. The orbital decay is caused by the quadrupole moment of the binary system's gravitational force. For an unequal mass system, only one spiral arm is visible, which can also nicely be seen in the 2D-plane of Fig. 4.2. There the star closest to the surrounding gas becomes dominant, resulting in only one visible spiral arm, which is less efficient in angular momentum transport than two spiral arms. This leads to a semi-major axis reduction of 15 % for $q = 0.8$, whereas the semi-major axis of a binary system with a mass-ratio of q = 0.1 decreases only by 5 %.

The efficiency of the angular momentum transport for the binary to the surrounding gas depends on how efficient the density wave is generated. As we will see, this efficiency is defined by the ratio of the orbital velocity $v_{\mathrm{orbit}} = \sqrt{G \cdot M_{\mathrm{sys}}/a}$ to the sound speed c_s: $\mathbb{V} = v_{\mathrm{orbit}}/c_s$.

For this ratio, one can distinguish two regimes: One where the binary velocity is higher than the sound speed ($\mathbb{V} \geq 1$) and one where the binary velocity is lower than the sound speed ($\mathbb{V} < 1$). For the standard parameters investigated here, the orbital velocity as a fraction of the sound speed is

$$\mathbb{V} = \frac{v_{\mathrm{orbit}}}{c_s} = \frac{2.97\ \mathrm{km/s}}{2\ \mathrm{km/s}} \approx 1.5. \tag{4.4}$$

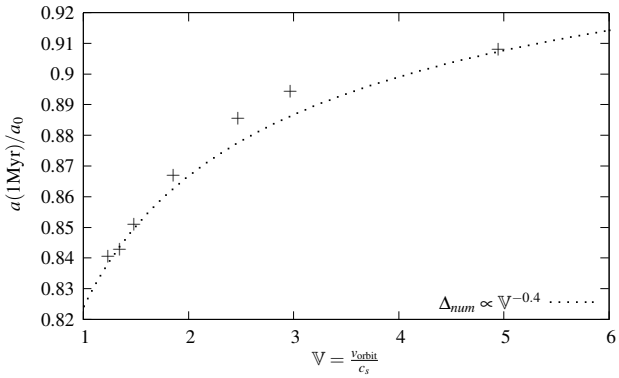

Figure 4.6: Relative semi-major axis after 1 Myr for different fractions of orbital velocity to sound speed. The crosses depict the simulation results and the dotted lines show a fit to these results.

It is important to notice, that v_{orbit} changes as the semi-major axis decreases, here only the initial semi-major axis is used to calculate the orbital velocity. To reach $\mathbb{V} < 1$ by changing the initial binary properties, a larger semi-major axis has to be chosen meaning $a > 220$ AU for $M_{sys} = 1$ M$_\odot$. Alternatively, the system mass can be reduced to $M_{sys} < 0.5$ M$_\odot$ for $a = 100$ AU. For such binary systems, the quadrupole moment $\propto M_{sys}/a^4$ is low and thus the effect of orbital decay.

The considerations above imply an isolated binary system. Including the cluster environment, the possibility of orbital decay for such systems is even smaller, when considering the circumbinary gas. Depending on the cluster density, another star is likely to interact with the circumbinary gas, necessary for the orbital decay. Especially for high semi-major axis, another star is likely to destroy the gas environment, which would stop the orbital decay. Furthermore, for low system masses another star is likely to engage in three-body interactions leading to the ejection of the star with the lowest mass, which possibly hardens the binary system but not through orbital decay. Thus, systems with $\mathbb{V} < 1$ will not be considered at all, since the orbital decay is not the major influence for these binary systems.

For $\mathbb{V} \geq 1$, the simulation results show that the coupling mechanism is most efficient, when the sound speed is similar to the orbital velocity (see Fig. 4.6). The resulting semi-major axis after 1 Myr can be fitted using $\Delta_{num} \propto \mathbb{V}^{-0.4}$.

For the here used default values, a binary system with $\mathbb{V} = 4$ reduces its semi-major axis by 9 % and for an optimal wave generation mechanism ($\mathbb{V} = 1$), the semi-major axis is reduced by 18 %. Thus, the orbital decay differs by 50 %, depending on the efficiency of the angular-momentum transport.

Next, the dependency on the system mass is investigated. The lower limit of the investigated system masses range is 0.5 M$_\odot$, since for $M_{sys} < 0.5$ M$_\odot$ the orbital velocity of the stars in a

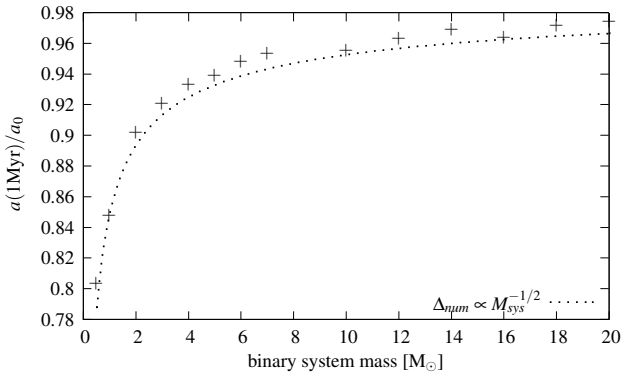

Figure 4.7: Relative semi-major axis after 1 Myr for different system masses. The crosses depict the simulation results and the dotted lines show a fit to these results.

circular binary system is lower than the chosen sound speed, meaning $\mathbb{V} < 1$. The orbital decay is very small < 3 % for a system mass of 20 $M_\odot$, which is chosen as upper limit. This is well below the high-mass case of 100 $M_\odot$ mentioned above.

Varying the binary system mass, the numerical simulations show a dependency of $\Delta_{num} \propto M_{sys}^{-1/2}$ (see Fig. 4.7). This strongly deviates from the analytic approximation, which shows a M_{sys}^2 - dependency. Nevertheless, this approximated system mass dependency seems to be not in accordance with observations (see Sec. 2.5). The reason for this difference is that for the analytic approximation the system mass is directly transformed into the density perturbation. Therefore, the system mass of the approximation is comparable to the amplitude of the gas density perturbation at the inner radius. In contrast, in the numerical simulation the amplitude of the gas perturbation increases sub-linear with linear increase of the system mass. However, increasing the system mass leads to a linear increase in the angular momentum of the binary system. Thus, the sub-linear increasing angular momentum transfer cannot remove the same percentage of angular momentum from a high-mass binary to the gas than in the low-mass case. This reduces the effect of orbital decay for higher system masses.

Additionally, increasing the binary system mass while keeping the semi-major axis constant, means also increasing the orbital velocity of the binary system. As shown above, the fraction $\mathbb{V} = v_{\mathrm{orbit}}/c_s$ determines how efficient the angular momentum is transported from the binary system to the gas. In the here investigated case of $\mathbb{V} \geq 1$, the coupling mechanism is most efficient for $\mathbb{V} = 1$. Therefore, the orbital decay of high-mass stars is much slower than for low-mass stars, since $\mathbb{V}$ increases for increasing system mass.

The semi-major axis also changes the orbital velocity $v_{\mathrm{orbit}} = \sqrt{G \cdot M_{\mathrm{sys}}/a}$. The maximum semi-major axis, where the velocity of the standard binary system is still larger than the sound speed

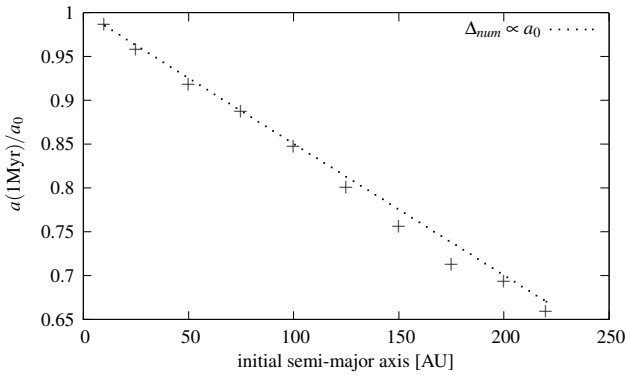

Figure 4.8: Relative semi-major axis after 1 Myr for different initial semi-major axis. The crosses depict the simulation results and the dotted lines show a fit to these results.

of 2 km/s is 220 AU. This is a reasonable upper limit for the semi-major axis investigation, since one of the widest binary system which is still surrounded by a circumbinary disc is BD+31°7643, a main-sequence B5 star with a projected separation of 200 AU (Kalas & Jewitt, 1997). At a semi-major axis of 20 AU, the semi-major axis loss is lower than 5%, using the default values for all other initial binary and gas parameters. Therefore, the semi-major axis of this parameter study was chosen to be in the range of $20-220$ AU, with a default value of 100 AU.

In Stahlers analytic approximation, the change of the semi-major axis (second term Eq. 4.3) depends as $\Delta_{approx} \propto a_0^{-1}$ on the initial semi-major axis. Again, including the effect of wave generation, the simulation results in Fig. 4.8 show in contrast a linear dependency on the initial semi-major axis $\Delta_{num} \propto a_0$. This results directly from the angular momentum transport being less efficient for lower orbital velocities and thus high semi-major axis. The initial semi-major axis has a huge influence on the final semi-major axis, since the resulting orbital decay changes from 30% for $a_0 = 200$ AU to 10% for $a_0 = 50$ AU.

Gas properties

The simulation results are not only influenced by the initial binary parameters, but also depend on the properties of the gas environment (lower part of Tab. 4.1). In an embedded cluster, the gas density depends on the type of cluster (e.g. loose or compact cluster see Sec. 1.3.3) and the location of the binary within the cluster, with the highest gas density located at the centre of the cluster. In addition, the gas mass decreases with time as stars form and the gas becomes expelled due to radiation pressure of high-mass stars and/or supernova explosions. In star forming infrared dark clouds a gas density of 10^7 cm^{-3} is observed (Padmanabhan, 2001). Simulations predict densities of up to 10^{10} cm^{-3} around protostars directly after their formation (Machida & Matsumoto, 2011),

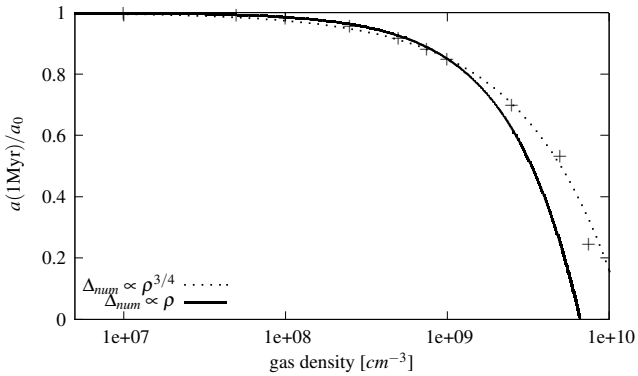

Figure 4.9: Relative semi-major axis after 1 Myr for different densities. The crosses depict the simulation results and the dotted lines show a fit to these results.

which coincides with observations of high-mass star formation sites where Indriolo et al. (2013) observed a density of $> 5 \cdot 10^9 \mathrm{cm}^{-3}$. Taking these values as a guideline here, the simulations were performed with the gas number density ranging from $10^7 \mathrm{cm}^{-3}$ up to $10^{10} \mathrm{cm}^{-3}$.

A higher gas density speeds up the orbital decay in both, the analytic approximation and numerical simulation (see Fig. 4.9). The simulation results confirm the linear dependency on the gas density found in the analytic approximation for densities $\leq 10^9 \mathrm{cm}^{-3}$. However, for densities $> 10^9 \mathrm{cm}^{-3}$, the simulations show $\Delta_{num} \propto \rho^{3/4}$ (see Fig. 4.9). The difference between the linear and non-linear behaviour starts when the semi-major axis is reduced by more than 20%. There, the changes of orbital velocity of the star becomes dominant, reducing the efficiency of the angular momentum transport and thus the final semi-major axis.

Since the observations of the gas density around high-mass protostars and simulation suggests, that the density is mass dependent, this should be included when calculating a the orbital decay of a specific binary system. Unfortunately, so far neither observational nor theoretical work can describe the dependency of the surrounding gas density on the binary system mass.

Another physical property which influences the efficiency of the angular momentum transport is the sound speed of the gas. It depends on the equation of state of the gas, its temperature and composition. A representative model for regions of low-mass star formation would be a low temperature (10 K) H_2 gas that can be treated as ideal gas. In this case the sound speed would be low with $c_s \approx 0.2$ km/s. On the other hand, in high-mass starless cores sound speeds from 1 km/s to 2.5 km/s were observed (Sridharan et al., 2005). Therefore, this parameter study covers the range of $0.2 - 2.5$ km/s,

As seen before, the ratio of orbital velocity to sound speed $\mathbb{V} = v_{binary}/c_s$ plays a crucial role, when determining the efficiency of the coupling between the binary system and the surrounding

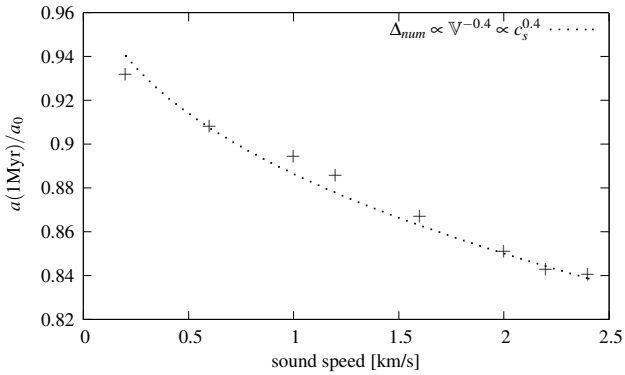

Figure 4.10: Relative semi-major axis after 1 Myr for different sound speeds. The crosses depict the simulation results and the dotted lines show a fit to these results.

gas. For constant initial binary parameters, changing the sound speed is equivalent to changing $\mathbb{V}$. Thus, the numerical results can be fitted using $\Delta_{num} \propto \mathbb{V}^{-0.4} \propto c_s^{0.4}$ (see Fig. 4.10). In contrast, the analytic approximation shows a much stronger dependency with $\Delta_{approx} \propto c_s^5$. The reason is, that for the sound speed the approximation and the numerical case cannot be compared, since the dependency in the numerical simulations is determined by the wave generation, which was neglected in the analytic approximation. Like for the ratio $\mathbb{V}$, the difference in orbital decay between a low and high sound speed can be $\approx 50\%$.

So far, the physical parameters of the gas have been discussed. The geometry of the gas sphere is defined by the inner radius r_{in} where the circumbinary gas starts. At first glance it seems to be just a numerical choice, but it actually represents the extend of the physical area of the low-mass density region surrounding the binary. As seen in Sec. 4.1, the outgoing density waves strongly depend on the distance between the stars of the binary system and the innermost gas cell. Simulations by Shi et al. (2012) of a stage where the gas sphere surrounding the binary system has formed a disc, show an average inner radius of two semi-major axis (see also Sec. 1.5.3). Therefore, two semi-major axis was used as a default parameter. Here, also smaller values of the inner radius (1.5 semi-major axis) were tested and the entire range up to a semi-major axis loss lower than 1% was covered, which corresponds to 4.5 semi-major axis.

Naturally the inner radius does not appear in a far field approximation, since there the wave generation itself is not included. Throughout the simulation the inner radius is fixed at the chosen multiple of the semi-major axis $r_{in} \in [1.5a : 4.5a]$. This is achieved by decreasing the inner radius as the binary orbit decays. The simulation results in Fig. 4.11 can be fitted using $\Delta_{num} \propto r_{in}^{-4}$. This coincides with the force of the binaries quadrupole momentum acting on this inner radius $F \propto r^{-4}$ (see Sec. 4.1), which induces the density waves responsible for the orbital decay. Physically, the

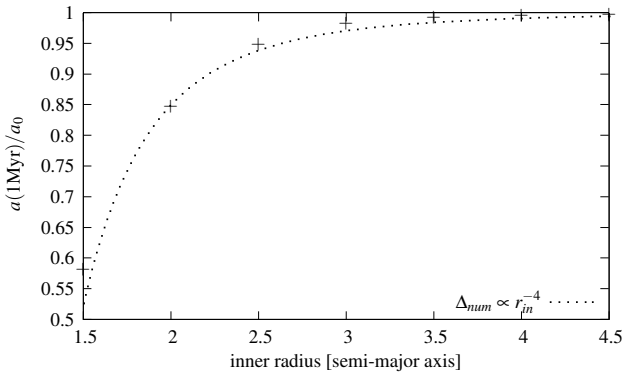

Figure 4.11: Relative semi-major axis after 1 Myr for different inner radii. The crosses depict the simulation results and the dotted lines show a fit to these results.

faster orbital decay for a smaller inner radius represents the increase of the gravitational force for shorter distances between the star and the gas and thus a better coupling mechanism. The inner gas radius is, beside the gas density itself, the property which influences the outcome of the orbital decay most. In the here shown case, the orbital decay varies from only 1% for an inner radius of 4.5 semi-major axis to 50% for 1.5 semi-major axis. Thus it is vital to get a better observational picture of those star forming regions to obtain a realistic parameter range.

4.3 Fit and Latin Hypercube Sampling

In the last section, the dependence of the orbital decay on the initial binary and gas properties was determined. Table 4.2 summarises the change Δ of the semi-major axis for Stahler's approximation $a_{approx} = a_0(1-\Delta_{approx})$ and the fit to the numerical simulations $a_{num} = a_0(1-\Delta_{num})$.

In summary, the dependence of the orbital decay onto the duration of the embedded phase, gas density and binary mass-ratio are similar to the predictions of the analytic approximation. However, the dependence on semi-major axis, system mass, sound speed, and inner radius differ from that in the approximation. This is caused by their influence on the efficiency of the wave generation, which was neglected in the analytic approximation. As pointed out in Sec. 2.5, for the system-mass this was already expected, given that the mass dependency of analytic approximation is not in accordance with the observations.

In Stahler's approximation, the independence of the binary and gas properties is assumed. Observations suggest, that this is actually not the case and several possible dependencies will be discussed later. Nevertheless, to retrieve a fit-formula it is also assume that all variables are inde-

	Δ_{approx} **analytic approach**	Δ_{num} **fit to numerical simulation**
binary parameters		
mass-ratio	$C_2 \cdot \frac{q}{(1+q)^2}$	$C_q = 0.6 \cdot \frac{q}{(1+q)^2}$
system mass	$C_3 \cdot M_{sys}^2$	$C_q \cdot \left(\frac{M_{sys}^d}{M_{sys}}\right)^{1/2}$
semi-major axis	C_4/a_0	$C_q \cdot \frac{a_0}{a_0^d}$
gas parameters		
time	$C_1 \cdot t$	$C_q \cdot \left(\frac{t}{t^d}\right)^{9/10}$
gas density	$C_5 \cdot \rho$	$C_q \cdot \left(\frac{\rho_0}{\rho_0^d}\right)^{3/4}$
gas sound speed	C_6/c_s^5	$C_q \cdot \left(\frac{c_s}{c_s^d}\right)^{0.4}$
inner radius	-	$C_q \left(\frac{r_{in}^d}{r_{in}}\right)^4$

Table 4.2: Change Δ of the semi-major axis for the fit to the numerical simulations $a_{num} = a_0(1-\Delta_{num})$ and the analytic approximation $a_{approx} = a_0(1-\Delta_{approx})$. X^d denotes the default values from Tab. 4.1, all C_is are constants and $C_q = 0.6 \cdot q/(1+q)^2$.

pendent and combine for example the r_{in}-term $(r_{in}^d/r_{in})^5$ with the fit of

$$a(q,t) = a_0 \left(1 - 0.6 \cdot \frac{q}{(1+q)^2} \cdot \left(\frac{t}{t^d}\right)^{9/10}\right),$$

which results in

$$a(q,t,r_{in}) = a_0 \left(1 - 0.6 \cdot \frac{q}{(1+q)^2} \cdot \left(\frac{r_{in}^d}{r_{in}}\right)^5 \cdot \left(\frac{t}{t^d}\right)^{9/10}\right).$$

In the same manner, the terms of ρ_0, c_s, M_{sys}, and a_0 are included, leading to

$$a(t, r_{in}, \rho_0, c_s, a_0, e, q, M_{sys}) = a_0(1-\Delta_{num}) \tag{4.5}$$

$$\Delta_{num} = 0.6 \cdot \frac{q}{(1+q)^2} \left(\frac{c_s}{c_s^d}\right)^{0.4} \left(\frac{r_{in}^d}{r_{in}}\right)^4 \left(\frac{a_0}{a_0^d}\right) \left(\frac{\rho}{\rho^d}\right)^{3/4} \left(\frac{M_{sys}^d}{M_{sys}}\right)^{1/2} \left(\frac{t}{t^d}\right)^{9/10}.$$

As discussed above, this formula is only valid for a binary system with an orbital velocity greater than the sound speed of the gas ($\mathbb{V} \geq 1$).

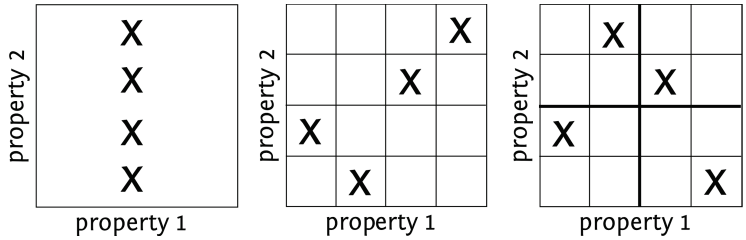

Figure 4.12: Choosing variables from a 2D sample. Left panel: Testing the variability of one parameter / Middle panel: Latin Hypercube sampling / Right panel: Orthogonal Latin Hypercube sampling

In Sec. 4.2 this fit was only tested for the default case with one parameter varied at a time. In a 2D example, this means fixing 'property 1' while changing 'property 2' (see left panel Fig. 4.12). Testing the whole 6-dimensional parameter space is extensive. Thus, a mathematical tool called orthogonal Latin Hypercube Sampling was used to verify the fit (Hoare et al., 2008). With this method a set of parameters can be calculated, which represent this 6-dimensional parameter space and reduces the number of necessary simulations to $N = 2 \cdot (n_{input} + n_{output}) = 14$, since here six input parameters $a_0, M_{\rm sys}, q, \rho, r_{in}$ and c_s and one output parameter $a$are tested. In the middle panel of Fig. 4.12 an example of a Latin Hypercube Sampling to retrieve an optimal coverage of a 2D parameter space is shown. The here used orthogonal Latin Hypercube Sampling ensures additionally, that from every sub-bin of the parameter space, indicated by thick lines in the right panel of Fig. 4.12, one parameter set is chosen.

Here the 'Sampling and sensitivity analyses tools' (SaSAT) of Hoare et al. (2008) was used to calculate an orthogonal Latin Hypercube Sample, which ensures that the ensemble of random numbers is a good representative of the real variability. As an input the ranges for each parameter (see Tab. 4.1) are used to calculate 14 independent parameter sets. These parameter sets were simulated using the hydrodynamic simulations and the resulting semi-major axis was compared to the semi-major axis calculated with the fit formula above. Tab. A.1 in the appendix shows the parameter combinations, simulation results, fit results and the difference between the semi-major axis loss due to orbital decay in the simulations and fit formula. Since these parameters represent an orthogonal Latin Hypercube in 6 dimensions, the resulting differences between the fit formula and simulation can be used to determine an error for the fit formula. The maximum difference between the semi-major axis loss in the simulation and the fit was 3%. This means that an error of 3% can be assumed for the combined fit formula (for the accuracy of the simulation itself see Sec. 3.4).

As mentioned above, some binary and gas properties are not independent from each other, which has been neglected here and also in the analytic approach. The surrounding gas density might depend on two parameters $\rho(M_{sys}, r_{cluster})$:

- The density surrounding a star or stellar system seems to correlate with the mass of this system M_{sys}, since around high-mass protostars a higher gas density as at low-mass star formation sites was observed (Indriolo et al., 2013).

- The mean gas density of a cluster depends on the radius of the cluster $r_{cluster}$. High mass stars, which need a high density, might not form in the outskirts of clusters. In contrast, low-mass stars might as well form in the inner cluster region as in the outskirts and therefore may be surrounded by dense or sparse gas.

Here an ideal gas was assumed, which simplifies the equation of state to $\rho = p/(R_s \cdot T)$, where T is the temperature of the gas, p the pressure and R_s the gas constant. For the parameter study above T and p are set indirectly via gas density and sound speed $c_s^2 = \partial p/\partial \rho$. However, the temperature of the gas also depends on the binary system mass, since the higher the mass of a star the higher its luminosity and thus the heating of the gas environment. Therefore, knowing the system mass and position of a binary system in a cluster could define the gas properties via a chosen equation of state. If such a law were available, this would restrict the parameter study above. In this case, the last free gas parameter would be the inner radius. Observations and simulations which determine this inner radius are only for a few specific binaries available so far and even if a dependency of the inner radius on the mass-ratio, system mass, and eccentricity is suggested, $r_{in}(q, M_{sys}, e)$, no general rule is given so far (see Sec. 1.5.3). Thus, with further observations and theoretical work, the gas parameters could be determined only by the binary and cluster properties.

Additionally, all of these parameters depend on the semi-major axis, which changes throughout the simulation. If the reduction of the semi-major axis is large enough, this change actually dominates the evolution. This was shown for densities $> 10^9$ cm^{-3}, where the density dependence of the orbital decay becomes non-linear resulting from a semi-major axis reduction of $\geq 20\%$.

4.4 Evolution of binaries on eccentric orbits

The analytic approximation is so far limited to binary systems on circular orbits. However, observations show that binaries on eccentric orbits are much more common. The observed eccentricity distribution of $f(e) = 2e$ (see Sec. 1.4) leads to 96% of a typical binary cluster population having eccentricities larger than $e = 0.2$. Therefore, if one wants to know the relevance of the orbital decay in a binary population of a star forming cluster, the extension to eccentric orbits is crucial. Therefore, the temporal development of the orbit for binaries with eccentricities in the range of $e \in [0, 1)$ was simulated.

In Sec. 4.4, it was demonstrated that the orbital decay depends strongly on the inner radius, where the circumbinary gas starts. For eccentric orbits, the distance between the star's position

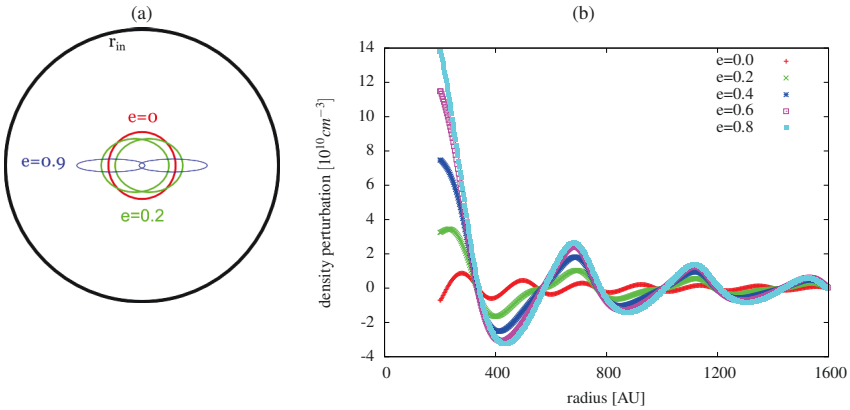

Figure 4.13: (a) Sketch of binary orbits with different eccentricities and their position in reference to the inner gas boundary r_{in}.
(b) Density perturbation resulting from binary systems with orbits of different eccentricities.

and the inner radius varies strongly with time and with it the gravitational force acting on the gas (see Eq. 4.2).

Figure 4.13a shows three different binary orbits and their relation to the inner radius, assuming $r_{in} = 2a$. The minimal distance between the apocentre of the stellar orbits and the inner radius depends on the eccentricity. For the circular case this minimal distance is $1.5a$, whereas for an eccentricity of 0.2 the distance reduces to $1.4a$ and even further to $1.05a$ for an eccentricity of 0.9. Here it is neglected, that the inner radius might also depend on the eccentricity (see Sec. 1.5.3), since no underlying dependency was found so far. Additionally, the radiation pressure of the stars could influence the inner radius, which would have an even higher impact for binary systems with highly eccentric orbits.

The distance between the apastron of the stellar orbit and the inner radius determines the amplitude of the density perturbation $\Delta\rho = \rho(t) - \rho_0$. Figure 4.13b shows the resulting density perturbation within the circumbinary gas for different eccentricities. The maximum amplitude of the density perturbation exceeds the background density $\rho_0 = 10^9 \mathrm{cm}^{-3}$ for all binary systems with $e \geq 0.2$. Following this simulations, these high density perturbations lead to a physically incorrect treatment in the hydrodynamic simulation. Therefore, to investigate high eccentricities, but ensure the validity limit of the simulation code, all simulations are performed with an inner radius larger than the default value of two semi-major axis. A larger inner radius reduces the amplitude of the density perturbation and the resulting semi-major axis change, which is proportional to the inner radius with $\Delta_{num} \propto r_{in}^{-4}$. Thus, with a larger inner radius, the effect of eccentric orbits can be investigated.

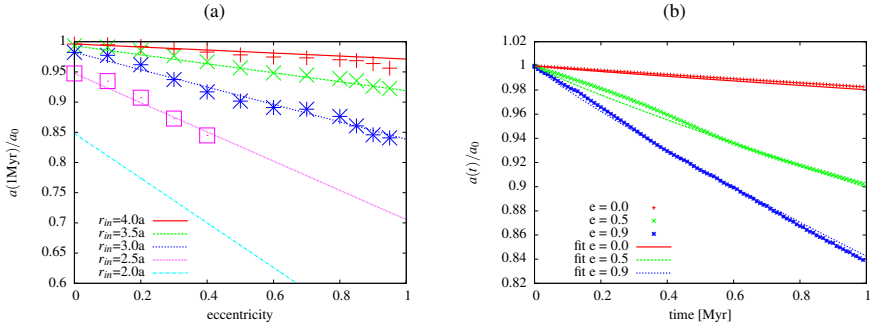

Figure 4.14: (a) Percentage of semi-major axis after 1 Myr as a function of the eccentricity. The colours denote different inner radii from 4 semi-major axis (red) to 2 semi-major axis (light blue). (b) Decrease of the semi-major axis with time for different eccentricities.

For the same semi-major axis, the higher amplitudes of the outgoing waves in binaries with higher eccentricities lead to a stronger orbital decay than circular binaries experience. Figure 4.14a shows the dependency of the orbital decay on the eccentricities for different inner radii. To exclude the case, where the perturbation exceeds the background density, for an inner radius of 2.5 semi-major axis only eccentricities $e \leq 0.4$ were simulated. For larger inner radii the whole eccentricity range was investigated. The dependency of the orbital decay on the eccentricity can be approximated by

$$a(e) = a(e^d = 0, t) \cdot \left(1 - (1.8 \cdot r_{in}^{-1.5} - 0.2) \cdot e \cdot \left(\frac{t}{t^d}\right)^{9/10}\right), \tag{4.6}$$

where $a(e^d = 0, t)$ is the semi-major axis after a simulation time t of a circular binary for which all other binary and gas parameters are the same. Using this formula, a system with an inner radius of two semi-major axis and an eccentricity of $e = 0.7$ would experience an semi-major axis loss of 40% due to orbital decay (light blue line Fig. 4.14a).

Assuming again, that the variables are independent, the combined fit formula for circular binaries (Eq. 4.5) can be inserted as $a(e^d = 0)$ in the fit formula for the eccentricity (Eq. 4.6) leading to

$$a(t, r_{in}, \rho_0, c_s, a_0, e, q, M_{sys}, e) = a_0(1 - \Delta_{num})(1 - \Delta_{num}^{ecc}) \tag{4.7}$$

$$\Delta_{num}^{ecc} = (1.8 \cdot r_{in}^{-1.5} - 0.2) \cdot e \cdot \left(\frac{t}{t^d}\right)^{9/10}$$

$$\Delta_{num} = 0.6 \cdot \frac{q}{(1+q)^2} \left(\frac{c_s}{c_s^d}\right)^{0.4} \left(\frac{r_{in}^d}{r_{in}}\right)^4 \left(\frac{a_0}{a_0^d}\right) \left(\frac{\rho}{\rho^d}\right)^{3/4} \left(\frac{M_{sys}^d}{M_{sys}}\right)^{1/2} \left(\frac{t}{t^d}\right)^{9/10}.$$

Thus, the eccentricity is included as a correction factor. To test this fit, a 7-dimensional orthogonal Latin Hypercube Sampling was performed (see Sec. 4.3), yielding to an error of $\lesssim 6\%$. In Tab. A.2 in the appendix all initial and calculated properties and resulting errors are shown.

Now it is possible to compare the semi-major axis decay with time for different eccentricities. Figure 4.14b shows the simulation results and fits of an orbital decay for $e = 0$, $e = 0.5$ and $e = 0.9$ and an inner radius of $r_{in} = 3a$. The differences between the circular and the eccentric case result from the closer minimum separation between the innermost gas cell and the outermost point of the orbit. Thus, even if a binary system with a circular orbit shows only a 2% orbital decay, the orbit of a binary system with an eccentricity of 0.9 decays by 15%.

4.5 Summary

In this chapter the numerical code developed for this thesis was used to simulate the orbital evolution of a binary system embedded in gas for an extensive parameter space.

- Qualitatively, the changes of the binary parameters are directly visible in the shape of the resulting outgoing density wave in the surrounding gas. There, it can be seen that for a binary system with unequal masses only one spiral arm is visible, because one star dominates the binary - gas interaction. Since, the gravitational force of the density, which acts on the stars, results in the observed orbital decay. Thus, these unequal mass systems with only one visible spiral arm show a slower orbital decay.

- Quantitatively, the effect of this density wave onto the semi-major axis of the binary system was investigated in an extensive parameter study for different gas and binary properties. The results were fitted and compared to the analytic approximation by Stahler (2010). It was shown that the approximation overestimates the effect of orbital decay by neglecting the wave generation process itself. Including the wave generation process in the simulations leads to a slower orbital decay for circular binary systems.

- The efficiency of the wave generation itself depends on the fraction of $\mathbb{V} = v_{\rm orbit}/c_s$, with the orbital velocity of the binary system $v_{\rm orbit} = \sqrt{G \cdot M_{\rm sys}/a}$. Thus, for all properties which are involved in the wave generation, the semi-major axis development shows different dependencies as predicted by the approximation.

- The semi-major axis is changing throughout the simulation. Therefore, a separation from the other properties is not possible. This causes the properties which are not involved in the wave generation (t, q, ρ) to show similar dependencies as the analytic approximation.

- By simulating the wave generation itself, the inner radius r_{in} where the circumbinary gas starts was introduced. The resulting orbital decay depends crucially on this inner radius $\propto r_{in}^{-4}$. Thus, observations of this radius are vital to improve the simulations.
- In contrast to the analytic approximation, the numerical simulations can be extended to eccentric orbits. The investigation of eccentric orbits showed, that the orbital decay is faster for binary systems with higher eccentricities than for circular ones. This results from the apastron of the binary orbit being closer to the circumbinary gas for high eccentricities than for low ones. Therefore the resulting forces between binary system and gas are stronger.
- All binary and gas properties were combined into a fit formula Testing this fit formula using an orthogonal Latin Hypercube Sampling, an error of $\lesssim 6\%$ was calculated.

The here retrieved fit formula of the numerical simulation improves the analytic approximation by Stahler (2010), since now the wave generation and eccentric orbits are included. In the next chapter it will be investigated how a whole binary population is influenced by the orbital decay calculated via this fit formula. The results will be compared to Chap. 2, where the analytic approximation was applied to a binary population.

5 Consequences of orbital decay for a binary population in a typical cluster

In Chap. 4 the temporal evolution of single binary systems was investigated. Since most stars form in a cluster environment, the obtained results are now applied to a binary population typical for a cluster. This means that the fit formula for the orbital decay

$$a(t, r_{in}, \rho_0, c_s, a_0, e, q, M_{sys}, e) = a_0(1-\Delta_{num})(1-\Delta_{num}^{ecc})$$

$$\Delta_{num} = 0.6 \cdot \frac{q}{(1+q)^2} \left(\frac{c_s}{c_s^d}\right)^{0.4} \left(\frac{r_{in}^d}{r_{in}}\right)^4 \left(\frac{a_0}{a_0^d}\right) \left(\frac{\rho}{\rho^d}\right)^{3/4} \left(\frac{M_{sys}^d}{M_{sys}}\right)^{1/2} \left(\frac{t}{t^d}\right)^{9/10}$$

$$\Delta_{num}^{ecc} = (1.8 \cdot r_{in}^{-1.5} - 0.2) \cdot e \cdot \left(\frac{t}{t^d}\right)^{9/10},$$

which was retrieved from the numerical simulations is used to calculate the effect of orbital decay for an entire binary population. The temporal development of the period distribution of this binary population is monitored and the period distribution obtained after 1 Myr is compared to observations of the field binary population.

Additionally, the differences of these results to Chap. 2 are discussed, where the analytic approximation by Stahler (2010)

$$a_{approx}(t) = a_0(1-\Delta_{approx})$$

$$\Delta_{approx} = \frac{32\pi}{15} \frac{q}{(1+q)^2} \frac{\rho_0}{c_s^5} \frac{G^3 M_{\rm sys}^2}{a_0} t.$$

was used to calculate the period distribution change of a binary population. To ease comparison, an ONC-like cluster was modelled and the same binary population as in Chap. 2 was used. The binary development was investigated for a cluster evolution time of 1 Myr. After this, the cluster is assumed to disperse the gas and therefor the gas-induced orbital decay stops.

In Chap. 2 all binary systems were assumed to be on circular orbits, since the analytic approximation is only valid for circular orbits. Therefore, in a first step, the fit formula is applied to a binary population with only circular orbits. Secondly, the fit formula is applied to a binary population with an eccentricity distribution and the differences between both results are discussed.

5.1 Method

First the properties of the modelled **cluster** are defined. Equivalent to Chap. 2 the stellar density distribution of the ONC-like cluster was chosen to be nearly isothermal (see Eq. 2.1) and include mass segregation. The velocity and gravitational interactions of the stars are not considered here. As demonstrated in Chap. 2 the here neglected dynamical effects like binary destruction act on long-period binaries ($> 10^5$ days). Therefore, the orbital decay was investigated only for binaries with periods $\leq 10^5$ days.

In order for the gas-induced orbital decay to work, a binary system has to be surrounded by gas. Even during the first Myr, where the cluster is still embedded in gas, other stars might remove it. This can happen if the gravitational force of another nearby star is more dominant than the surrounding gas or the radiation pressure of the other star destroys the circumbinary gas environment. To consider this in the investigation, the here calculated orbital decay takes only place if other stars have a minimum mean distance to a binary system. This distance was estimated by having a larger mean distance between the stars than the sum of the inner radius r_{in} and at least ten wavelengths λ_{gas} of the resulting acoustic wave in the gas

$$\overline{R} \approx \rho_{star}^{-1/3} > r_{in} + 10\lambda_{gas} = r_{in} + 10\pi c_s \cdot \sqrt{\frac{4 \cdot \pi^2}{G \cdot M_{sys}} a^3}.$$

Here the mean distance is calculated via the stellar number density ρ_{star}, and the wavelength in the gas can be derived from $\lambda_{gas} = c_s \cdot T_{binary}/2$ (see Sec. 3.4.2) and the Kepler equation (see Eq. 1.4). This means that for high-mass systems the mean distance at which the orbital decay still takes place can be much smaller than for low-mass systems. In the case of $r_{in} = 2a$ and a solar-mass star with a semi-major axis of 100 AU, the mean distance between a binary system and any other star or system has to be larger than 2310 AU. For an ONC-like cluster a smaller mean distance is only reached in the dense inner cluster region, inside a radius of 0.02 pc from the cluster centre. There, the highest gas density can be found, but gravitational force or radiation pressure of the other stars are more dominant. Since in this sphere of 0.02 pc only a few stellar systems are enclosed, most binary systems of the here modelled binary population fulfil the minimum-distance criterion and will be processed by orbital decay.

For the gas properties, the observations are not conclusive so far. In contrast to Chap. 2 where the mean cluster gas density was modelled with an isothermal density distribution with a maximum density of 10^5 cm^{-3} and a constant sound speed of 0.49 km/s, here the standard scenario of Chap. 4 is used, since observations have shown, that the gas surrounding a just formed star is much denser and the sound speed higher. Therefore, the binary systems are for 1 Myr embedded in a gas density of 10^9 cm^{-3} with a sound speed of 2 km/s. The inner radius of a binary system, where the circumbinary gas starts, was chosen to be two semi-major axis.

In reality the density (and sound speed) varies throughout the cluster, with the highest density in the cluster centre. Thus, the observed mean density results from a highly varying local density, with stars being formed at the densest cores of these turbulent medium. So far it is unknown, how the density and sound speed of these cores might depend on the system mass of the binary system. Assuming the relatively high density of $10^9 \mathrm{cm}^{-3}$ gives a good upper limit, since around high-mass stars densities of $> 5 \cdot 10^9$ cm^{-3} were observed (Indriolo et al., 2013).

For the **binary population**, the initial distribution of the binary properties have to be chosen. Like in Chap. 2, the semi-major axis is initially log-uniform $f_a(a) \propto d\mathrm{N}/da \propto a^{-1}$ where $a \in [0.02\,\mathrm{AU}, 10000\,\mathrm{AU}]$ and the mass-ratio distribution follows $f_q(q) \propto q^{0.4}$ with $q = m_2/m_1 \in [0,1]$. The system mass distribution of the binary population is sampled from the stellar IMF given by Eq. 1.14 with $M_{sys} \in [0.08\,\mathrm{M}_\odot, 50\,\mathrm{M}_\odot]$.

The fit formula is limited to binary systems with $\mathbb{V} = v_{\mathrm{orbit}}/c_s \geq 1$, since the orbital decay does not act on binary systems with $\mathbb{V} < 1$ (see Sec. 4.2). Therefore, only binary systems which fulfil $\mathbb{V} \geq 1$ were processed by the orbital decay. For example for the solar-mass case, this restriction excludes all binary systems with a semi-major axis $a > 220$ AU, which corresponds to periods $T > 10^6$ days.

In contrast to the analytic approximation, which is only valid for circular orbits, the fit formula includes also binary systems with eccentric orbits. For comparison the fit formula is applied to a binary population with only circular orbits. Additionally, a more realistic thermal eccentricity distribution $f(e) = 2e$ is used (see Sec. 1.4) and compared to the results with binary systems on circular orbits.

In summary, the fit formula for the orbital decay is applied to all binary systems with periods lower than 10^5 days, a higher orbital velocity than the surrounding sound speed $\mathbb{V} \geq 1$ and an environment with a mean stellar distance $\overline{R} > r_{in} + 10\lambda$.

5.2 Results

The period distribution processed by the orbital decay is calculated for binary systems with M-dwarf primaries ($0.1\,\mathrm{M}_\odot < m_1 < 0.5\,\mathrm{M}_\odot$), G-star primaries ($0.7\,\mathrm{M}_\odot < m_1 < 1.3\,\mathrm{M}_\odot$), B-star primaries ($1.5\,\mathrm{M}_\odot < m_1 < 5.0\,\mathrm{M}_\odot$), and O-star primaries ($m_1 > 16\,\mathrm{M}_\odot$), to compare the period distributions to observations (see Sec. 1.2) and the results of Chap. 2.

Since in Chap. 2 all binary orbits were assumed to be circular, the fit formula was first applied to such a binary population with only circular orbits. The resulting binary population for binary systems with **solar-mass primaries** is shown as a dark blue line in Fig. 5.1. This period distributions results from an initially log-uniform period distribution, which is shown as a green line. The resulting period distribution with only circular orbits is also log-uniform. It can be seen that this binary population is not processed by the orbital decay, since initial and final period distribution

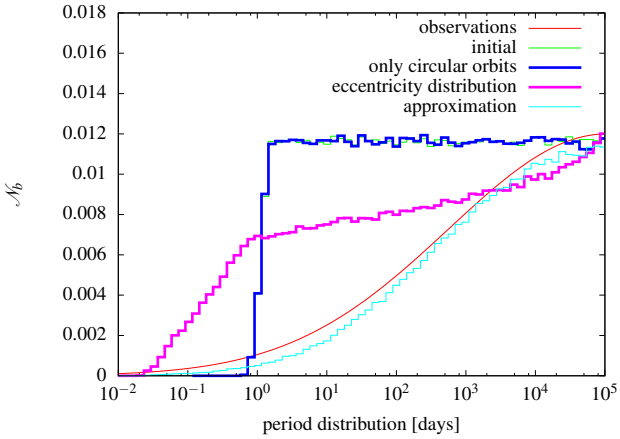

Figure 5.1: Observed period distributions for binaries with solar-mass primaries (red line) and effect of the orbital decay on an initially log-uniform distribution (green line) for binary population with only circular orbits (dark blue line) and with an eccentricity distribution of $f(e) = 2e$ (magenta line). For comparison the result of Chap. 2 is included (light blue line).

coincide.

The magenta line in Fig. 5.1 shows the resulting binary period distribution of a more realistic binary population with a thermal eccentricity distribution (Ambartsumian, 1937). This period distribution results from the same initial log-uniform period distribution processed by orbital decay, which was calculated via the fit formula retrieved in Chap. 4, differs significantly from the initial distribution. The difference between binary systems with circular orbits and binaries with highly eccentric orbits was already visible in Fig. 4.14b, where the orbital decay for systems with high eccentricities is much faster.

The results of Chap. 2 (light blue line), where the orbital decay was calculated via the analytic approximation by Stahler (2010), differ significantly from the initial log-uniform period distribution (green line), even if there all binaries were assumed to be on circular orbits. The reason for this is that the neglected wave generation process in the approximation overestimates the orbital decay.

Comparing the processed binary population with a thermal eccentricity distribution (magenta line) to the field observations of main-sequence stars by Raghavan et al. (2010) (red line), more binary systems are left for periods lower than 10^3 days in the calculation than expected. This results from the dependency of the orbital decay on the semi-major axis, where the orbital decay slows down as the semi-major axis decreases until no further orbital decay takes place. In contrast, in the analytic approximation the orbital decay speeds up for a decreasing semi-major axis. This leads to the conclusion, that the results of the approximation in Chap. 2 might have shown only by

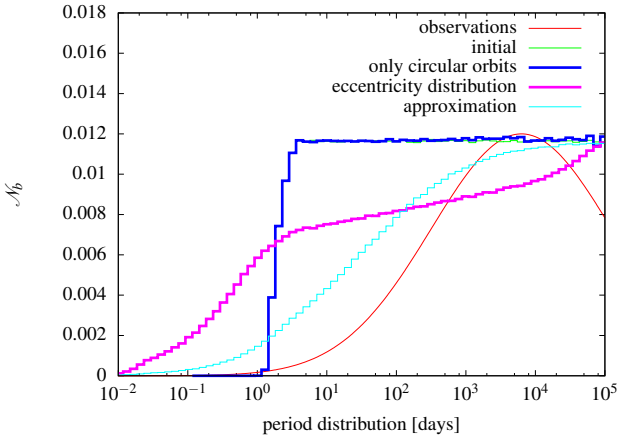

Figure 5.2: As in Fig. 5.1, but for the primary mass range of $0.1\mathrm{M}_\odot < m_1 < 0.5\mathrm{M}_\odot$.

chance a similar dependency than the observations.

To merge more binary systems with periods lower than 10^3 days the embedded time span would have to be longer, but this would also reduce the number of binary systems with periods between 10^3 and 10^5 days and thus not coincide with observations. Another possibility to merge more binary systems would be a higher gas density, but since here already a density of 10^9 cm^{-3} was used and densities $> 5 \cdot 10^9$ cm^{-3} are only observed around high-mass protostars (Indriolo et al., 2013), a higher density is not likely. Thus, the question arises if the initial period distribution is log-uniform on the short period side or if other processes alter the period distribution further.

In Sec. 2.5 we saw that a binary population processed by the analytic approximation is less capable of reproducing the period distributions, which were observed for main-sequence M-dwarf primaries ($0.1\ \mathrm{M}_\odot < m_1 < 0.5\ \mathrm{M}_\odot$), B-star primaries ($1.5\ \mathrm{M}_\odot < m_1 < 5.0\ \mathrm{M}_\odot$) and O-star primaries ($m_1 > 16\ \mathrm{M}_\odot$).

Figure 5.2 shows the binary population with **M-dwarf primaries** ($0.1\ \mathrm{M}_\odot < m_1 < 0.5\ \mathrm{M}_\odot$). The period distribution resulting from the binary population with only circular orbits remains again log-uniform (dark blue line). The initially log-uniform period distribution (green line) is processed by the orbital decay calculated via the fit formula for 1 Myr resulting in a shift towards lower periods and merging binary systems for the population with a thermal eccentricity distribution (magenta line). Neither the fit formula (magenta line) nor the analytic approximation (light blue line) processes the initially log-uniform period distribution in such a way to represent the fit to the observational data (red line) of Fischer & Marcy (1992).

In contrast to the analytic approximation, the period distribution resulting from the application of the fit formula shows less binaries for periods $> 10^2$ days and more binaries for periods

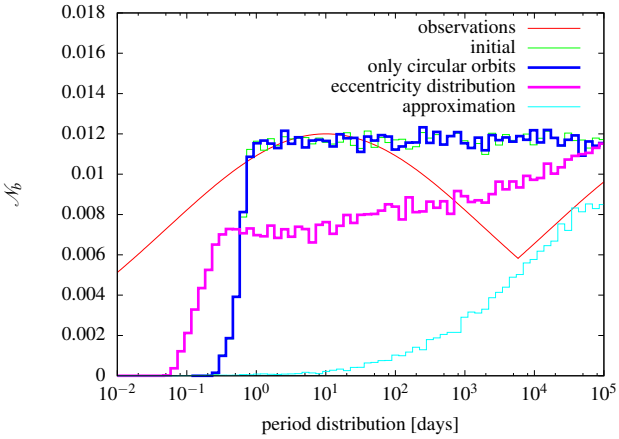

Figure 5.3: As in Fig. 5.1, but for the primary mass range of $1.5 M_\odot < m_1 < 5.0 M_\odot$.

$< 10^2$ days, which can be explained by comparing both equations. With decreasing semi-major axis, the orbit decays speeds up in the approximation (Eq. 4.3) and slows down in the fit formula (Eq. 4.7). Thus in the approximation, the short-period binary systems are more likely to be destroyed. For the period distribution resulting from the fit formula, a longer embedded time span or a higher gas density would lead to less binaries for periods $> 10^2$ days, but even more binary systems with periods $> 10^2$ days would be destroyed which means that the observed period distribution cannot be reproduced by changing these gas properties.

For binary systems with **B-star primaries** ($1.5\ \mathbf{M}_\odot < m_1 < 5.0\ \mathbf{M}_\odot$) the final period distribution of a binary population with only circular orbits remains log-uniform (dark blue line) after applying the fit formula. Using the same binary population, all binary systems with periods $< 10^2$ days were destroyed when applying the approximation (light blue line in Fig. 5.3). This contradicts the spectroscopic observations of (Carquillat & Prieur, 2007), who found binary systems in this period and mass range. However, after the application of the fit formula to a population with a thermal eccentricity distribution, considerable less binary systems than in the approximation have merged (magenta line). Thus, the mass dependency of the fit formula seems to reflect the observations better than the analytic approximation. Considering that for the fit formula the speed of orbital decay slows down with decreasing semi-major axis, even a lower gas density or a longer embedded time would not lead to a period distribution with a peak at the short period end.

The same is true for binary systems with **O-star primaries** $m_1 > 16\ \mathbf{M}_\odot$. There no binaries merge when applying the fit formula to a binary population on circular orbits (dark blue line) and nearly all binary systems merged when applying the analytic approach (light blue line in Fig. 5.4), which contradicts the observed overabundance of very-short period binary systems (red line).

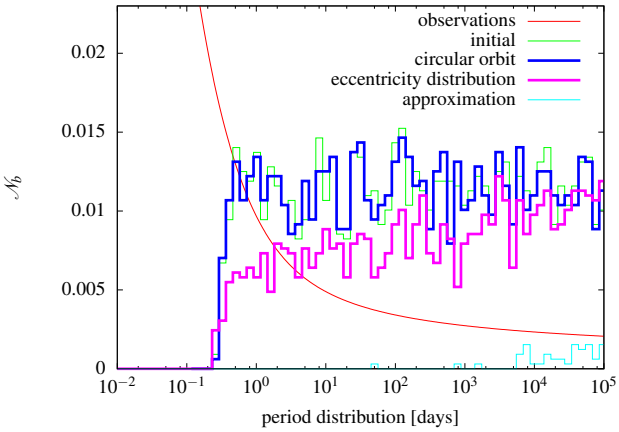

Figure 5.4: As in Fig. 5.1, but for the primary mass of $m_1 > 16\mathrm{M}_\odot$.

After the application of the fit formula to a binary population with a thermal eccentricity distribution, more short-period binary systems remain (magenta line) than in the approximation, but the fit to the observations cannot be reproduced.

On the one hand, radiation pressure of high-mass stars removes the gas faster than low-mass stars, resulting in these binaries being exposed shorter (< 1 Myr) to the effect of orbital decay and only a few high-mass binary systems with circumbinary discs were observed so far (e.g. Sánchez-Monge et al., 2013). This indicates a fast destruction of a disc and expulsion of other circumbinary gas, resulting in a less effective orbital decay. On the other hand, the gas surrounding high-mass protostars might be even denser ($> 5 \cdot 10^9$ cm^{-3} Indriolo et al., 2013) which would lead to a more effective orbital decay. It remains unknown which of these processes is dominant during the high-mass stellar evolution.

Summarising, these applications of the fit formula onto a whole binary population show that including the wave generation changes the resulting period distribution significantly. For the populations with binary systems assumed to be on circular orbits the period distribution remains log-uniform, which emphasises the importance to consider eccentric orbits. In the case of a thermal eccentricity distribution, especially the system mass and semi-major axis dependency seems to reflect the observations much better than the analytic approach. Nevertheless, for all mass-ranges the question remains if the initial period distribution is indeed log-uniform and if other processes influence short period binaries.

As mentioned in Chap. 2, an ONC-like cluster is only one representation of a cluster. Therefore, the results cannot represent the entire field binary population, which develops at least from two cluster types (see Sec. 1.3.3), ONC-like clusters and clusters with a much higher stellar density

throughout their evolution. Thus, the results presented here are only one example of how the orbital decay influences a typical binary population. Additionally, only the short period sides of the distributions are shown here. Thus, it is not possible to normalise these distributions.

The comparison of the results to the observational fits have to be considered with caution, since some of these observations have huge errors themselves (for a detailed discussion see Sec. 2.5). Thus, further observations of very young binary populations are necessary for a better comparison and to improve the simulations.

6 Discussion

The investigation of a complex system via numerical simulations, is restricted by the computational resources, the quality of observations needed for the modelled properties and the available theoretical models. This applies to some extent, when discussing the assumptions made in this thesis. These assumptions can be divided into those of the binary system simulations performed in Chap. 3 and 4 and those of applying the effect to a whole binary population in Chap. 2 and 5. For both investigations the restrictions imposed by the observations, theoretical models and computational resources are summarised in Tab. 6.1

First, the possible influences of the assumptions for the **binary system simulations** in Chap. 3 and 4 will be discussed. Ideally, simulations of the here investigated gas-induced orbital decay of a binary system should include also the formation process. This would lead to a better model of the gas surrounding the binary system. However, additional to the huge computational effort, which would restrict the number of cases which can be simulated in a reasonable time, the setup of the initial gas cloud would also introduce a new set of parameters to the investigation. Furthermore, the formation of binary systems is still an open question (see Sec. 1.3.2) and the effort to introduce a more self-consistent treatment would only lead to a larger parameter space. Given the fact that the binary formation process itself is unknown, one has to rely on observations and theoretical models of the earliest phases of binaries for the initial conditions and restrictions applied here.

Due to restricted computational resources the effects which take place inside the inner gas radius, were excluded in the here presented simulations. This results in a setup with no gas inside this inner radius and a uniform, non-rotating surrounding gas density outside this radius. The stars are treated as point masses and the monopole moment of the binary potential is subtracted from the total binary potential, because this monopole moment is usually counteracted by a gas density distribution and rotating of the surrounding gas. The consequences of these initial conditions and the resulting influences on the gas-induced orbital decay are the following:

Since the area next to the stars was not modelled here, accretion from a protostellar disk or even from the circumbinary disk was excluded. Here only the final system mass and mass-ratio was used to simulate the orbital decay. To include the accretion process, the simulation would start with a lower system mass and reach the final mass during the binary simulation.

Including accretion and internal processes during the protostellar phase would change the stellar radius during the binary evolution (see Fig. 1.7). For short period binary systems, this could

	binary system	cluster
initial conditions	no gas inside inner radius uniform surrounding density star as point masses excluding monopole moment	long periods not considered only stellar density and binary properties only one cluster type
excluded evolution processes	accretion radius evolution mass transfer & merger processes tidal interactions (circularisation) magnetic fields	stellar velocity three-body interactions changing gas environment radiation pressure

Table 6.1: Restrictions for the binary simulations and the cluster calculation.

influence the time at which the mass transfer between the stars starts. These processes would only be important if the merger process were modelled in detail. However, the merger process itself is complex. Depending on the age of each stellar component, the chemical processes during the merger differ and thus influence the outcomes of a binary merger (e.g. Glebbeek et al., 2013).

Tidal effects, like circularisation in binaries with very short periods, are not included here, since the stars are treated as point masses. The circularisation itself would slow down the orbital decay, but is only effective for periods $\lesssim 8$ days, which corresponds to a semi-major axis of 0.08 AU in the solar-mass case. Since the in Chap. 4 presented simulations show that the orbital decay can be neglected for such small semi-major axis, the circularisation would not influence the simulation results presented in this thesis. However, it needs to be investigated if this is still the case when including accretion and the changes of the protostellar radius.

Flows within the gas and even through the gap might also influence the gas-induced orbital decay. Artymowicz & Lubow (1996) found, that a binary system might accrete gas from a circumbinary disc, without closing the low density region between circumbinary and circumstellar disc. Overall, the circumbinary disc was found to reduce the semi-major axis and increase the eccentricity of the binary system, but they presented only a few case studies (Artymowicz et al., 1991). Additionally, their low-resolution simulations follow the binary orbits only for 70 periods, which corresponds to $\approx$ 70.000 years. Therefore, these simulations already suggest the effect described in this thesis, but only for a very limited set of parameters.

Artymowicz & Lubow (1996) used a rotating gas profile with a surface density of $\Sigma(r) \propto r^{-1}$. By contrast, here a non-rotating 3D gas sphere with a uniform gas distribution was used. The efficiency of the angular momentum transport might differ for these two environments. The presented results show that, for the gas, the efficiency depends only on the sound speed of the gas, but having

a rotating disc would introduce a new set of properties.

Here, magnetic fields have not been included. However, in MHD simulations of T Tauri stars by Shi et al. (2012), the same geometry of circumstellar discs, gap, and circumbinary disc was found as in the HD T Tauri simulations used as basis for the here presented binary simulation (see Sec. 3.1). Additionally, they found that, at least for the examples considered in their study, the angular momentum gained through accretion and the angular momentum loss due to the torques is nearly balanced. Since the gain of mass through accretion would slow down the orbital decay, these effects should be included in a further study.

Now looking at a whole **cluster population** as investigated in Chap. 2 and 5, a self consistent formation and evolution of such a cluster cannot be simulated with current knowledge and computational resources. Thus, for the cluster itself only the stellar density distribution and the binary properties are given in Chap. 5. This means that the velocity of the stars inside the cluster and the resulting three-body interactions and gas dynamic are neglected. Binary systems with periods $> 10^5$ days are not considered, since these are mostly influenced by the three-body interactions. Additionally, the presented ONC-like cluster is an example for one type of clusters. Thus, the cluster results can only be considered as a first step in understanding how the gas-induced orbital decay would influence a whole binary population.

The orbital decay ends when the gas is expelled from the cluster due to radiation pressure or even supernova explosions. On short time-scales (< 1 Myr), the radiation pressure of a binary system could also influence its inner radius where the circumbinary gas starts, which is a crucial parameter when determine the effect of orbital decay. Additionally, the radiation pressure might also influences the gas environment of nearby binary systems and thus their orbital decay. For nearby binary systems and even the radiating star itself, it is not clear how the gas inside the inner radius interacts with this radiation. Thus, so far the radiation pressure cannot be calculated for the circumbinary gas. For future investigations, a detailed study of the processes inside the inner radius would be vital to improve the orbital decay simulations.

Even the time evolution for the gas distribution of a cluster is unknown. Parmentier & Pfalzner (2013) developed a model calculating the mean gas density evolution in an ONC-like cluster, but this does not include the local gas density surrounding a binary system. At first, the local density might be much higher than the mean density, since the binary system has just formed from this gas. Later, the local density could be even lower than the mean density, when dispersed by radiation pressure. The first would increase the orbital decay whereas the latter decreases the orbital decay.

Comparing the period distribution resulting from the orbital decay with observations of a field binary population shows, that the above discussed restrictions have a huge impact. Additionally, the log-uniform period distribution is questionable, since only a few protostellar binary systems were observed in this stage so far. Furthermore, since the interaction with other stars is neglected,

it is also neglected how the orbital decay might influence the cluster dynamic. Thus, the here applied cluster model is only a first approach.

7 Summary and conclusion

In this thesis, the influences of the surrounding gas on a young binary system was investigated. This included detailed numerical studies of isolated binary systems and investigations of the consequences for a whole population of binaries as typically found in young clusters.

The effect of the gas on the binary is angular momentum loss due to the excitation of acoustic waves in the surrounding gas, leading to a decay of the orbit. First, the analytic approximation of Stahler (2010) was applied to a binary population, assuming an initially log-uniform period distribution (Chap. 2). In this approximation all binaries were assumed to be on circular orbits. The results were combined with the destruction of long-period binaries due to three-body interactions, known from cluster simulations by Kaczmarek et al. (2011). The combined binary population reproduces the period distribution observed for main-sequence solar-mass stars very well, but fails to match observations of other mass ranges.

The main shortcoming of the analytic approximation, besides not being valid for circular orbit, is that the wave generation itself is not calculated. Therefore, in a second investigation a self-consistent hydrodynamic code was developed to overcome these restrictions (Chap. 3). This code was used to simulate the evolution of the binary orbit (Chap. 4). It was shown, that the initial binary properties affect the shape of the resulting outgoing density waves in the surrounding gas, which influence the efficiency of the angular momentum transport. The effect of these density waves onto the semi-major axis of the binary system was investigated for different gas and binary properties. The resulting dependencies of the gas-induced orbital decay were combined into a fit formula (Eq. 4.7).

This fit formula was tested using an orthogonal Latin Hypercube sample, leading to an error of $\lesssim 6\%$. The orthogonal Latin Hypercube method provides a parameter set with optimal coverage of this huge parameter space, with simulations of only 16 different parameter sets to test the fit formula.

It was shown, that the efficiency of the wave generation itself depends on the fraction of $\mathbb{V} = v_{\rm orbit}/c_s$, with $v_{\rm orbit} = \sqrt{G \cdot M_{\rm sys}/a}$ being the orbital velocity of the binary system. Since the wave generation was neglected by the analytic approximation, all properties which are involved in the wave generation show a different scaling as predicted by the approximation (a, M_{sys}, c_s) or were not necessary to calculate for the approximation (r_{in}). As a consequence, neglecting the wave generation leads to overestimating the orbital decay in the analytic approach. However,

an investigation of eccentric orbits showed, that the orbital decay is faster for binary systems with higher eccentricities than their circular counterparts.

The influence of the eccentricity is also visible when applying the fit formula to a whole binary population in a young star cluster (see Chap. 5). There, binary populations with only circular orbits show no visible difference between the initial and final period distribution. In contrast, the final period distribution of binary populations with an eccentricity distribution differ significantly from the initial distribution. However, also this period distribution processed by the orbital decay does not reproduce the observations of field binary populations. This is due to three different reasons. The here modelled ONC-like cluster is only one example for stellar clusters which will resolve into the field population and therefore cannot represent the whole field population. Furthermore, the modelling of the cluster neglects the stellar dynamic and the used initial properties of the modelled binary population. Especially the initial period distribution needs to be substantiated by observations of more binary systems covering all mass ranges. Finally, more detailed observations of protostellar binary populations are needed to improve the simulation of the gas-induced orbital decay.

In summary, the here developed numerical simulation can be used to model the gas-induced orbital decay. The application to a binary population of a young star cluster shows, that this effect cannot be neglected when investigating the gas embedded phase of a young cluster. There, most stars are part of a binary or higher order system, but so far only the stellar interactions leading to the destruction of long period binaries via three body encounters were investigated.

When including the gas-induced orbital decay, the final period distribution changes significantly. Binary systems with periods $< 10^5$ days are shifted towards lower periods and even merge. So far the formation of more massive stars via merger was only considered for stellar densities $\geq 10^6$ stars pc^{-3} (Bonnell & Bate, 2005), which is rather unlikely for most clusters. For example, in an ONC-like cluster the stellar density reaches only $\approx 7 \cdot 10^4$ stars pc^{-3} in the cluster centre. Thus, binary systems processed by the gas-induced orbital decay are more likely to merge.

The binary properties also influence the star which might result from a merger. The merger of binary systems is believed to result in so called fast rotators, since the external angular momentum might be converted into internal angular momentum. Additionally, it might be observable if a star results from the merger during the embedded phase where the merging stars are still young or later when the stars are already on the main sequence. The resulting merger product should be nitrogen-rich if the merger happens on the main sequence and nitrogen-normal otherwise (Glebbeek et al., 2013).

Observations of the field population showed, that the number of binaries with high-mass primaries ($m_1 > 16\,\mathrm{M}_\odot$) increases with decreasing period. The orbital decay is a possible mechanism to shift longer periods toward shorter once. However, in the here applied cluster environment more

binary systems with short periods and high-mass primaries are merged than shifted towards these short periods. The radiation pressure could prohibit these binary systems from merging, since such massive stars might remove the surrounding gas in < 1 Myr due to their radiation pressure. For example, for a binary system with a system mass of 20 $M_{\odot}$ a period of $1.4 \cdot 10^4$ days and an eccentricity of 0.7, in a surrounding gas density of $5 \cdot 10^9$ cm^{-3} and a sound speed of 2 km/s, the gas-induced orbital decay would still reduce the period by 26% even when considering that the embedded phase might be only 0.5 Myr.

Investigations of other effects between the binary systems and the surrounding gas would be vital for a future study. It is especially interesting to consider how a binary system and the cluster environment influences the inner gas radius via radiation pressure, accretion and gas dynamics or the surrounding gas density and sound speed. The here presented model of the gas-induced orbital decay can then be used to interpret this future observations.

Bibliography

Aarseth, S. J. 1963, Monthly Notices of the Royal Astronomical Society, 126, 223

Aarseth, S. J. 1971, Astrophysics and Space Science, 14, 20

Aarseth, S. J. 2003, Gravitational N-Body Simulations

Abt, H. A., Gomez, A. E., & Levy, S. G. 1990, The Astrophysical Journal Supplement Series, 74, 551

Abt, H. A. & Levy, S. G. 1985, The Astrophysical Journal Supplement Series, 59, 229

Ambartsumian, V. A. 1937, Astronomicheskii Zhurnal, 14, 207

Andre, P., Ward-Thompson, D., & Barsony, M. 2000, Protostars and Planets IV, 59

Andrews, S. M. & Williams, J. P. 2007, The Astrophysical Journal, 671, 1800

Andrews, S. M., Wilner, D. J., Hughes, A. M., Qi, C., & Dullemond, C. P. 2009, The Astrophysical Journal, 700, 1502

Arons, J. & Max, C. E. 1975, The Astrophysical Journal, 196, L77

Artymowicz, P., Clarke, C. J., Lubow, S. H., & Pringle, J. E. 1991, The Astrophysical Journal Letters, 370, L35

Artymowicz, P. & Lubow, S. H. 1994, The Astrophysical Journal, 421, 651

Artymowicz, P. & Lubow, S. H. 1996, The Astrophysical Journal Letters, 467, L77

Bachiller, R. 1996, Annual Review of Astronomy and Astrophysics, 34, 111

Bally, J. & Zinnecker, H. 2005, The Astrophysical Journal, 129, 2281

Banerjee, R. & Pudritz, R. E. 2007, The Astrophysical Journal, 660, 479

Banerjee, S., Kroupa, P., & Oh, S. 2012, The Astrophysical Journal, 746, 15

Bate, M. R. 2009, Monthly Notices of the Royal Astronomical Society, 392, 590

Bate, M. R. & Bonnell, I. A. 1997, Monthly Notices of the Royal Astronomical Society, 285, 33

Binney, J. & Tremaine, S. 1987, Galactic dynamics

Bisikalo, D. V., Sytov, A. Y., Fateeva, A. M., & Kaygorodov, P. V. 2012, in Numerical Modeling of Space Plasma Slows (ASTRONUM 2011), Vol. 459, 55

Blitz, L. 1993, in Protostars and Planets III, ed. E. H. Levy & J. I. Lunine, 125–161

Boden, A. F., Akeson, R. L., Sargent, A. I., et al. 2009, The Astrophysical Journal Letters, 696, L111

Bonnell, I. A. & Bate, M. R. 2005, Monthly Notices of the Royal Astronomical Society, 362, 915

Bonnell, I. A. & Bate, M. R. 2006, Monthly Notices of the Royal Astronomical Society, 370, 488

Bonnell, I. A., Bate, M. R., Clarke, C. J., & Pringle, J. E. 1997, Monthly Notices of the Royal Astronomical Society, 285, 201

Bonnell, I. A. & Davies, M. B. 1998, Monthly Notices of the Royal Astronomical Society, 295, 691

Borissova, J., Ivanov, V. D., Hanson, M. M., et al. 2008, Astronomy and Astrophysics, 488, 151

Bressert, E., Bastian, N., Gutermuth, R., et al. 2010, Monthly Notices of the Royal Astronomical Society, 409, L54

Carquillat, J.-M. & Prieur, J.-L. 2007, Monthly Notices of the Royal Astronomical Society, 380, 1064

Carroll, B. W. & Ostlie, D. A. 2006, An introduction to modern astrophysics and cosmology

Caselli, P. & Myers, P. C. 1995, The Astrophysical Journal, 446, 665

Cash, J. R. & Karp, A. H. 1990, ACM Trans. Math. Softw., 16, 201

Chabrier, G. 2001, The Astrophysical Journal, 554, 1274

Chabrier, G. 2002, The Astrophysical Journal, 567, 304

Chini, R., Hoffmeister, V., Kimeswenger, S., et al. 2004, Nature, 429, 155

Chini, R., Hoffmeister, V. H., Nasseri, A., Stahl, O., & Zinnecker, H. 2012, Monthly Notices of the Royal Astronomical Society, 424, 1925

Clark, P. C., Bonnell, I. A., Zinnecker, H., & Bate, M. R. 2005, Monthly Notices of the Royal Astronomical Society, 359, 809

Clarke, C. J., Harper-Clark, E., & Lodato, G. 2007, Monthly Notices of the Royal Astronomical Society, 381, 1543

Connelley, M. S., Reipurth, B., & Tokunaga, A. T. 2008a, The Astronomical Journal, 135, 2496

Connelley, M. S., Reipurth, B., & Tokunaga, A. T. 2008b, The Astronomical Journal, 135, 2526

Courant, R., Friedrichs, K., & Lewy, H. 1928, Mathematische Annalen, 100, 32

Dale, J. E., Ercolano, B., & Bonnell, I. A. 2012, Monthly Notices of the Royal Astronomical Society, 427, 2852

Davis, P. J., Siess, L., & Deschamps, R. 2013, Astronomy and Astrophysics, 556, 4

De Rosa, R. J., Bulger, J., Patience, J., et al. 2011, Monthly Notices of the Royal Astronomical Society, 415, 854

de Val-Borro, M., Gahm, G. F., Stempels, H. C., & Peplinski, A. 2011, Monthly Notices of the Royal Astronomical Society, 413, 2679

de Wit, W. J., Hoare, M. G., Oudmaijer, R. D., et al. 2011, Astronomy and Astrophysics, 526, L5

Doyle, L. R., Carter, J. A., Fabrycky, D. C., et al. 2011, Science, 333, 1602

Duchêne, G. & Kraus, A. 2013, Annual Review of Astronomy and Astrophysics, 51, 269

Dukes, D. & Krumholz, M. R. 2012, The Astrophysical Journal, 754, 56

Duquennoy, A. & Mayor, M. 1991, Astronomy and Astrophysics, 248, 485

Eggleton, P. 2006, Evolutionary Processes in Binary and Multiple Stars

Elmegreen, B. G. 2007, The Astrophysical Journal, 668, 1064

Fateeva, A. M., Bisikalo, D. V., Kaygorodov, P. V., & Sytov, A. Y. 2011, Astrophysics and Space Science, 335, 125

Figer, D. F. 2008, in IAU Symposium, Vol. 250, IAU Symposium, ed. F. Bresolin, P. A. Crowther, & J. Puls, 247–256

Fischer, D. A. & Marcy, G. W. 1992, The Astrophysical Journal, 396, 178

Gammie, C. F. 2001, The Astrophysical Journal, 553, 174

Garcia, P. J. V., Benisty, M., Dougados, C., et al. 2013, Monthly Notices of the Royal Astronomical Society, 430, 1839

Glebbeek, E., Gaburov, E., Portegies Zwart, S., & Pols, O. R. 2013, Monthly Notices of the Royal Astronomical Society, 434, 3497

Goodwin, S. P. 2010, Royal Society of London Philosophical Transactions Series A, 368, 851

Grellmann, R., Preibisch, T., Ratzka, T., et al. 2013, Astronomy and Astrophysics, 550, A82

Heggie, D. C. 1975, Monthly Notices of the Royal Astronomical Society, 173, 729

Hillenbrand, L. A. 1997, The Astrophysical Journal, 113, 1733

Hillenbrand, L. A. & Carpenter, J. M. 2000, The Astrophysical Journal, 540, 236

Hillenbrand, L. A. & Hartmann, L. W. 1998, The Astrophysical Journal, 492, 540

Hoare, A., Regan, D. G., & Wilson, D. P. 2008, Theoretical Biology and Medical Modelling, 5, 4, PMID: 18304361

Hogerheijde, M. 1998, doctoral thesis, Leiden University

Hoyle, F. 1953, The Astrophysical Journal, 118, 513

Huff, E. M. & Stahler, S. W. 2007, The Astrophysical Journal, 666, 281

Indriolo, N., Neufeld, D. A., Seifahrt, A., & Richter, M. J. 2013, The Astrophysical Journal, 776, 8

Inutsuka, S.-I. & Miyama, S. M. 1992, The Astrophysical Journal, 388, 392

Ivanova, N., Justham, S., Chen, X., et al. 2013, Astronomy and Astrophysics Review, 21, 59

Jensen, E. L. N., Dhital, S., Stassun, K. G., et al. 2007, The Astronomical Journal, 134, 241

Jensen, E. L. N. & Mathieu, R. D. 1997, The Astronomical Journal, 114, 301

Jorissen, A. & Frankowski, A. 2008, in American Institute of Physics Conference Series, Vol. 1057, American Institute of Physics Conference Series, ed. P. Pellegrini, S. Daflon, J. S. Alcaniz, & E. Telles, 1–55

Kaczmarek, T. 2012, doctoral thesis, Universität zu Köln

Kaczmarek, T., Olczak, C., & Pfalzner, S. 2011, Astronomy and Astrophysics, 528, 144

Kahn, F. D. 1974, Astronomy and Astrophysics, 37, 149

Kalas, P. & Jewitt, D. 1997, Nature, 386, 52

Khaliullin, K. F. & Khaliullina, A. I. 2010, Monthly Notices of the Royal Astronomical Society, 401, 257

Klassen, M., Pudritz, R. E., & Peters, T. 2012, Monthly Notices of the Royal Astronomical Society, 2443

Klessen, R. S. 2011, in EAS Publications Series, Vol. 51, EAS Publications Series, ed. C. Charbonnel & T. Montmerle, 133–167

Klessen, R. S., Heitsch, F., & Low, M. M. 2000, The Astrophysical Journal, 535, 887

Köhler, R., Petr-Gotzens, M. G., McCaughrean, M. J., et al. 2006, Astronomy and Astrophysics, 458, 461

Korntreff, C., Kaczmarek, T., & Pfalzner, S. 2012, Astronomy and Astrophysics, 543, 126

Kouwenhoven, M. B. N., Brown, A. G. A., Goodwin, S. P., Zwart, S. F. P., & Kaper, L. 2009, Astronomy and Astrophysics, 493, 979

Kouwenhoven, M. B. N., Brown, A. G. A., Zinnecker, H., Kaper, L., & Zwart, S. F. P. 2005, Astronomy and Astrophysics, 430, 137

Kouwenhoven, M. B. N., Brown, A. G. A., Zwart, S. F. P., & Kaper, L. 2007, Astronomy and Astrophysics, 474, 77

Kouwenhoven, M. B. N., Goodwin, S. P., Parker, R. J., et al. 2010, Monthly Notices of the Royal Astronomical Society, 404, 1835

Kratter, K. M., Matzner, C. D., & Krumholz, M. R. 2008, The Astrophysical Journal, 681, 375

Kratter, K. M., Matzner, C. D., Krumholz, M. R., & Klein, R. I. 2010, The Astrophysical Journal, 708, 1585

Kraus, A. L., Ireland, M. J., Martinache, F., & Hillenbrand, L. A. 2011, The Astrophysical Journal, 731, 8

Kraus, S., Hofmann, K.-H., Menten, K. M., et al. 2010, Nature, 466, 339

Kroupa, P. 1995a, Monthly Notices of the Royal Astronomical Society, 277, 1491

Kroupa, P. 1995b, Monthly Notices of the Royal Astronomical Society, 277, 1522

Kroupa, P. 1998, Monthly Notices of the Royal Astronomical Society, 298, 231

Kroupa, P. 2001, Monthly Notices of the Royal Astronomical Society, 322, 231

Kroupa, P. & Bouvier, J. 2003, Monthly Notices of the Royal Astronomical Society, 346, 343

Kroupa, P. & Burkert, A. 2001, The Astrophysical Journal, 555, 945

Krumholz, M. R. & McKee, C. F. 2008, Nature, 451, 1082

Kuiper, R., Klahr, H., Beuther, H., & Henning, T. 2010, The Astrophysical Journal, 722, 1556

Kuiper, R., Klahr, H., Beuther, H., & Henning, T. 2011, The Astrophysical Journal, 732, 20

Kunz, M. W. & Mouschovias, T. C. 2009, The Astrophysical Journal, 693, 1895

Lada, C. J. & Lada, E. A. 2003, Annual Review of Astronomy and Astrophysics, 41, 57

Larson, R. B. 1973, Annual Review of Astronomy and Astrophysics, 11, 219

Larsson, S. & Thomee, V. 2003, Partial Differential Equations with Numerical Methods, 45th edn. (Springer-Verlag)

Lehmann, H., Vitrichenko, E., Bychkov, V., Bychkova, L., & Klochkova, V. 2010, Astronomy and Astrophysics, 514, 34

Leisawitz, D., Bash, F. N., & Thaddeus, P. 1989, The Astrophysical Journal Supplement Series, 70, 731

Luhman, K. L., Mamajek, E. E., Allen, P. R., & Cruz, K. L. 2009, The Astrophysical Journal, 703, 399

Machida, M. N. & Matsumoto, T. 2011, Monthly Notices of the Royal Astronomical Society, 413, 2767

Machida, M. N., Tomisaka, K., Matsumoto, T., & Inutsuka, S.-i. 2008, The Astrophysical Journal, 677, 327

Marks, M., Kroupa, P., & Oh, S. 2011, Monthly Notices of the Royal Astronomical Society, 417, 1684

Maschberger, T. 2013, Monthly Notices of the Royal Astronomical Society, 429, 1725

Matzner, C. D. & McKee, C. F. 2000, The Astrophysical Journal, 545, 364

McCaughrean, M., Zinnecker, H., Andersen, M., Meeus, G., & Lodieu, N. 2002, The Messenger, 109, 28

McKee, C. F. & Tan, J. C. 2002, Nature, 416, 59

McKee, C. F. & Tan, J. C. 2003, The Astrophysical Journal, 585, 850

Menten, K. M., Reid, M. J., Forbrich, J., & Brunthaler, A. 2007, Astronomy and Astrophysics, 474, 515

Meru, F. & Bate, M. R. 2011, Monthly Notices of the Royal Astronomical Society, 410, 559

Moeckel, N. & Bally, J. 2007, The Astrophysical Journal, 656, 275

Myers, P. C. & Fuller, G. A. 1992, The Astrophysical Journal, 396, 631

Myers, P. C. & Goodman, A. A. 1988, The Astrophysical Journal, 326, L27

Najita, J., Carr, J. S., & Mathieu, R. D. 2003, The Astrophysical Journal, 589, 931

Offner, S. S. R., Klein, R. I., McKee, C. F., & Krumholz, M. R. 2009, The Astrophysical Journal, 703, 131

Offner, S. S. R., Kratter, K. M., Matzner, C. D., Krumholz, M. R., & Klein, R. I. 2010, The Astrophysical Journal, 725, 1485

Olczak, C., Pfalzner, S., & Eckart, A. 2010, Astronomy and Astrophysics, 509, 63

Orosz, J. A., Welsh, W. F., Carter, J. A., et al. 2012a, The Astrophysical Journal, 758, 87

Orosz, J. A., Welsh, W. F., Carter, J. A., et al. 2012b, Science, 337, 1511

Paczynski, B. 1971, Annual Review of Astronomy and Astrophysics, 9, 183

Padmanabhan, T. 2001, Theoretical Astrophysics - Volume 2, Stars and Stellar Systems

Parker, R. J., Goodwin, S. P., & Allison, R. J. 2011, Monthly Notices of the Royal Astronomical Society, 418, 2565

Parker, R. J., Goodwin, S. P., Kroupa, P., & Kouwenhoven, M. B. N. 2009, Monthly Notices of the Royal Astronomical Society, 397, 1577

Parmentier, G. & Pfalzner, S. 2013, Astronomy and Astrophysics, 549, 132

Pelupessy, F. I. & Portegies Zwart, S. 2012, Monthly Notices of the Royal Astronomical Society, 420, 1503

Pfalzner, S. 2009, Astronomy and Astrophysics, 498, L37

Pfalzner, S. 2011, Astronomy and Astrophysics, 536, 90

Pfalzner, S. & Kaczmarek, T. 2013, Astronomy and Astrophysics, 559, 38

Pfalzner, S. & Olczak, C. 2007, Astronomy and Astrophysics, 475, 875

Preibisch, T., Balega, Y., Hofmann, K.-H., Weigelt, G., & Zinnecker, H. 1999, New Astronomy, 4, 531

Preibisch, T., Ratzka, T., Gehring, T., et al. 2011, Astronomy and Astrophysics, 530, 40

Raghavan, D., McAlister, H. A., Henry, T. J., et al. 2010, The Astrophysical Journal Supplement Series, 190, 1

Reid, I. N. & Gizis, J. E. 1997, The Astronomical Journal, 113, 2246

Reipurth, B., Clarke, C. J., Boss, A. P., et al. 2014, Protostars and Planets VI, 1403, 1907

Reipurth, B., Guimaraes, M. M., Connelley, M. S., & Bally, J. 2007, The Astronomical Journal, 134, 2272

Rice, W. K. M., Lodato, G., & Armitage, P. J. 2005, Monthly Notices of the Royal Astronomical Society, 364, L56

Salpeter, E. E. 1955, The Astrophysical Journal, 121, 161

Sana, H., de Koter, A., de Mink, S. E., et al. 2013, Astronomy & Astrophysics, 550, A107

Sana, H., de Mink, S. E., de Koter, A., et al. 2012, Science, 337, 444

Sánchez-Monge, A., Cesaroni, R., Beltran, M. T., et al. 2013, Astronomy and Astrophysics, 552, L10

Shi, J.-M., Krolik, J. H., Lubow, S. H., & Hawley, J. F. 2012, The Astrophysical Journal, 749, 118

Shu, F. H., Adams, F. C., & Lizano, S. 1987, Annual Review of Astronomy and Astrophysics, 25, 23

Sridharan, T. K., Beuther, H., Saito, M., Wyrowski, F., & Schilke, P. 2005, The Astrophysical Journal, 634, L57

Stahler, S. W. 2010, Monthly Notices of the Royal Astronomical Society, 402, 1758

Sytov, A. Y., Kaigorodov, P. V., Fateeva, A. M., & Bisikalo, D. V. 2011, Astronomy Reports, 55, 793

Tan, J. C., Kong, S., Butler, M. J., Caselli, P., & Fontani, F. 2013, The Astrophysical Journal, 779, 96

Thompson, M. J. 2006, An Introduction to Astrophysical Fluid Dynamics (Imperial College Press)

Toomre, A. 1964, The Astrophysical Journal, 139, 1217

Tsuribe, T. & Inutsuka, S.-I. 1999, The Astrophysical Journal, 523, L155

Unsöld, A. & Baschek, B. 2002, Der neue Kosmos. Einführung in die Astronomie und Astrophysik

Weigelt, G., Balega, Y., Preibisch, T., et al. 1999, Astronomy and Astrophysics, 347, L15

Welsh, W. F., Orosz, J. A., Carter, J. A., et al. 2012, Nature, 481, 475

Whitworth, A. 1979, Monthly Notices of the Royal Astronomical Society, 186, 59

Wolff, S. C., Strom, S. E., Dror, D., Lanz, L., & Venn, K. 2006, The Astronomical Journal, 132, 749

Zahn, J.-P. & Bouchet, L. 1989, Astronomy and Astrophysics, 223, 112

Zhang, Y., Tan, J. C., & McKee, C. F. 2013, The Astrophysical Journal, 766, 86

Zhao, B. & Li, Z.-Y. 2013, The Astrophysical Journal, 763, 7

Zhao, B., Li, Z.-Y., & Kratter, K. M. 2013, ArXiv e-prints 1308.0830

Zwicky, F. 1953, Publications of the Astronomical Society of the Pacific, 65, 205

A Tables

A.1 Latin hypercube parameters for circular orbits

r_{in}	ρ	c_s	a(0Myr)	q	M_{sys}	a_{sim}(1Myr)	a_{calc}(1Myr)	Error [loss %]
3.24	9.21E+009	0.69	41.49	0.73	15.60	41.34	41.37	-0.08
2.92	7.18E+009	1.32	83.78	0.34	5.39	81.05	82.43	-1.65
4.46	1.20E+009	1.03	44.97	0.62	0.10	44.44	44.96	-1.15
3.10	9.72E+009	1.52	63.00	0.22	3.59	61.59	62.22	-1.00
3.44	2.02E+009	2.13	87.81	0.09	1.78	87.49	87.54	-0.06
4.29	9.14E+008	0.93	55.30	0.46	6.86	54.76	55.28	-0.94
3.57	6.78E+009	1.82	91.49	0.99	2.70	90.10	90.09	0.01
2.64	4.49E+009	1.79	64.81	0.41	14.01	63.20	64.22	-1.57
2.05	2.64E+009	1.42	58.58	0.12	8.72	56.40	57.91	-2.57
3.86	8.34E+009	0.56	51.19	0.55	1.47	49.93	50.88	-1.85
4.05	7.58E+009	2.42	94.30	0.95	10.77	93.59	93.94	-0.37
3.75	5.94E+009	2.01	81.05	0.28	13.46	80.71	80.88	-0.21
1.66	1.48E+008	1.19	73.97	0.02	8.98	73.44	73.90	-0.62
2.29	1.55E+009	0.49	72.11	0.86	14.56	71.96	71.64	0.44
2.83	3.01E+009	1.67	52.12	0.67	7.91	50.99	51.78	-1.52

Table A.1: Parameter selection for an orthogonal latin hypercube (column 1-7). Simulated (column 8) and calculated (column 9) semi-major axis and resulting differences between the semi-major axis loss of both (column 10).

.

A.2 Latin hypercube parameters for eccentric orbits

r_{in}	ρ	c_s	a(0Myr)	e	q	M_{sys}	a_{sim}(1Myr)	a_{calc}(1Myr)	Error
3.74	8.72E+09	2.49	77.35	0.79	0.52	6.91	68.77	73.45	-6.05
3.96	8.44E+09	0.63	68.34	0.53	0.13	4.38	64.87	67.11	-3.28
3.28	7.27E+08	1.39	88.70	0.66	0.70	8.37	87.80	82.43	6.05
1.96	9.01E+09	2.16	47.69	0.11	0.27	4.99	39.21	41.25	-4.21
2.23	5.38E+09	0.69	95.56	0.01	0.92	13.60	89.58	92.13	-2.67
2.87	1.33E+09	1.26	84.52	0.19	0.81	9.93	83.32	81.30	2.39
2.83	7.50E+09	1.47	71.27	0.49	0.37	1.30	56.49	60.49	-5.61
1.77	5.65E+09	2.15	54.99	0.05	0.16	15.02	51.75	51.45	0.54
3.56	9.67E+09	1.62	99.99	0.46	0.08	5.89	92.27	96.32	-4.05
3.08	6.98E+09	0.97	79.98	0.40	0.06	3.31	77.26	75.27	2.48
4.43	6.10E+09	1.79	44.85	0.42	0.41	11.06	42.96	44.91	-4.33
2.51	4.21E+09	1.01	55.59	0.13	0.73	12.39	53.68	53.10	1.06
2.56	4.26E+08	2.34	64.57	0.30	0.59	7.34	63.70	59.60	6.34
4.30	2.24E+09	1.98	41.96	0.73	0.99	11.96	41.92	41.86	0.14
4.19	1.60E+09	1.20	62.41	0.21	0.86	0.45	62.04	61.67	0.59
2.28	4.99E+09	0.35	49.29	0.60	0.50	2.95	$\mathbb{V} < 1$	$\mathbb{V} < 1$	0

Table A.2: Parameter selection for an orthogonal latin hypercube (column 1-6). Simulated (column 7) and calculated (column 8) semi-major axis and resulting differences between the semi-major axis loss of both (column 9).

Acknowledgements

First of all, I would like to express my deepest gratitude to my advisors, Prof. Dr. Susanne Pfalzner and Dr. Lukas Arnold, for their valuable guidance as well as their excellent and challenging supervision. They were always a great support for me and my research.

Furthermore, it is a pleasure to give my sincere thanks to those who made this thesis possible, especially Andreas Breslau and Kirsten Vinke, for their enduring support and intensive discussions. I would also like to thank my colleagues from the Max-Planck-Institute for radio astronomy for supporting the astrophysical part of my thesis and my colleagues from the Forschungszentrum Jülich GmbH for their programming support, interesting discussions and insights into other scientific fields during lunch and our $\mathrm{Rur_{tal}}$bahn rides. I would like to thank both groups for their kind and productive working environment.

I deeply thank my husband, family and friends for their listening and endless support they provided to me during my research.

Schriften des Forschungszentrums Jülich
IAS Series

Band / Volume 13
Validated force-based modeling of pedestrian dynamics
by M. Chraibi (2012), xiv, 112 pages
ISBN: 978-3-89336-799-3
URN: urn:nbn:de:0001-2012062608

Band / Volume 14
Pedestrian fundamental diagrams:
Comparative analysis of experiments in different geometries
by J. Zhang (2012), xiii, 103 pages
ISBN: 978-3-89336-825-9
URN: urn:nbn:de:0001-2012102405

Band / Volume 15
UNICORE Summit 2012
Proceedings, 30 - 31 May 2012 | Dresden, Germany
edited by V. Huber, R. Müller-Pfefferkorn, M. Romberg (2012), iv, 143 pages
ISBN: 978-3-89336-829-7
URN: urn:nbn:de:0001-2012111202

Band / Volume 16
Design and Applications of an Interoperability Reference Model
for Production e-Science Infrastructures
by M. Riedel (2013), x, 270 pages
ISBN: 978-3-89336-861-7
URN: urn:nbn:de:0001-2013031903

Band / Volume 17
Route Choice Modelling and Runtime Optimisation
for Simulation of Building Evacuation
by A. U. Kemloh Wagoum (2013), xviii, 122 pages
ISBN: 978-3-89336-865-5
URN: urn:nbn:de:0001-2013032608

Band / Volume 18
Dynamik von Personenströmen in Sportstadien
by S. Burghardt (2013), xi, 115 pages
ISBN: 978-3-89336-879-2
URN: urn:nbn:de:0001-2013060504

Band / Volume 19
Multiscale Modelling Methods for Applications in Materials Science
by I. Kondov, G. Sutmann (2013), 326 pages
ISBN: 978-3-89336-899-0
URN: urn:nbn:de:0001-2013090204

Schriften des Forschungszentrums Jülich
IAS Series

Band / Volume 20
High-resolution Simulations of Strongly Coupled Coulomb Systems with a Parallel Tree Code
by M. Winkel (2013), xvii, 196 pages
ISBN: 978-3-89336-901-0
URN: urn:nbn:de:0001-2013091802

Band / Volume 21
UNICORE Summit 2013
Proceedings, 18th June 2013 | Leipzig, Germany
edited by V. Huber, R. Müller-Pfefferkorn, M. Romberg (2013), iii, 94 pages
ISBN: 978-3-89336-910-2
URN: urn:nbn:de:0001-2013102109

Band / Volume 22
Three-dimensional Solute Transport Modeling in Coupled Soil and Plant Root Systems
by N. Schröder (2013), xii, 126 pages
ISBN: 978-3-89336-923-2
URN: urn:nbn:de:0001-2013112209

Band / Volume 23
Characterizing Load and Communication Imbalance in Parallel Applications
by D. Böhme (2014), xv, 111 pages
ISBN: 978-3-89336-940-9
URN: urn:nbn:de:0001-2014012708

Band / Volume 24
Automated Optimization Methods for Scientific Workflows in e-Science Infrastructures
by S. Holl (2014), xvi, 182 pages
ISBN: 978-3-89336-949-2
URN: urn:nbn:de:0001-2014022000

Band / Volume 25
Numerical simulation of gas-induced orbital decay of binary systems in young clusters
by C. Korntreff (2014), 98 pages
ISBN: 978-3-89336-979-9
URN: urn:nbn:de:0001-2014072202

Weitere ***Schriften des Verlags im Forschungszentrum Jülich*** unter
http://wwwzb1.fz-juelich.de/verlagextern1/index.asp

Most stars are not single but part of a binary or multiple system. These binary systems form from the gas and dust in molecular clouds usually building clusters that are initially embedded in the star-forming gas. Hence, the question arises whether the properties and frequency of binary stars change during this gas-embedded phase.

Until today, the interaction between binary systems and surrounding gas has been neglected. In this interaction, the binary system potential torques the nearby gas, producing an outgoing acoustic wave. This wave transports angular momentum from the binary system to the gas, resulting in a decay of the binary orbit.

In my thesis I investigated how a binary population in a typical young cluster is affected by this gas-induced orbital decay. When observing a forming star cluster, the developed method can be used to deduce the impact of the gas-induced orbital decay on its binary population.

This publication was written at the Jülich Supercomputing Centre (JSC) which is an integral part of the Institute for Advanced Simulation (IAS). The IAS combines the Jülich simulation sciences and the supercomputer facility in one organizational unit. It includes those parts of the scientific institutes at Forschungszentrum Jülich which use simulation on supercomputers as their main research methodology.

IAS Series
Volume 25
ISBN 978-3-89336-979-9

JÜLICH
FORSCHUNGSZENTRUM